A Ground-Based Search for Transit Timing Variations from the Apache Point Observatory

Praveen Kundurthy

A dissertation submitted in partial fulfillment
of the requirements for the degree of

Doctor of Philosophy

University of Washington

2012

Eric Agol, Chair

Andrew C. Becker

Suzanne L. Hawley

Program Authorized to Offer Degree:
Astronomy

University of Washington

Abstract

A Ground-Based Search for Transit Timing Variations from the Apache Point Observatory

Praveen Kundurthy

Chair of the Supervisory Committee:
Professor Eric Agol
Astronomy

The following dissertation presents work done as part of a ground-based transit follow-up program designed to look for transit timing variations in well-known transiting systems called, the Apache Point Survey of Transit Lightcurves of Exoplanets (APOSTLE). I outline the observing strategy, data reduction and analysis of data for the objects GJ 1214b, XO-2b and TrES-3b. The results of our analysis show general agreement with previously measured properties for these systems, and in some cases we are able to place tighter constraints on system parameters. We were able to detect a low-energy stellar flare, and three spot-crossing events with our observations of GJ 1214b. Our transit timing data do not show strong signs of timing variations and hence we are unable to claim detections of additional planets. Even though the results of this study do not present any new discoveries, the topics outlined in this dissertation are a useful synthesis of techniques used to execute a high-precision ground-based transit follow-up project.

TABLE OF CONTENTS

LIST OF FIGURES

LIST OF TABLES

ACKNOWLEDGMENTS

This dissertation would not be possible without the help of several people, on the professional and personal level.

Committee: It was great having Eric, Andy and Suzanne as advisors through graduate school. Over the course of my graduate career I have become convinced that there is no problem Eric can't solve. A large number of ideas implemented during this project were either entirely Eric's or grew from suggestions given by him. Under his guidance I was confident that I could bring the project to completion. In a similar vein, Andy helped greatly in improving my understanding of instrumentation, data reduction and observations, which make up the foundation of this dissertation. Upon his suggestion, I picked up several diverse skills which helped me streamline the project and will surely aid me greatly in the future. In a time when the academic career path is daunting, Andy's insistence that I pick up transferable skills was especially constructive. Suzanne's role as the chair of the time allocation committee for the Apache Point Observatory aided this project greatly. I have to thank her for scheduling the many transit observations presented in this dissertation, and for several efforts to ensure the successful execution of our observations. In addition to the project presented in this dissertation, Eric, Andy and Suzanne have to be thanked for helping me with other projects over my graduate career.

Funding Sources: Funding for this work came from NASA Origins grant NNX09AB32G and NSF Career grant 0645416.

APOSTLE: I owe thanks to the other members of our team, Ben Williams and Rory Barnes, who patiently listened to my weekly complaints about malfunctioning code and other trivialities. Ben played an important role in the initial instrument characterization, and Rory has helped me tie-in dynamical studies into the project. The entire APOSTLE team must be thanked for providing feedback on my work over the years.

APO: I owe thanks to Anjum Mukadam for building the *Agile* instrument without which the data presented here would not exist. Russell Owen has to be thanked for implementing science-frame guiding for *Agile*, which made my life as an observer infinitely easier. Thanks also goes to several APO staff members for ensuring my observing runs went smoothly.

Astro Front Office: Stan Vlcek, Pat Taylor and especially Sarah Garner have to be thanked for helping an organizationally and paper-work challenged student like me move things along.

Family: My parents have to be thanked for being amazingly supportive of my choice to pursue Astronomy, and it is impossible to adequately acknowledge the extent of their encouragement in the limited space. Also part of this support system have been my wonderful grand mom (*ajji*) and grand dad (*ajja*); would have been great if *ajja* had made it to see me complete the journey he saw me start, over a decade ago. Finally a very important thank you goes to my amazing partner in life, my wife Nitasha who has been beside me since my budding-astronomer days in Tucson. Couldn't have done this without you folks!

DEDICATION

This work is dedicated to my parents, Prabhakar and Vijaya, whose support and encouragement has been like a powerful rocket that propels a puny craft (*i.e.* me) on its journey to explore the stars.

Chapter 1

Introduction

"Why would they bother? Well, whenever experimentalists find a new method to measure something with vastly greater precision than was possible before, that is often sufficient motivation for them to go ahead."
– Lawrence M. Krauss

Nearly two decades after the discovery of the first planets outside our solar system, astronomers continue to comb the skies in search for more. Observational efforts on two fronts (ground-based and space-based) have revealed a great diversity in the properties of planets (and planet candidates), and posed several new questions about the planet formation process. The search for planets and the careful measurement of planetary properties are the observational foundations upon which the physics of planet formation may be understood.

There are several methods for detecting and measuring the properties of planetary systems; the two most prominent methods today are the radial velocity (RV, Mayor & Queloz, 1995) and transit techniques (Charbonneau et al., 2000). The RV technique involves measuring changes in the star's radial velocity caused by the gravitational influence of planets (using the Doppler shifts of stellar spectral lines). RV observers can place lower limits on the planetary mass ($M_p \sin i_{\rm orb}$), where M_p is the planetary mass and $i_{\rm orb}$ is the unknown inclination of the planet's orbit with respect to the sky-plane. Other planetary properties such as the orbital period, semi-major axis (a) and eccentricity (e) can also be measured (given that the properties of the host star are

known). The transit method applies to those systems where the orbital inclination of a planet is close to 90° (*i.e.* edge-on) with respect to the observer's sky-plane. In this case, when a planet and star cross each other in the line of sight of an observer, changes in the total flux can be detected due to eclipse events. For the case when the planet obscures the star, the eclipse event is called a transit (and is sometimes referred to in the literature as the 'primary eclipse'). During a transit, observers can detect dips in starlight caused by the obscuration of a portion of the stellar disk by the passing planet. When the star conceals the planet as the planet moves behind the star in its orbit, the eclipse event is called an occultation (or 'secondary eclipse'). These events are harder to detect due to the forbiddingly small planet-to-star flux ratio at wavelengths accessible to ground-based telescopes, since planets tend to emit most of their energy in the infrared (or longer wavelengths).

Several system properties can be measured from observing a transit, including the ratio of the sizes of the planet and star ($R_p/R_\star$, where R_p and $R_\star$ are the radii of the planet and star respectively). Systems where a planet can be detected using both RV and transit methods are ideal laboratories to test theories of planet formation, since we can determine the planet's mass and radius, and hence understand its internal composition by computing the average planetary density (ρ_p).

The exoplanet community has co-opted the term 'architecture' to embody several properties of planetary systems such as multiplicity and orbital parameters like eccentricities (e), inclinations ($i_{\rm orb}$), semi-major axes (a) and orbital periods. Planetary properties (like M_p and R_p distributions) may also be included. Studying the architecture of planetary systems is the key toward developing theories of planet formation that can adequately explain the origin and evolution of all planetary systems (including our own). The architecture of a given planetary system holds clues to its forgotten origin. For example, the earliest discoveries of planets were almost exclusively of gas giants close to their parent stars (*i.e.* Hot-Jupiters). It is useful to note that these early discoveries were of planets which have no analog in the solar system.

Hot-Jupiters are believed not to have formed in-situ, since their gaseous components could only have accreted in the volatile-rich outer regions of the protoplanetary disk (Pollack et al., 1996). To explain their final orbital configurations, inward migration mechanisms were invoked (Lin et al., 1996; Rasio & Ford, 1996; Masset & Papaloizou , 2003). Migration was given little importance during the time when the only known planetary system was our own solar system. Most models of in-situ planet formation easily explain the solar system's architecture. Today however, most planet formation models (even those of the solar system) include some form of planet migration (Gomes et al., 2005; Tsiganis et al., 2005; Walsh et al., 2011). Observations of Hot-Jupiter systems show (a) stellar spin and planetary orbit misalignment is prevalent (Albrecht et al., 2012) and (b) several Hot-Jupiter circular orbits. These observations have bolstered the theory that Hot-Jupiters form via a process of dynamical excitation of their orbits and circularization via tidal dissipation (Fabrycky & Tremaine, 2007). In exoplanet science, there is no question that the ability of observers to make new findings propels the development of theory.

The search for new exoplanetary systems has advanced to space-based observations with the launch of the European Space Agency's (ESA) *CoRoT* satellite (Fridlund et al., 2006) and its larger and more successful NASA cousin *Kepler* (Borucki et al., 2010). Both missions are designed to look for new transiting planets by continuously monitoring certain regions of the sky. At the time of writing this dissertation, *Kepler* has revealed the smallest planets outside our solar system (Kepler 20e & 20f, $R_p = 0.87R_\oplus$ & $1.0R_\oplus$ respectively Fressin et al., 2011). Observations from *Kepler* (and *CoRoT*) have led to the discoveries of several types of planets and planetary systems which share little resemblance with our own solar system. However, *Kepler*'s discovery of a terrestrial-sized planet (2.4 $R_\oplus$) in the habitable zone of a main-sequence star (Borucki et al., 2011c) is a clear sign that we are inching towards the long sought-after discovery of a habitable Earth-twin. The vast majority of *Kepler* discoveries however, are classified as planet candidates rather than planets since

their masses have not been constrained (and are not likely to be soon) with either RV or other follow-up methods. Some *Kepler* planet discoveries, only have upper mass limits placed from measurements of radial velocity and careful ruling out of false-positive scenarios. These upper limits only confirm their planetary nature, and do not characterize the system. The greatest impediment to complete characterization of planetary mass is the faintness of the stars in the *Kepler* field (most *Kepler* targets are between 200–900 pc away). However, for the unique scenario where planets in a multi-planet system have commensurate orbital periods, *i.e.* they are close-to or in mutual mean motion resonance (MMR), their masses can be determined. Planets in such systems have times of mid-transit which fluctuate around the times expected from the Keplerian period. These variations arise due to the fact that the mutual gravitational influences of these planets are maximized at predictable points in their orbital phases. These coherent perturbations to their orbits cause the period of the planet to oscillate around the purely Keplerian case. Lissauer et al. (2011a) showed that the amplitude of these oscillations can be used to constrain planetary mass ratios and hence to characterize the given system. The difference in mid-transit times from the transit times predicted from assuming a strictly Keplerian orbit are called transit timing variations (TTVs).

The *Kepler* mission has tallied several *candidate* multi-planet systems (Lissauer et al., 2011b), and has made the first discoveries of multi-planet systems showing transit timing variations (Holman et al., 2010; Lissauer et al., 2011a; Ballard et al., 2011; Nesvorný et al., 2012). All the *Kepler* TTV systems satisfy the condition of being close to MMR. Of *Kepler*'s TTV systems, the planets of Kepler-9 (Holman et al., 2010) and Kepler-11 (Lissauer et al., 2011a) were first detected in transit and the TTVs were confirmed only after fitting ephemerides to all eclipse times. Using the TTV technique to look for additional planets was first proposed by Agol et al. (2005) and Holman & Murray (2005). So even for a system where only one planet is seen in transit, a deviation from the Keplerian period could indicate the presence of

additional undetected planets. Ballard et al. (2011)'s discovery (of Kepler 19) was the first case where the perturber (Kepler 19-c) was detected by TTV and is not seen in transit, thereby fullfilling the predictions of Agol et al. (2005) and Holman & Murray (2005) that the TTV technique can be used to establish multiplicity.

Apart from the *Kepler* systems, TrES-1 (Steffen & Agol, 2005, *HST*), HD 189733 (Miller-Ricci et al., 2008a, *MOST*), CoRoT-1 (Bean, 2009, *CoRoT*) and GJ 436 (Ballard et al., 2010, *Spitzer*) have been monitored with various space-based telescopes but no TTVs have been reported. There have also been ground-based attempts to look for TTVs for the systems OGLE-111 (Díaz et al., 2008; Adams et al., 2010), TrES-3 (Gibson et al., 2009) and HAT-P-13 (Pál et al., 2011; Nascimbeni et al., 2011b; Fulton et al., 2011). For most of these systems TTVs have either not been detected or interesting deviations have been ruled out by follow-up work. The studies on WASP-3 (Maciejewski et al., 2010), WASP-5 (Fukui et al., 2011) and WASP-10 (Maciejewski et al., 2011) have shown that ephemeris fits that include additional planets match the observed TTV data better than a linear ephemeris for a single planet. However these claims are tentative because (1) as with most ground-based data to date, these data do not have continuous coverage of transits and hence no trends (such as periodically varying TTVs) have been reported; and (2) tracking sources of systematic uncertainties is challenging and several of the larger transit timing deviations could be due to unknown systematics or underestimated timing errors (Fukui et al., 2011).

1.1 Thesis Outline

This dissertation describes work done as part of the Apache Point Observatory Survey of Transit Lightcurves of Exoplanets (APOSTLE). APOSTLE is one of several ground-based projects looking for signs of transit timing variations in previously known systems around nearby stars. The targets observed so far by APOSTLE are WASP-2b (Collier Cameron et al., 2007a), XO-2b (Burke et al., 2007), TrES-

3b (O'Donovan et al., 2007) and GJ 1214b (Charbonneau et al., 2009). APOSTLE observations have yielded transit lightcurves with photometric precision on the order of a few hundred ppm (parts per million). High photometric precision translates directly to more accurate and precise measurements of transit times. Transit times measured to better than $\sim$ 1 minute precision should be sufficient to detect TTVs produced by the gravitational influence of other planets in a given system.

In Chapter 2, I first discuss the APOSTLE project by outlining the observing strategy and the observing history of the objects discussed in this dissertation. Secondly, I cover the details of instrument characterization, and the development of a customized reduction pipeline for APOSTLE data. Chapter 3 discusses the models used to characterize transit lightcurves and Chapter 4 describes the use of a Markov Chain Monte Carlo routine developed to fit transit lightcurves. The three chapters that follow Chapter 4 describe how this analysis was used on all APOSTLE data, where Ch. 5, Ch. 6 and Ch. 7 describe the results for GJ 1214, XO-2 and TrES-3 respectively. The final chapter (Ch. 8) summarizes the results and discusses the future of ground-based observations and follow-up of transiting planets.

Chapter 2

APOSTLE

The Apache Point Observatory Survey of Transit Lightcurves of Exoplanets (APOSTLE) is a high-precision ground-based photometric follow-up program designed to look for transit timing variations (TTVs). The project was conceived by Andrew C. Becker and Eric Agol of the University of Washington to take advantage of the combination of the 3.5m aperture of the ARC[1] telescope and the high-speed frame-transfer photometer, *Agile* (Mukadam et al., 2011). Most wide-angle surveys that search for transiting planets have small apertures, which result in lightcurves with low photometric precision that are often only good enough to make detections of the transit event, and are not suited for characterization. Transit discoveries are almost always followed up with observations using a larger aperture telescope in order to constrain system parameters (e.g. recent SuperWASP and HATNet discoveries, Faedi et al., 2011; Howard et al., 2012). The greater collecting power of a larger telescope results in improved photometric precision and hence better constraints on transit parameters. The *Agile* CCD has virtually no dead-time during read out (100% duty cycle), which further enhances the precision with which the time of mid-transit can be measured. Given a set of time series data observed at a cadence of Γ (measurements per second), with the ideal characteristic of displaying only uncorrelated Gaussian noise at a level of σ_{ph}, the precision on the transit time scales as $\sigma_{TT} \approx (t_G/2\Gamma)^{1/2}\sigma_{ph}(R_p/R_\star)^{-2}$, where t_G is the ingress/egress duration (Ford & Gaudi, 2006). The parameters, R_p and $R_\star$ are the planetary and stellar radius respec-

[1]Astrophysical Research Consortium

tively. For typical transiting systems, if one can achieve a photometric precision $\sim 10^{-3}$ (without correlated noise) the transit times can be constrained to within 10 seconds. This level of timing precision is more than sufficient to detect timing variations > 1 min. Transit surveys from the ground typically achieve photometric precisions that are an order of magnitude worse (e.g. $\sim 10^{-2}$, Pollacco et al., 2006).

For the case when planets are in MMR, Agol et al. (2005) describe roughly how the maximum timing deviation ($\delta t_{\rm max}$) scales with properties of the system,

$$\delta t_{\rm max} \sim \frac{P}{4.5j} \frac{m_{\rm pert}}{(m_{\rm pert} + m_{\rm trans})} \tag{2.1}$$

where $m_{\rm pert}$ and $m_{\rm trans}$ are the masses of the perturbing planet and the transiting planet respectively. The period of the transiting planet is P and the order of the resonance is j (where $j = 1$ in the case where inner-to-outer period ratio is 2:1). For a Jupiter-mass transiting planet on a 2 day orbit in a 2:1 MMR with an outer Earth-mass perturber, the maximum amplitude of the timing variation is ~ 2 min. More massive perturbers and/or lower mass transiting planets will result in larger timing variations. The period of libration of these variations scales roughly as $P_{\rm lib} \sim 0.5 j^{-4/3} \mu^{-2/3} P$ (Agol et al., 2005), where μ is the mass ratio of the massive planet to the host star. For the example provided above, given the transiting planet orbits around a solar twin, the timing variations would oscillate over a period of ~ 100 days. Prior to 2010, most known transiting planets had periods < 10 days and typical masses < 5 Jupiter-masses ($M_{\rm J}$). A significant portion of parameter space for hypothetical systems in MMRs are well within the range of any survey which can achieve photometric precision of 1000 ppm (parts per million) or better. The APOSTLE project began on this premise in late 2007 and has since monitored a small sample of known transiting systems, achieving its set photometric and timing precision goals.

2.1 Observing Strategy

Target selection was the first step in the execution of the survey. From the catalog of known transiting planets, systems that had published periods, transit times and host star coordinates were shortlisted. Planets in crowded fields like those discovered by the SWEEPS (Sahu et al., 2006) and OGLE (Szymański et al., 2001) surveys were excluded, since these targets were generally faint and photometry on these fields would have resulted in limited photometric precision. Targets from space-based telescopes like *CoRoT* and *Kepler*, which already deliver excellent photometry, were also excluded.

The next stage of vetting targets was focused on excluding systems where APOSTLE's proposed photometric precision could not be achieved. Rather than use flux calibrated (absolute) photometry, APOSTLE (like most other transit observations) utilizes high signal-to-noise differential (relative) photometry. In this method, the instrumental brightnesses of the target and an adjacent comparison star are used to compute the lightcurve. It is obviously easier to achieve high signal-to-noise when a target is bright, hence, for high precision differential photometry the comparison star (or stars) must also be of similar brightness (and ideally of similar color). The precision on differential aperture photometry is limited by the precision achieved on the faintest star in the field. Also, over the course of an observing night, extinction due to observing through varying atmospheric columns (airmass) can cause slight deviations in the relative count rate for objects of different color, a phenomenon known as differential extinction. To minimize this effect the target and comparison star should ideally be of similar color. An instrumental constraint also exists as a result of *Agile*'s somewhat limited field of view (FOV), of 2.5' × 2.5'. The comparison star thus needs to be sufficiently close to (but not blended with) the target star. Given these conditions, the target list was shortened further by querying the USNO-B1.0 catalog (Monet et al., 2003) for comparison stars within 3.2' (diagonal extent of FOV) and a

target-to-comparison ΔMag ≤ 1.0 in USNO-B1.0 R magnitudes. The requirement for color similarity was relaxed, since it considerably shortened the list of observable candidates. The APOSTLE team decided to address the effects of differential extinction on the data during the detrending process (see § 2.2).

The final step in target selection simply involved checking observability from APO. Given the known ephemerides of the shortlisted systems, a search was done for when the expected transit (including pre-ingress and post-egress portions) fell within a given observing window. Over the course of the project, four candidates (WASP-2, GJ 1214, XO-2 and TrES-3) were consistently observable and became the primary set of APOSTLE targets. The results for GJ 1214, XO-2 and TrES-3 are covered in this dissertation and WASP-2 will be discussed in an upcoming article by Becker et al. (in prep).

Starting in late 2007, APOSTLE was granted 66 half-nights by the APO time allocation committee through a competitive selection process. Owing to weather and other technical difficulties APOSTLE so far has gathered 36 usable lightcurves; giving a rate of observing success $> 50\%$. A summary of the observing history is presented in Table 2.1, with a more detailed outline given in the appropriate chapters that follow (Ch. 5, 6 and 7).

During the early stages of the project an optimal observing strategy had not been decided. Several of the initial lightcurves were gathered at short cadences (0.5 and 1.0 second readouts). In addition several of the early APOSTLE observations were in the I–band (with filter centered at $\lambda_0 = 805$nm, Cousins, 1976; Bessell, 1990). The short readout mode allowed for fine sampling of the lightcurve, but due to the lower signal-to-noise and the unsuitability for characterizing systematics, this observing mode was abandoned. In addition, the I–band images also contained a strong contribution from a fringe pattern (caused by interference from the backscattering of atmospheric lines within the CCD's pixels). Early in 2010, the observing strategy was switched to longer readouts (typically 45–75 seconds) to reduce the level of correlated

Table 2.1: APOSTLE Observations

Object	I–band(S)	I–band(L)	r'–band(L)	Total
Presented in This Dissertation				
GJ 1214	0	0	6	6
XO-2	4	2	4	10
TrES-3	0	0	11	11
Presented in Becker et al. (in prep)				
WASP-2	3	4	3	10

S = Short exposures (0.5-10 sec)

L = Long exposures (45-75 sec)

noise (red-noise), and were made using the r'–band, which is similar to the SDSS[2] r filter (λ_0 = 626nm, Fukugita et al., 1996), to reduce the influence of fringes. In this observing mode, the telescope was defocused to spread the stellar point-spread function (PSF) across multiple pixels, which minimized the systematics caused by pixel-to-pixel wandering of the PSF. The longer exposures also allowed for a greater count rate which maximized the signal-to-noise per image. The count rate was kept below *Agile*'s non-linearity limit of ∼52k ADU and well below its saturation level of 61k ADU by small adjustments to the telescope's secondary focus.

A variety of image processing steps from correction of counts in the non-linear regime to the removal of the fringe pattern are discussed in the section on the data reduction (§ 2.2) that follows. The APOSTLE catalog contains data gathered using the I–band and r'–band, using both short and long exposures. The short exposure data are binned before analysis. In addition to target frames, sky-flats and dark frames were also collected each night. Dark frames are simply closed filter exposures

[2]Sloan Digital Sky-Survey

on the CCD which help characterize the intrinsic thermal noise on the CCD. The sky-flats are exposures of the twilight sky (or the night sky without tracking), which ideally serves as a uniform illumination source. The sky-flats are used to characterize the flat-field (or illumination pattern), which describes the pixel-to-pixel variations in sensitivity on the CCD.

2.2 Data Reduction: Tracking Down Sources of Error

A common reason for the premature declaration of an interesting trend or anomalous measurement where there is none, is because the error analysis was incomplete. When an observational or experimental setup pushes into new areas of precision, it often becomes sensitive to sources of error previously considered insignificant. Established methods of data reduction often exclude several such sources of error, which must be reintroduced into the analysis for higher precision measurements. In order to best understand the sources of uncertainty we developed a customized image reduction pipeline using the Interactive Data Language (IDL). The pipeline carries out all the standard steps of astronomical image reduction and propagates the errors accumulated in each step to create an error image with a map of pixel-to-pixel uncertainties.

The following subsections detail image processing step-by-step, including dark current subtraction, correcting counts in the non-linear regime, removal of the illumination (flatfield) and fringe patterns, and finally the photometry. All expressions for errors stem from the standard error propagation equation for uncorrelated quantities:

$$\begin{aligned} F(x_i) \quad &, \quad i = 1, ...N \\ \sigma_F^2 \quad &= \quad \sum_i^N \sigma_i^2 \left(\frac{\partial F}{\partial x_i} \right)^2 \end{aligned} \tag{2.2}$$

where F is the quantity for which one needs to determine uncertainties, and is dependent on N uncorrelated quantities x_i.

2.2.1 Readout Noise, Dark Current & Non-Linearity

The raw counts within a given pixel in the unprocessed image have an uncertainty which is simply the sum of the Poisson noise (due to photon counting) and noise incurred from reading out the charge (read noise) and converting to digital units called ADU[3] (counts). The Poisson noise for the raw counts ($C_{\rm raw}$) is simply $\sqrt{C_{\rm raw}}$, and the read noise R_D. Typically the read noise must be divided by the instrument Gain to convert from electron counts (e^-) to ADU units. Hence the square of the intrinsic error on each pixel is given by the following equation, which applies to all unprocessed frames including darks and sky-flats.

$$\sigma^2_{C_{\rm raw}} = \frac{C_{\rm raw}}{\rm Gain} + \left(\frac{R_D}{\rm Gain}\right)^2 \tag{2.3}$$

Long exposure observations were made using *Agile*'s medium gain, slow readout (100kHZ) mode with frames binned by a factor of 2, yielding a plate-scale of $0\farcs258$/pixel. The same binning applied to the short exposure modes, however for short exposures *Agile* was set to medium gain, fast readout (1MHz) mode. The read noise and gain values applied during reduction were different for the two readout modes. The read noise and gain were 3.66 e^- and 1.96 e^-/ADU respectively, for the long exposure, and 6.62 e^- and 1.93 e^-/ADU respectively, for the short exposure observations [4].

The first step in reduction is the creation of a Masterdark frame which represents an estimate of the thermal noise for a given exposure. During a typical APOSTLE observing night, we collected 25 dark frames for every exposure time used (sky-flats and target frames). Each set of darks were stacked and co-added after outlier rejection to create a Masterdark frame. The uncertainty in a given pixel of the Masterdark ($\sigma_{\rm MD}$) is simply the standard deviation of the stacked points used to compute the median. Target frames and sky-flats are dark-corrected by simply subtracting the Masterdark

[3] Analog to Digital Units

[4] *Agile* instrument manual, 2012: http://www.apo.nmsu.edu/arc35m/Instruments/AGILE/

(MD) and the errors in the resulting frame are the sum in quadrature of $\sigma_{\rm raw}$ and $\sigma_{\rm MD}$.

The count level in a CCD's pixel-well increases linearly with the number of detected photons (which are converted to electrons by the photoelectric effect). However, as the count levels approach the saturation limit (*i.e.* the maximum well capacity) the count rate slows and rises in a non-linear manner until the pixel saturates. Pixels that have entered this regime can be salvaged and corrected to their expected values given a linear count rate, unlike pixels which have saturated.

During the characterization of *Agile*, Andrew C. Becker empirically fit for the non-linear accumulation rate using a sequence of exposures, starting with 2 seconds and doubling it till saturation was reached. The non-linear portion of the accumulation is roughly described by,

$$\begin{aligned} C^{'} &= C \times (1 + s_1(\log_{10} C - \log_{10} s_0)) && \text{(2.4a)} \\ &= C \times K && \text{(2.4b)} \\ K &= 1 + \frac{s_1 \ln (C/s_0)}{\ln 10} && \text{(2.4c)} \end{aligned}$$

where C and $C^{'}$ are the pixel counts pre and post correction respectively. The quantity K, is the correction factor for pixels above s_0 (the cutoff where the pixels are non-linear), and s_1 is a scaling factor for the logarithmic fitting function (Eq. 2.4c). The uncertainty incurred from this correction can be computed from the error propagation equation (Eq. 2.2). The frame to be corrected for non-linear pixels C is assumed to be dark-subtracted, and hence σ_C will contain the errors propagated from this transformation.

$$\sigma^2_{C'} = \sigma^2_C K^2 + \sigma^2_K C^2 \qquad \text{(2.4d)}$$

where σ^2_K in greater detail (using 2.4c) is:

$$\sigma^2_K = \frac{1}{(\ln(10))^2} \left[\sigma^2_{s_1} (\ln(C/s_0))^2 + \sigma^2_C (s_1/C)^2 + \sigma^2_{s_0} (s_0/s_1)^2\right] \qquad \text{(2.5)}$$

If $C < s_0$ then the correction factor K equals 1 and $\sigma_K = 0$, and the error equation reduces to the error in ADUs for each pixel. The empirically derived values for s_0 and s_1 and their uncertainties are shown in Table 2.2 (private comm. Andrew C. Becker).

Table 2.2: Coefficients for Non-linearity Correction

Quantity	Value (ADU)	Error^2	Value
s_0	52304.877	$\sigma^2_{s_0}$	3.996001
s_1	0.21759	$\sigma^2_{s_1}$	0.056734

2.2.2 The Flatfield, Fringe Pattern & Science Ready Frames

APOSTLE exclusively uses twilight or drift flats during its observations. Since the overall count level of a given set of sky-flats will vary, these frames are (1) normalized by the global image median, (2) stacked and median combined after outlier rejection to create the Masterflat (MF). The resulting illumination pattern is then divided from every dark-subtracted target frame to create science ready images. The uncertainty in the Masterflat ($\sigma_{\rm MF}$) is simply the standard deviation of the stacked normalized pixels.

For *Agile* I–band images however, there is an additional step after flat-fielding due to the fact images taken in this filter contain a fringe pattern. Photons from strong atmospheric lines (in the I-filter bandpass) backscatter within the CCD pixels, and owing to the variable thickness of the pixel array, interfence between photons from these lines cause the fringe pattern. Since the fringe pattern is convolved with the illumination pattern of the CCD, it is challenging to completely remove it. Images taken in filters in the r'–band and bluer are known not to show significant fringing (Mukadam et al., 2011). Benjamin C. Williams and Andrew C. Becker created an

I–band Fringe-frame for *Agile* which was utilized in the APOSTLE reduction pipeline. This frame was produced by median combining dithered frames on the dark sky, where flux contributions from stars were removed by outlier rejection. The final Fringe-frame is normalized such that it has a median of zero, and an amplitude of one.

The fringe correction process assumes that a target frame affected by fringing ($T^{'}$) is simply a linear combination of the science frame (T) and the fringe pattern:

$$T^{'} = T + a_0 F \tag{2.6}$$

where F is the Fringe-frame and a_0 is a scaling factor describing the amplitude of the fringing on a given frame. The frame $T^{'}$ has been corrected for the dark current, non-linearity and the flatfield. During reduction of I–bandframes, the fringe amplitude is estimated by minimizing χ^2 between the input data and the above linear model. We typically found the resulting frame ($T = T^{'} - a_0 F$) to be sufficiently corrected of fringes after visual examination. The fringe amplitudes (a_0) were always smaller than the RMS of the global sky background on each frame, with a_0 ranging between 6–13% of the sky RMS for XO-2 and between 12-16% of the sky RMS for WASP-2 I–band data. The errors from the fringe frame (σ_F) are also propagated to the final science image. Figure 2.1 shows an example of results from the application of the APOSTLE reduction pipeline on an I–band image of XO-2.

In summary, the APOSTLE reduction pipeline for *Agile* target frames can be summarized by the following equation; in terms of the data products of the reduction pipeline, the equations represent the science frame (T) and its corresponding error frame (σ_T^2).

$$T = \frac{(C_{\rm raw} - {\rm MD})K}{\rm MF} - a_0 F \tag{2.7a}$$

with the complete error term written as,

$$\sigma_T^2 = \frac{K^2}{\rm MF^2}\left[\sigma_{C_{\rm raw}}^2 + \sigma_{\rm MD}^2 + \left(\frac{C_{\rm raw} - {\rm MD}}{\rm MF}\right)^2 \sigma_{\rm MF}^2\right] + \left(\frac{C_{\rm raw} - {\rm MD}}{\rm MF}\right)^2 \sigma_K^2 + a_0^2 \sigma_F^2 \tag{2.7b}$$

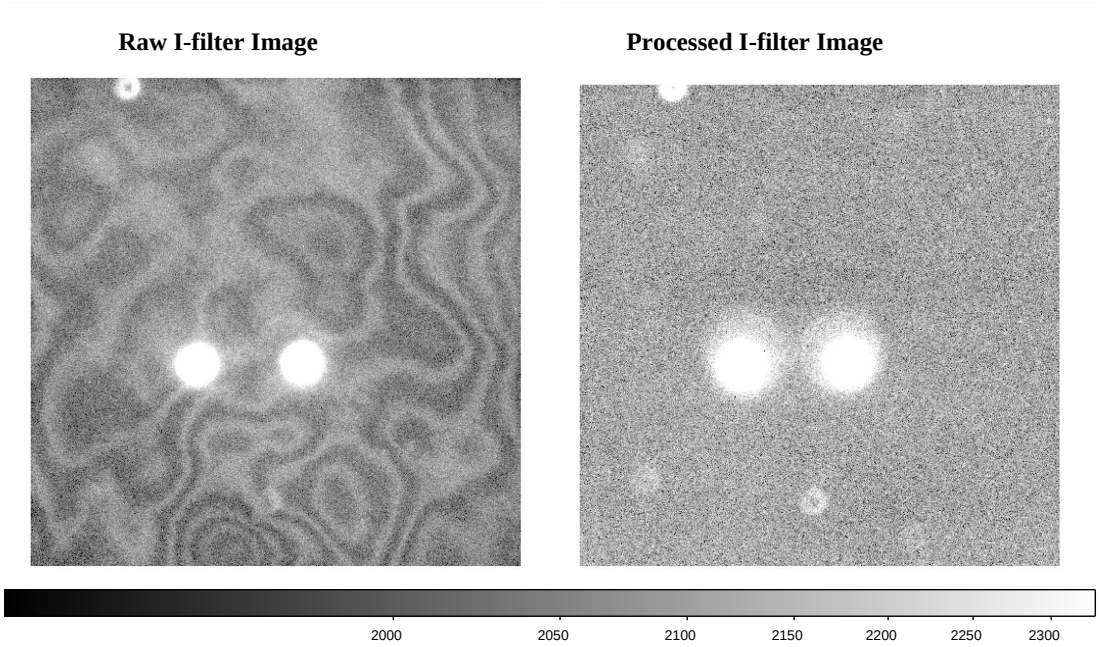

Figure 2.1: Raw (left pane) and processed (right pane) images of XO-2 taken with *Agile* on Nov 22, 2008. The fringe pattern is clearly visible in the raw frame, and has mostly been removed in the processed frame. The gray scale color bar shows the count levels in ADUs in the square-root scaling.

2.2.3 Optimal Aperture Photometry

We used SExtractor (Bertin & Arnouts, 1996) to derive initial centroids of our defocused stars. This software allows the use of a customized PSF kernel, and we ended up using a 'donut'-shaped detection kernel for data gathered when the telescope was strongly defocused. We used the default Gaussian PSF kernel for instances where the telescope was not defocused, which was true for short exposure data (exposures $<$ 45 sec). Coordinates obtained from SExtractor were then used for circular aperture photometry with the PHOT task in IRAF's NOAO.DIGIPHOT.APPHOT package. We derived flux estimates from a range of circular apertures with radii between 5–50 pixels, at intervals of 1 pixel, by simply summing the counts in these apertures. An outlier–rejected global median on the frame was used as the sky estimate, which is

removed to derive the instrumental flux of the stars. To derive photometric errors, we extracted counts from the error frames using the same centroids and apertures used for photometry on the target frames. Estimating photometric errors in this manner yielded uncertainties that were greater (by 50%) when compared to the default errors reported by PHOT. As established in the previous sections (§ 2.2.1 and § 2.2.2), this method takes into account sources of error which are otherwise ignored by standard photometric techniques, and hence gives more conservative estimates of the photometric uncertainty.

To decide on the optimal aperture, we investigated the transit lightcurve on a given night using a range of photometric apertures (with radii between 5 - 50 pixels). The fluxes derived from photometry were used to create transit lightcurves by dividing the flux of the target star by the comparison star and then dividing the entire lightcurve by the median out-of-eclipse flux level. This transformation returns the lightcurve in units of normalized flux-ratio. Next, each transit lightcurve was detrended (using the technique to be described in the upcoming § 2.2.4) and normalized by a trial model lightcurve (with the transit parameters chosen to be close to previously known values). The aperture where the scatter in the normalized residuals around this model is minimized was chosen as the optimal aperture. Smaller apertures do not completely sample the flux from the stars, and at larger apertures one loses signal-to-noise due to the fact that one accumulates fewer counts from the star when compared to sky counts. The optimal aperture typically fell between 5–50 pixel radii. We present the complete list of optimal apertures in the appropriate observation sections for each system. The sizes of the typical apertures were always a few times larger than the typical half-width at half maximum of the stellar PSFs. The photometric precisions are also listed in the observing summary tables in Chapters 5, 6 and 7.

2.2.4 Nuisance Parameters & Detrending

There are many systematic trends that may be introduced over the course of observing which may not be accounted for by the reduction protocols described in § 2.2.1 and § 2.2.2; for example, differential extinction due to airmass variation or photometric variation due to centroids wandering over pixels of varying sensitivities (e.g. due to small imperfections in the flat-fielding). Thus, for each image we extracted a set of nuisance parameters which were then used to compute a correction function (*i.e.* detrending function) to remove these trends (which are listed in Table 2.3). To avoid affecting the transit signal the detrending correction is applied to the data after the transit signal is removed. So for data from a given night, the goodness of fit (χ^2) is given by:

$$\chi^2 = \sum_{i}^{N_{\rm Data}} \frac{(O_i - M_i - F_{cor,i})^2}{\sigma_i^2} \tag{2.8a}$$

where $N_{\rm Data}$ represent the number of time series points (noted by the index i), O_i are the observed lightcurve data, M_i is the transit model, $F_{cor,i}$ is the correction function and σ_i are the observational errors on the lightcurve. The correction function (F_{cor}) is modeled as a linear sum of nuisance parameters as described by the following equation:

$$F_{cor,i} = \sum_{k=1}^{N_{\rm nus}} c_k X_{k,i}, \tag{2.8b}$$

where $X_{k,i}$ are the nuisance parameters, c_k are the corresponding coefficients. The index k counts over the number of nuisance parameters $N_{\rm nus}$. The list of nuisance parameters are listed in Table 2.3.

The airmass, Telrot, and Telfocus parameters were extracted from image headers when available. When airmass was unavailable, we recomputed values, using *pyephem* (Rhodes, 2008, rhodesmill.org/pyephem/index.html), given the time stamps, observation date, the telescope's global coordinates, and the object's sky coordinates. The centroid positions (x1, y1) and (x2, y2), were taken from the SExtractor output during the photometric processing. We also extracted the aperture counts on the Masterdark

Table 2.3: List of Nuisance Parameters

#	Nuisance Pars.	Description
1	airmass	Atmospheric column Density
2	msky1	Local sky brightness around Target Star
3	msky2	Local sky brightness around Comparison Star
4	gsky	Global sky brightness
5	x1	SExtractor x position of the Target Star
6	y1	SExtractor y position of the Target Star
7	x2	SExtractor x position of the Comparison Star
8	y2	SExtractor y position of the Comparison Star
9	sD1	Counts in Target star aperture on the Masterdark
10	sD2	Counts in Comparison star aperture on the Masterdark
11	sF1	Counts in Target star aperture on the Masterflat
12	sF2	Counts in Comparison star aperture on the Masterflat
13	a_0	Fringe amplitude for I-band Images
14	Telrot	Rotation of Telescope
15	Telfocus	Focus on secondary mirror

and Masterflat frames (rows 9-12 in Table 2.3) using the centroids and apertures from the photometric processing. These sums may trace subtle pixel-to-pixel sensitivity variations. The sky values, msky1 and msky2, are median estimates of the background flux level around the target and comparison stars respectively. These values were computed between circular annuli at 50 and 60 pixels. The global sky (gsky) is simply the median background level on the entire image. For I–band images we also stored the values of the best-fit fringe amplitude a_0 (from Eq. 2.6).

Not all the parameters listed in Table 2.3 are used while detrending the lightcurves.

A suitable set of detrending parameters were selected for a given night by running several manual trials of linear least squares minimization on Eq. 2.8a. The model parameters were fixed at reasonable values and only the coefficients (c_k) were fit. Those nuisance parameters which returned large uncertainties on the coefficients were excluded since this indicated a poor match to the noise trend in a lightcurve. This method of selecting nuisance parameters is admittedly ad-hoc. However, given the diversity of observing conditions and data quality, there was no way to automate the optimal selection of nuisance parameters. The detrending is performed using the final set of nuisance parameters in conjunction with fitting the transit parameters in order to ensure that the correction process is not biased by the trial model used in the selection of nuisance parameters.

2.2.5 Barycentric Time Correction

During observations, the charge on *Agile* is read out using GPS-synchronized pulses with an absolute timing accuracy better than a millisecond (Mukadam et al., 2011). The UTC (Coordinated Universal Time) stamps in *Agile*'s image headers are accurate at this level, and hence suitable for use by APOSTLE to look for TTVs on the order of minutes. However there are several corrections that need to be made before any TTV analysis. The IAU[5] recommends the use of TCB (Barycentric Coordinate Time[6]) for any work involving timing analysis (Kaplan, 2005). TCB is considered to be the best approximation to making timing measurements from an inertial reference frame. Conversion to this system accounts for time delays caused by the orbital motion of the Earth, and the gravitational effects of the Sun and planets, are corrected and relativistic effects are also taken into account. In effect, events reported using TCB are equivalent to making measurements from the solar system barycenter (SSB). The

[5]IAU – International Astronomical Union

[6]TCB – Temps-Coordonneé Barycentrique

transit community has recently adopted TDB (Barycentric Dynamical Time[7]). This time coordinate is related to TCB by an offset and a linear scaling factor (Standish, 1998; Eastman et al., 2010). Even though the TDB system is not quite in the physical S.I. units of 'second', it is closer to a time system used by widely accepted calculations of solar system ephemerides. To avoid general confusion, *all timing measurements are reported in TDB*, in conformance with the rest of the exoplanet transit community.

Eastman et al. (2010) have presented IDL routines which do the required conversion from UTC to TDB. The APOSTLE team had independently developed a set of routines to make the required conversion, and incorporated them in the reduction pipeline. UTC time stamps were converted to TDB using prescriptions described in Seidelmann & Fukushima (1992), Standish (1998), Hobbs et al (2006), and Edwards et al. (2006). The general time coordinate transformation follows,

$$TDB(\mathrm{JD}) = UTC(\mathrm{JD}) + C_{\mathrm{cor}} + G_{\mathrm{cor}} + E_{\mathrm{cor}} \tag{2.9}$$

where $TDB(\mathrm{JD})$ and $UTC(\mathrm{JD})$ are the Julian day representation of these times. The terms C_{cor}, G_{cor} and E_{cor} are the clock correction term, the geometric correction (or the Roemer delay) and the relativistic correction (or the Einstein delay) term respectively.

The clock correction term (C_{cor}) simply converts UTC time, which is based on the rotation of the Earth, to the atomic clock based Terrestrial Time (TT) coordinate. The next step in the correction accounts for the fact that observers on the Earth are not in a stationary reference frame. Due to the Earth's annual motion around the Sun, the light travel time from a given target star to an observer on the Earth will vary depending on the time of the year. The geometric correction (G_{cor}) simply accounts for this shift in time by reconciling all readings to the solar system barycenter (SSB). We used the publicly available JPL ephemerides (JPLEH.405) of solar system objects to estimate the Earth's position in a SSB centered reference frame. The light travel

[7]TDB – Temps Dynamique Barycentrique

time correction is then computed from this information. The IDL library `cmephem` contains useful routines that can read JPL ephemerides and perform appropriate interpolations at high precision (Markwardt, 1997). However, one must note that the time coordinates used in JPLEPH.405 though similar to TT, are not in the same physical units. The time coordinate TT is in units of the S.I. second, whereas the time coordinates in JPLEPH.405 are in simulation time units, which differ from the S.I. second very slightly. Kaplan (2005) state that querying the ephemeris files using TT can incur timing inaccuracies on the order <2 milliseconds. This level of error is well below APOSTLE's timing precision requirements and hence can be ignored. The next important correction is the relativistic correction ($E_{\rm cor}$) that corrects for the time-keeping rate of clocks under the influence of the Earth's gravitational field and orbital motion. The TT coordinate (after geometric correction) is converted to TDB based on an analytic approximation to the relativistic correction (Fairhead et al, 1988; Fairhead & Bertangnon, 1990), as implemented in the Markwardt library's `TDB2TDT.pro` routine (Markwardt, 1997).

Time corrections are still not complete with the steps described above. Pulsar astronomers who need to be exceedingly careful of time-keeping errors include additional terms like the Shapiro delay, or Interstellar refraction (Hobbs et al, 2006). The Shapiro delay, which is due to the bending of light in the solar system's potential well (even accounting for the positions of the planets) is the next most significant contributor of the correction terms (Hobbs et al, 2006; Edwards et al., 2006). However we can confidently ignore this term since its contribution to timing delays is on the order of microseconds. We also confirmed our time correction routines by comparing our results with those produced by Eastman et al. (2010)'s freely available IDL routine `JDUTC2JDTDB.pro`. Our tests showed agreement at the microsecond level, which is safely below the levels of any experimental errors in our data.

Chapter 3

The Transit Model

As defined in Chapter 1, a transit is an eclipse event where the planet obscures part of the stellar disk from the point of view of the observer. The u-shaped transit lightcurve results from the blocking of stellar flux as the planet crosses the face of the star (see Figure 3.1).

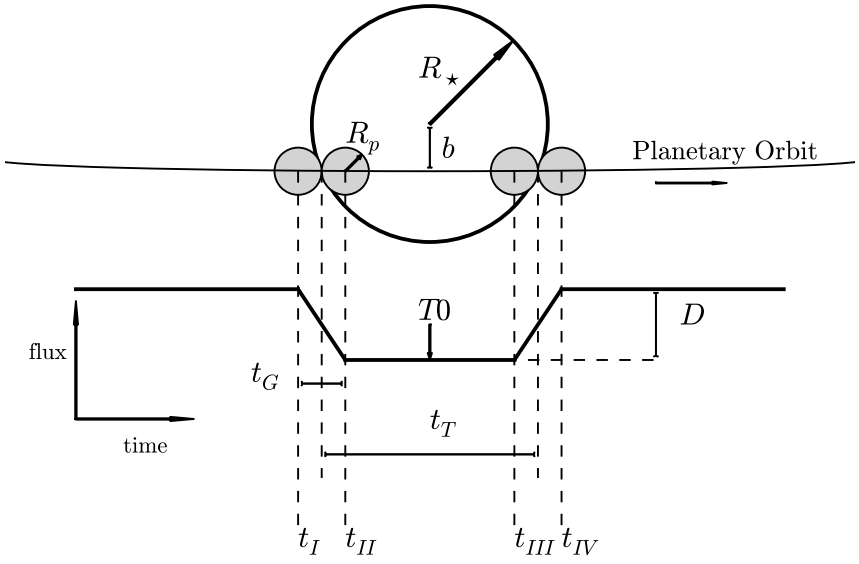

Figure 3.1: A diagram representing a transit event (top) and the corresponding lightcurve shape (bottom).

At any given point in the transit, the fractional stellar flux lost due to obscuration is roughly equal to the area of overlap between two circles with radii corresponding to the star ($R_\star$) and planet (R_p). The time-dependence of the flux simply reflects the overlap between the planetary and stellar disks due to their relative motions. The top half of Figure 3.1 diagrammatically represents the planet transit, and the bottom half roughly shows the resulting lightcurve as flux vs. time. The large circle represents the stellar disk, and the four small gray circles represents the transiting planet at the four times of contact, t_I, t_{II}, t_{III} and t_{IV}. Points t_I and t_{II} represent the times when the planet has begun to cross the limb of the star and when it has completely crossed the limb respectively. This portion of the lightcurve, where the planet is entering the stellar disk is called the ingress. The portion when it exits the disk between t_{III} and t_{IV} is the egress. The points t_{III} and t_{IV} represent the times when the planet has begun to cross beyond the limb of the star and when it has completely exited the stellar disk respectively. The planetary radius (R_p), stellar radius ($R_\star$) and the impact parameter b are also marked on Figure 3.1. The line passing through the gray circles represents the orbital path of the planet (also marked is the direction of orbital motion).

Below the diagram of the transit event is a rough representation of the observed flux as a function of time (the lightcurve). The four contact points are mapped from the diagram onto the lightcurve showing when the flux changes during ingress and egress. One must note that real observations of transits never have the trapezoidal shape shown in Figure 3.1 for two reasons. (i) The area of overlap for two circles does not vary linearly even when the orbital motion causing the overlap is uniform (Mandel & Agol, 2002). In addition the assumption of uniform orbital motion is not accurate. (ii) The radial brightness profiles for stars are not constant, but rather darkened near the limbs. This physical effect is called limb-darkening, and is a result of the observer's slanted view through lower density and hence lower surface brightness regions of the stellar atmosphere at the limbs. An optically thick cool layer of the

photosphere has a lower surface brightness than an optically thick hot surface, as is the case when comparing a view through the limb and the center of the star. A variety of models can be used to account for the brightness variation of the stellar disk. The quadratic limb-darkening law, where the brightness profile drops off roughly as: $I \propto 1 - u_1(1-\mu) - u_2(1-\mu)^2$, is the most commonly used (Mandel & Agol, 2002); here I is the brightness, $\mu \equiv \sqrt{1-r^2}$, where r is the radial distance from the center of the stellar disk in $R_\star$ units. The coefficients u_1 and u_2 are the quadratic limb-darkening coefficients (same as γ_1 and γ_2 in, Mandel & Agol, 2002). In addition to modifying the shapes of the ingress and egress portions of the lightcurve, limb-darkening also adds a curvature to the transit trough. So the transit trough is not truly flat as represented in Figure 3.1.

The center of the transit is marked in the figure by the mid transit time ($T0$) and is typically assumed to correspond to the point of conjunction, where the planet and star are exactly aligned with the line of sight to the observer. If the transiting planet has an eccentric orbit, and the point of conjunction is not aligned with the periapse, the duration of ingress ($t_i = t_{II} - t_I$) and egress ($t_e = t_{IV} - t_{III}$) are generally unequal. Winn (2010) shows that the differences between these durations can be approximated by $\frac{t_e - t_i}{t_e + t_i} \sim e\cos(\omega)\left(\frac{a}{R_\star}\right)^{-3}(1-b^2)^{3/2}$. Here e, ω, and b are the orbital eccentricity, the argument of periapse and the impact parameter respectively. The terms associated with these factors are typically on the order of one or less. The only significant term is the one with $a/R_\star$ – the semi-major axis represented in stellar radius units. The term $(a/R_\star)^{-3}$ is negligible for most systems. More than 85% of known transiting planets have $a/R_\star \geq 5$ (Wright et al., 2011, as of Apr-24-2011), which corresponds to differences in ingress and egress duration $< 0.8\%$. When modeling transit lightcurves, these differences are typically ignored unless it known that the system has non-zero eccentricity (e.g. from RV measurements). For the case of circular orbits $t_i \approx t_e \equiv t_G$, where t_G is referred to as the ingress/egress duration or the limb-crossing duration (sometimes noted as τ, Carter et al., 2008; Winn, 2010). The systems monitored by

APOSTLE all have sufficiently large values of $a/R_\star$ and have RV measurements which do not indicate eccentric orbits. The transit duration (t_T) is the duration between mid ingress and mid egress ($t_{IV} - t_I - t_G$) (shown in Figure 3.1, which one must note is different from total duration of the transit ($t_{IV} - t_I$). The variable t_T is sometimes denoted as T (Carter et al., 2008; Winn, 2010). In the limit of circular orbits ($e = 0$), a small planetary size in comparison to the star ($R_p \ll R_\star$) and a large planet to star separation with respect to the stellar radius ($R_\star \ll a$) the two parameters t_G and t_T can be approximated as,

$$t_G = 2\frac{R_p}{v\sqrt{1-b^2}} \tag{3.1a}$$

$$t_T = 2\frac{R_\star}{v}\sqrt{1-b^2} \tag{3.1b}$$

where the orbital speed $v = 2\pi a/P$ and the impact parameter $b = a\sin i_{\rm orb}/R_\star$. The terms a, P, $i_{\rm orb}$, R_p and $R_\star$ are the semi-major axis, orbital period, inclination, planetary radius and stellar radius respectively (Carter et al., 2008).

Finally, the difference between the flux level at the trough of the transit and the out-of-eclipse flux level is the transit depth (D). As mentioned earlier, the limb-darkening profile of the star affects the trough of the transit, making it curved rather than flat. In this regard, the parameter D simply represents the maximum depth of the trough at conjunction, which depends on the ratio of the area of the disks of the planet to the star ($R_p^2/R_\star^2$) and the ratio of the disk-averaged stellar intensity at conjunction $I(b)$ to the un-obscured disk-averaged intensity at conjunction for an impact parameter of zero, $I(0)$. The transit depth D is:

$$D = \frac{R_p^2}{R_\star^2}\frac{I(b)}{I(0)} \tag{3.2a}$$

the term I(b)/I(0) can be replaced by the quadratic limb-darkening profile (Mandel & Agol, 2002) to give

$$D = \frac{R_p^2}{R_\star^2}\frac{(1-u_1(1-\sqrt{1-b^2})-u_2(1-\sqrt{1-b^2})^2)}{(1-\frac{u_1}{3}-\frac{u_2}{6})} \tag{3.2b}$$

We developed a transit model called `MultiTransitQuick` in PYTHON, which is based on the analytic lightcurve models presented in Mandel & Agol (2002), and the PYTHON implementation of some of its functions (from EXOFAST by Eastman et al., 2012). We wrote two versions of `MultiTransitQuick` (MTQ), one designed to fit transits observed with different filters, and the other designed to look for variations in the transit depth.

If one makes transit observations using filters of different wavelength, the resulting set of transit lightcurves must be analyzed using a model which accounts for the different limb-darkening profiles, and differing transit depths extant in the data. The standard set of parameters used for Multi-Filter version of MTQ is $\boldsymbol{\theta}_{\text{Multi-Filter}} = \{t_T,\, t_G,\, D_{j...N_F},\, v_{1,j...N_F},\, v_{2,j...N_F},\, T_{i...N_T}\}$, where T_i are the transit times, and the terms v_1 and v_2 are linear combinations of the quadratic limb-darkening coefficients; $v_1 = u_1 + u_2$ and $v_2 = u_1 - u_2$. These linear combinations were used while fitting the lightcurves, since it is known that directly fitting for limb-darkening coefficients results in strongly anti-correlated error distributions for various transit parameters (Brown et al., 2001) and can hinder the chances of various model fitting routines from converging to accurate values (more in Ch. 4). Henceforth the quadratic limb-darkening coefficients u_1 and u_2 will be collectively referred to as LDC-u, and their linear combinations v_1 and v_2 will be referred to as LDC-v, where LDC stands for Limb-Darkening Coefficients. The subscripts $i...N_T$ and $j...N_F$ are used to denote multiple transits (N_T) and multiple filters (N_F) respectively.

Variations in transit depth can arise due to several reasons. A commonly invoked source of such variations are starspots (cool photospheric regions) and faculae (hot photospheric regions) (Pont et al., 2007; Lanza et al., 2009; Knutson et al., 2011, and many more). Starspots on the visible face of the star lower the disk-averaged brightness of the star; see panel (a) in Figure 3.2. The appearance and disappearance of spots on the stellar surface due to rotation or stellar activity cycles would result in variations in the transit depth. Transits occurring across the spot-less stellar surface

will be shallower than when active regions exist on the visible face of the star, assuming the spots are cooler than the stellar surface. If such spots lie at a latitudes coincident with the transit chord, and the spot-coverage is more localized the transiting planet may occult the spot and result in a small rise in the transit lightcurve (see panel (b) in Figure 3.2). Conversely, if these active regions are hot spots, the transit depth, and spot-crossing features in the lightcurve would change in the opposite manner.

Other sources for transit depth variations include, planetary oblateness, spin precession (Carter & Winn, 2010), planetary rings (Barnes & Fortney, 2004), and satellites (Sartoretti & Schneider, 1999; Tusnski & Valio, 2011). The wide variety of proposed sources of transit depth variation means there may be several degeneracies to resolve if a transit depth variation is indeed detected. Nonetheless, understanding such phenomena may only be possible by looking for statistically significant measurements showing variable transit depths. The multi-filter capability of MTQ can be modified to fit for the depth of each transit as a unique parameter. In this case the set of parameters used is $\boldsymbol{\theta}_{\text{Multi-Depth}} = \{t_T, t_G, D_{i...N_T}, v_{1,j...N_F}, v_{2,j...N_F}, T_{i...N_T}\}$, where D_i is now fit for each transit instead of each filter. However, the filters corresponding to each depth is still tracked as the model needs to convolve the limb-darkening profile to correctly reproduce the full lightcurve profile.

3.1 Derived System Parameters

MTQ internally computes several properties of the system, including the orbital period P, the planet-to-star radius ratio ($R_p/R_\star$), $a/R_\star$ (p. 2 and p. 3) and the orbital inclination i_{orb}, which are all needed to generate the model lightcurves. The period is the most straightforward to compute as it depends only on the transit times (T_i). Under the assumption that any timing variations which may exist in the data are small (*i.e.* TTV $<<$ P) or non-existent the orbital period can be determined by fitting a

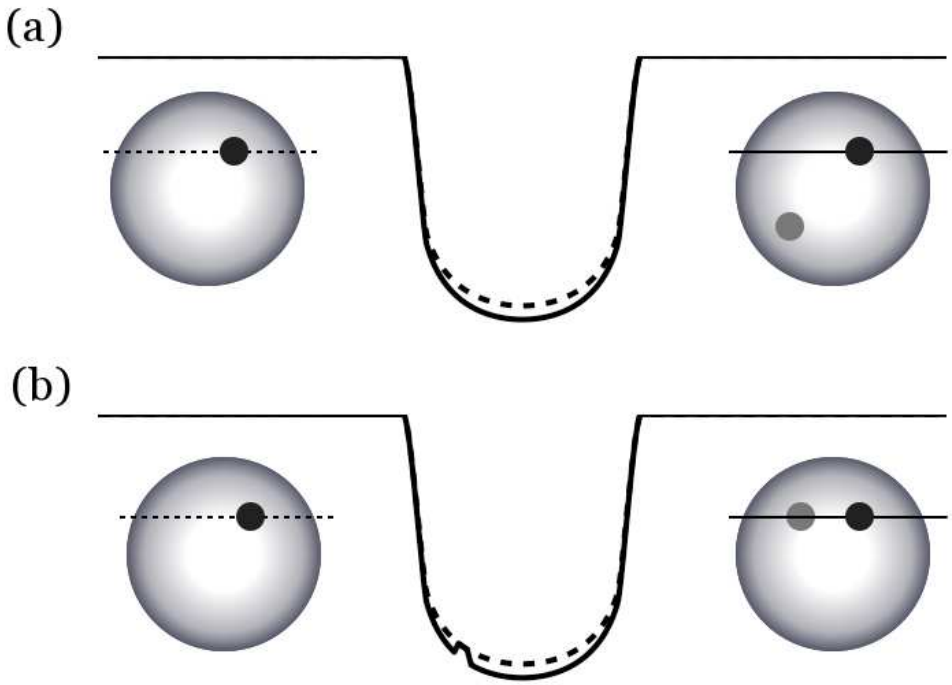

Figure 3.2: A Diagram representing how transit lightcurves are affected by star-spots. The top half (a) shows the case where the planet transits the spotless (dashed line transit; transit geometry shown on left) and spotted star but without crossing the spot (solid line transit; transit geometry shown on right). The resulting difference is just a change in the transit profile and transit depth. The bottom half (b) shows the case where, again, the planet transits the spotless (dashed line transit; transit geometry shown on left) and also crosses the spot (solid line transit; transit and spot-crossing geometry shown on right). In this case, in addition to a change in the transit profile (due to the presence of the spot) there is also a slight rise when the planet crosses the spot.

linear ephemeris (using the known transit epochs) to the transit times.

$$T_i = T0 + \mathrm{Epoch}_i \times P \tag{3.3a}$$

where P is the orbital period to be fit, Epoch_i is the known transit number, with respect to a zero-point transit time $T0$. The radius ratio $R_p/R_\star$ can be determined

from Eq. 3.1a, 3.1b and 3.2b. The impact parameter can be written in terms of t_G, t_T and $R_p/R_\star$ by diving Eq. 3.1a and 3.1b and rearranging to give:

$$b = \sqrt{1 - (t_T/t_G)(R_p/R_\star)} \tag{3.3b}$$

Substituting this expression in Eq. 3.2b results in a sextic (sixth order polynomial) function in $(R_p/R_\star)^{1/2}$. Given the model parameters t_G, t_T and D_j, one can get $R_p/R_\star$ from the roots to the sextic. However, this poses a problem to fitting multi-filter data since there will be multiple D_j values and hence the routine will produce multiple radius ratios. The expressions for several orbital parameters computed internally need $R_p/R_\star$, so in essence multi-filter data will produce multiple orbital parameters for the same system. To circumvent this problem, MTQ requires the user to designate one filter as the "reference" filter and $R_p/R_\star$ and all the dependent orbital parameters are computed only using $D_{\rm reference}$. Generally observations in a filter least affected by limb-darkening (typically at longer wavelengths), allow accurate estimates of $R_p/R_\star$ and serve well as reference filters. When fitting for multiple depths ($\boldsymbol{\theta}_{\rm Multi\text{-}Depth}$) a reference transit is designated instead of a reference filter. In this case, the lightcurve with the most complete in-eclipse data and low residual scatter at a red observed wavelength, is chosen as the reference. Once $R_p/R_\star$ is computed, one can compute the normalized orbital speed (Carter et al., 2008),

$$\frac{v}{R_\star} = 2\sqrt{\frac{(R_p/R_\star)}{t_T t_G}} \tag{3.3c}$$

the semi-major axis $a/R_\star$ in stellar radius units,

$$\frac{a}{R_\star} = \frac{P}{2\pi}\frac{v}{R_\star} \tag{3.3d}$$

which with the impact parameter (Eq. 3.3b) gives the orbital inclination,

$$i_{\rm orb} = \arccos\left(\frac{b}{a/R_\star}\right) \tag{3.3e}$$

and finally, using Kepler's 3rd law, we can write an expression for the average stellar density ($\rho_\star$) in terms of system parameters derived from transit lightcurves (Seager & Mallén-Ornelas, 2003),

$$\rho_\star = \frac{3\pi}{GP^2}\left(\frac{a}{R_\star}\right)^3 \tag{3.3f}$$

where G is the universal gravitational constant. We used `MultiTransitQuick` to run the analysis on APOSTLE data. The analyzer which utilizes `MultiTransitQuick` is described in the following chapter (Ch. 4). The results from this transit model on APOSTLE data are described in Ch. 5, 6 and 7.

Chapter 4

Transit MCMC

Bayes' theorem relates the conditional probability $\mathcal{P}(\boldsymbol{\theta} \mid \boldsymbol{d})$ to the converse conditional probability $\mathcal{P}(\boldsymbol{d} \mid \boldsymbol{\theta})$, and independent probabilities $\mathcal{P}(\boldsymbol{\theta})$ and $\mathcal{P}(\boldsymbol{d})$ of two events $\boldsymbol{\theta}$ and $\boldsymbol{d}$ respectively:

$$\mathcal{P}(\boldsymbol{\theta} \mid \boldsymbol{d}) = \frac{\mathcal{P}(\boldsymbol{\theta})\mathcal{P}(\boldsymbol{d} \mid \boldsymbol{\theta})}{\mathcal{P}(\boldsymbol{d})} \tag{4.1}$$

where the conditional probability $\mathcal{P}(\boldsymbol{\theta} \mid \boldsymbol{d})$ is defined as the probability of occurrence of event $\boldsymbol{\theta}$ given the knowledge that the *related event* $\boldsymbol{d}$ has occurred. This definition also applies to the converse conditional probability $\mathcal{P}(\boldsymbol{d} \mid \boldsymbol{\theta})$. The independent probabilities $\mathcal{P}(\boldsymbol{\theta})$ and $\mathcal{P}(\boldsymbol{d})$ are defined as the probabilities of the events $\boldsymbol{\theta}$ and $\boldsymbol{d}$ occurring independently from the other.

Bayes' theorem can be used to fit models to data via a series of techniques called Bayesian inference. These techniques are, in essence, agents for hypothesis testing, where $\boldsymbol{d}$ are the observed data and $\boldsymbol{\theta}$ are a set of proposed model parameters. In Bayesian inference, the conditional probability $\mathcal{P}(\boldsymbol{\theta} \mid \boldsymbol{d})$ term on the LHS of Eq. 4.1 is called the posterior probability and quantifies the uncertainties in the model parameters given the observed data. The challenge for the technique is to constrain the posterior probability from the joint probability, $\mathcal{P}(\boldsymbol{\theta})\mathcal{P}(\boldsymbol{d} \mid \boldsymbol{\theta})$, sometimes also referred to as the likelihood function. Bayesian inference techniques like Markov Chain Monte Carlo (MCMC) are widely used for this purpose. Since the analytic evaluation of Eq. 4.1 is challenging, Markov chains are used to sample parameter space, evaluate the local likelihood function and numerically map the posterior probability distribution. MCMC implementations are now the standard for modeling data on exoplanets

(Ford, 2005; Holman et al., 2006; Collier Cameron et al., 2007b; Kundurthy et al., 2011; Gazak et al., 2011) and several other applications.

We developed an MCMC routine called Transit MCMC (`TMCMC`), which is designed to work in conjunction with `MultiTransitQuick`. However, it can also be used to fit other models and data easily. The core `TMCMC` routine uses the Metropolis-Hastings (M-H) algorithm, and is based on its implementation for astronomical data, as described by Tegmark et al. (2004) and Ford (2005). In the standard formalism of M-H, the term $\mathcal{P}(\boldsymbol{\theta})\mathcal{P}(\boldsymbol{d} \mid \boldsymbol{\theta})$ in Eq. 4.1 (the likelihood term), is proportional to $e^{-\chi^2/2}$. The denominator $\mathcal{P}(\boldsymbol{d})$ is simply a scaling factor and may be ignored. The Markov chain is computed by making jumps in parameter space and selecting those jumps which tend toward regions of parameter space at lower χ^2. Jumps from the j^{th} step in the chain are made with the following equation:

$$\boldsymbol{\theta}_{j+1} = \boldsymbol{\theta}_j + \mathcal{G}(0, \boldsymbol{\sigma}_\theta^2) f \tag{4.2}$$

where $\boldsymbol{\theta}$ and $\boldsymbol{\sigma}_\theta$ are the vectors of model parameters and their associated step-sizes respectively. The term $\mathcal{G}(0, \sigma_\theta^2)$, referred to as the proposal distribution, is a random number drawn from a normal distribution with a mean of 0 and a variance of σ_θ^2. It is customary to use a Gaussian proposal distribution but this is not mandatory. Additional modifications, such as applying bounds to keep parameter values realistic, are often applied. In the M-H algorithm a given trial step ($\boldsymbol{\theta}_{j+1}$) is selected if the acceptance probability ($e^{-\Delta\chi^2(\boldsymbol{\theta})}$) is greater than a random variable drawn from a uniform distribution (see, Ford, 2005, for the uniform prior of $\boldsymbol{\theta}$). Making step selections this way results in a situation where jumps towards regions of low χ^2 (good fits) occur more often than jumps towards regions of high χ^2 (poor fits). The factor f is an adaptive step-size controller which is used to guide the chain to an optimal acceptance rate (Collier Cameron et al., 2007b). Statisticians have shown that the optimal acceptance rate for chains that step through one parameter is 44% and when multiple parameters are stepped through simultaneously this rate is closer to 23%.

Running chains close to the optimal acceptance rates result in evenly sampled posterior distributions (Gelman et al., 2003). In `TMCMC` the desired acceptance rates are achieved by adjusting the step-size controller (f) every 100 accepted steps according to $f_{\rm new} = W(f_{\rm old}/N_{\rm trials})$, where $N_{\rm trials}$ are the number of steps attempted for the last 100 accepted steps and W is a scaling factor which is 225 or 434 for single-parameter or multi-parameter chains respectively (as noted in, Collier Cameron et al., 2007b). Given sufficient time, a chain will sample parameter space such that the ensemble of the points from a converged chain accurately represent the posterior distributions (*i.e.* the uncertainties) of the parameters in set $\boldsymbol{\theta}$ given the observed data $\boldsymbol{d}$.

4.1 Markov Chains for MTQ

For APOSTLE data sets, we explored system parameters using three different kinds of chains. Two of these were based on the Multi-Filter parameter set $\boldsymbol{\theta}_{\rm Multi\text{-}Filter}$ described in Ch. 3; First, with Fixed Limb-Darkening Coefficients, and second, with Open Limb-Darkening Coefficients. For the Fixed LDC chains, the coefficients were simply fixed to values tabulated for the appropriate observing filter (Claret & Bloemen, 2011). For the Open LDC chains, the limb-darkening coefficients v_1 and v_2 are allowed to float. It has been shown that measured limb-darkening coefficients from high precision studies are in good agreement with tabulated values (Brown et al., 2001; Tingley et al., 2006). Another study using spectrophotometry from *HST* STIS showed that any variations in the estimate of transit parameters due to inaccurate limb-darkening are lower than the 1-σ uncertainty, with greater disagreement seen at shorter wavelengths (Knutson et al., 2007). Ground-based observations typically cannot achieve the level of photometric precision of space-based studies, hence constraining the limb-darkening from transit observations is difficult. Subtle inaccuracies in the fit limb-darkening profile can lead to incompatible estimates of system parameters, especially at short wavelengths (Kundurthy et al., 2011). In effect, the purpose of the Fixed LDC and Open LDC chains is simply to compare the differences in the fit

limb-darkening coefficients to the tabulated values. The third type of Markov chain was run on the Multi-Depth parameter set $\boldsymbol{\theta}_{\text{Multi-Depth}}$ described in Ch. 3. APOSTLE lightcurves were gathered over a long time-baseline, and statistically significant depth variations seen in the data may help shed light on the various phenomena responsible for depth variations (see Ch. 3).

Table 4.1: Bounds applied for MTQ in `TMCMC`

Bounds	Notes
$t_T > 0$	Non-zero transit duration
$t_G > 0$	Non-zero limb-crossing duration
$D > 0$	Non-zero transit depth
$1 - b^2 > 0$	Impact parameters less than 1 (primary condition for transit)
$b/(a/R_\star) \leq 1$	Ensures real values for orbital inclination
$0 < u_1 < 1$	Reasonable limb-darkening coefficients*
$0 < u_2 < 1$	Reasonable limb-darkening coefficients*

*applied when parameters were fit (OLDC chains)

We applied bounds to several transit parameters and combinations of transit parameters in MTQ (as shown in 4.1). Most of these bounds were simply to check if the parameters had values that were physically realistic. For most parameters it was quite rare that the MCMC chains got close to the bounding limits, since the chains spend most of their time near low χ^2 regions; parameter values near the bounds for the APOSTLE systems usually yield poor fits. When fitting for the limb-darkening however, the degeneracies proved very significant, and the Markov chains often strayed to unrealistic values. For example u_1 and u_2 took on values which would suggest limb-brightening rather than limb-darkening, either as a result of noisy data or due to gaps in the ingress or egress portions of the lightcurve. Limb-brightening

is considered unphysical for broadband observations. Thus, after every jump (Eq. 4.2), the vector of proposal parameters $\boldsymbol{\theta}_{j+1}$ is run through a series of sub-routines in MTQ, to check if any of the conditions in Table 4.1 are violated. If these any one of these conditions are violated, the vector is discarded and a new vector is generated. `TMCMC` carries out this check until agreeable values emerge, and then continues with the rest of the algorithm.

The observed data used as input to `TMCMC` are not detrended. This is due to the fact that, for a given night, the observed data first need to be normalized by a model lightcurve. The residuals are then used to determine the detrending coefficients and the correction function (c_k and $F_{\rm cor}$ respectively; see Eq. 2.8a and 2.8b). Since `TMCMC` steps through several proposed parameter values, these residuals need to be determined at every step to ensure $F_{\rm cor}$ is coupled to the best-fit model determined in the Markov chain. So after a proposed parameter vector ($\boldsymbol{\theta}_{j+1}$) is generated, the resulting set of model lightcurves from each night (M_i) are used to normalize the appropriate observed (un-detrended) lightcurves (O_i). The residuals are used to fit for the coefficients of the correction function ($F_{{\rm cor},i}$) for each night. At every step in the MCMC, the observed data, model lightcurves and correction functions for all nights are stacked as follows:

$$\begin{aligned}
\mathbb{O} &= [O_1, O_2, O_3, ...O_{N_T}] \\
\boxminus &= [\sigma_1, \sigma_2, \sigma_3, ...\sigma_{N_T}] \\
\mathbb{M}(\boldsymbol{\theta}) &= [M_1, M_2, M_3, ...M_{N_T}] \\
\mathbb{F}_{\rm cor} &= [F_{{\rm cor},1}, F_{{\rm cor},2}, F_{{\rm cor},3}, ...F_{{\rm cor},N_T}]
\end{aligned}$$

where $\mathbb{O}$ and $\boxminus$ are the stacked observed data and associated errors, and the model and detrending correction functions are in the stacks $\mathbb{M}$ and $\mathbb{F}_{\rm cor}$ respectively. N_T is the number of transits. The χ^2 is computed using the stacked arrays;

$$\chi^2 = \sum_k^{N_{\rm all}} \frac{(\mathbb{O}_k - \mathbb{M}_k - \mathbb{F}_{{\rm cor},k})^2}{\boxminus_k^2} \tag{4.3}$$

where k is the index which counts over the total number of data points ($N_{\rm all}$) in the stacked arrays.

4.2 Executing and Analyzing Chains

By varying the entire vector of model parameters, and applying a single step-size modifier (Eq. 4.2), we run the risk of using mismatched step-sizes and hence under-sampling the posterior distributions of some parameters. As mentioned before, it is known that well-constructed chains will properly sample posterior distributions given the correct acceptance rate (Gelman et al., 2003). However, the acceptance rate is guided by the location of the chain in parameter space, as steps in low probability (large χ^2) regions of parameter space are accepted less often than those in high probability regions. For example, if we make a poor choice and select a starting step-size for one parameter to be too large relative to the other parameters in the ensemble, the Markov chain for this parameter will traverse between regions of high and low probability faster than the rest. The adjustments to the acceptance rate f in the Markov chain will be biased by jumps in only this parameter, and the posterior distributions for the remaining parameters will be poorly sampled. The key to a well-constructed chain is to choose the relative starting step-sizes, for the parameter ensemble, such that they *all* roam high and low probability regions of parameter space at roughly the same rate. Determining a reasonable set of starting step-sizes is done by running short exploratory Markov chains (40,000 steps) for each model parameter (holding all others fixed). If these exploratory chains have not stabilized to the optimal acceptance rate of $\sim 44\%$ (as noted by Gelman et al., 2003, for single parameter chains) at the end of 40,000 steps, the chain is run until this rate is achieved. The jump sizes near the end of stabilized exploratory chains are then used as the starting steps for the multi-parameter chains. These multi-parameter chains will also be referred to as 'long chains' from now on.

For each transiting system, we ran long chains of 2×10^6 steps from two differ-

ent starting locations for each model scenario, Fixed LDC, Open LDC and Multi-Depth/Fixed LDC. After completion we (1) cropped the initial stages of these chains to remove the burn-in phase, where the chain is far from the best-fit region, and (2) we exclude the stage where the chain is far from the optimal acceptance rate of 23± 5% (as noted for multi-parameter chains Gelman et al., 2003). We run three types of post-processing on the chains after cropping: (a) We compute the ranked and unranked correlations in the chains of every fit parameter with respect to the others. These statistics simply provide an estimate of the level of degeneracy between parameters in a given model. The next two post-processing steps employ two commonly used diagnostics to check for chain convergence, namely (b) computing the auto-correlation lengths and (c) the Gelman-Rubin $\hat{\mathrm{R}}$-static values (Gelman & Rubin, 1992).

In a Markov chain, as a given step is only dependent on the preceding step, you are likely to have sections in the chain were the points show trends (*i.e.* are correlated). The correlation length signifies the interval at which sampled points in a Markov chain will be uncorrelated. The effective length is the total number of points in the chain divided by the correlation length. Short correlation lengths (*i.e.* large effective lengths) indicate that the MCMC ensemble represents a statistically significant and hence more precise sampling of the posterior distribution (Tegmark et al., 2004). The $\hat{\mathrm{R}}$-statistic is computed using multiple chains of the same parameter set which have different initial conditions. An $\hat{\mathrm{R}}$-statistic close to 1 (to within 10%) indicates that all chains have converged, cover approximately the same region of parameter space, and that the relevant parameter space has been sufficiently explored.

4.3 TAP: Red Noise Analysis and Transit Times

It has been noted by Carter & Winn (2009) that transit lightcurves lacking any significant "defects" or artificial trends can have correlated noise buried within the overall scatter, which is invisible to visual examination. They test a wavelet based

red-noise model on simulated transit lightcurves with and without artificial red-noise and find that models which do not fit for red-noise are subject to inaccuracies in transit parameters on the order of 2-3σ and tend to have underestimated errors by up to 30%. For transit timing studies, poor estimates such as these are cause for concern, since smaller errors and large deviations from the expected time can easily lead to false claims of TTVs. The detrending routine within `TMCMC` removes long-term trends related to instrumental or other nuisance parameters. We visually examined the residuals of APOSTLE lightcurves (those observed during good conditions), and noted that the data may still have low-level correlated noise, even after detrending. The Transit Analysis Package (TAP Gazak et al., 2011) implements the red-noise model of Carter & Winn (2009). We ran separate fits of transit parameters using TAP on the *detrended* lightcurves from our `TMCMC` fit.

The typical TAP parameter set is: $\boldsymbol{\theta}_{\rm TAP} = \{a/R_\star,\ i_{\rm orb},\ (R_p/R_\star)_{i...N_F},\ T_{i...N_T},\ \sigma_{({\rm white},i...N_T)},\ \sigma_{({\rm red},i...N_T)}\}$, where $\sigma_{({\rm white},i...N_T)}$ and $\sigma_{({\rm red},i...N_T)}$ are the white-noise and red-noise levels for N_T transits respectively. The TAP package does not fit for the period using the transit times, and often yields poor estimates of the period, so we fixed the period to the estimate from the `TMCMC` fit. The limb-darkening was fixed to values from the literature. The orbital eccentricity and argument of periastron were kept fixed at 0, for the three APOSTLE targets.

One must also note a pitfall of the Carter & Winn (2009) red-noise model. Their fitting function expects the white-noise and red-noise components of a given lightcurve to be stationary, *i.e.* there are no temporal variations in the Gaussian white-noise level and the red-noise's power-spectrum amplitude with time. They note that more elaborate noise models may be required to account for the fact that real data do not conform to these requirements. Typically the scatter is increased (due to lower signal-to-noise) at the portion of the lightcurve where the sky brightness is higher (e.g. data taken close to twilight). Variable observing conditions may alter not just the white-noise properties of a lightcurve but also result in red-noise that is more

complex than what can be described by Carter & Winn (2009)'s wavelet model. In addition, at the 1000 ppm level stellar variability is not understood; it is reasonable to assume the star contributes to the correlated noise in the lightcurve. In spite of these caveats, the TAP red-noise analysis serves as an good secondary check to results derived using `TMCMC` (which does not account for red-noise).

The following chapters outline the results from our analysis using `MultiTransitQuick` with `TMCMC` and the TAP models on the APOSTLE targets GJ 1214b, XO-2b and TrES-3b.

Chapter 5

GJ 1214b: A Super-Earth Around an M-dwarf

Our solar system has planets that can be classified into two broad categories; terrestrial (or rocky) and gaseous. There lies a gap in planetary mass and size between these two regimes, with the Earth being the largest and most massive terrestrial planet and Uranus and Neptune being the least massive and smallest gaseous planets respectively; $M_{\rm Uranus} \sim 15 {\rm M}_{\oplus}$, and $R_{\rm Neptune} \sim 3.9$ R$_{\oplus}$. It was not until 2009 that the first exoplanets in the intermediate regime were discovered via the transit method, namely *CoRoT*-7b (Léger et al., 2009; Queloz et al., 2009) and GJ 1214b (Charbonneau et al., 2009). This class of planets have since gained the title of "Super-Earth" and have no analog in the solar system. Even though there were several RV discoveries prior to 2009 of planets with minimum masses in the Super-Earth range ($1 {\rm M}_{\oplus} < M_p \sin(i_{\rm orb}) < 10 {\rm M}_{\oplus}$), transit discoveries offered the first confirmation that such a class existed; mainly due to the fact that the inclination can be constrained from transits and hence the mass-inclination degeneracy ($M_p \sin(i_{\rm orb})$) from RV observations is removed. Using both RV and transits allows for the complete characterization of masses and radii of planets. The discovery of Super-Earths holds clues to the transition between the terrestrial and gas-giant planet classes seen in our solar system. Theoretical considerations have predicted that during planet formation, a protoplanetary core of roughly ~ 10 M$_{\oplus}$ would be required to trigger rapid gas accretion to form a gaseous planet (Pollack et al., 1996). Some predictions place this critical mass as low as 2 M$_{\oplus}$ (Ikoma et al., 2001) or as high as 16 M$_{\oplus}$ (Lissauer et

al., 2009). The value of 10 $M_\oplus$ (seen as a sort of median of theoretical predictions), is often quoted in the literature as the boundary core-mass for terrestrial and gaseous worlds, but should not be considered a true boundary.

The largest size a $10M_\oplus$ planet could have, given the equation of state of a single-element zero-pressure Hydrogen sphere, is roughly $6R_\oplus$ (Seager et al., 2007). Though the assumptions given are not realistic, they given an estimate of the upper size-limit for planets in the Super-Earth-mass range. The *Kepler* mission has discovered several planetary candidates with radii smaller than $6R_\oplus$ (> 1500, Batalha et al., 2012). Without considering any forthcoming false positive studies, this statistic shows that there are many systems which could be intermediate rocky-gaseous planets or rocky planets. Confirmed *Kepler* planets like Kepler-10b (Batalha et al., 2011), Kepler-11b,d,e,f (Lissauer et al., 2011a), Kepler-18b (Cochran et al., 2011) and Kepler-20b (Gautier et al., 2012) fall in the Super-Earth-mass range; interestingly these systems show a bewildering diversity of planetary compositions as inferred from their average densities. Other than these *Kepler* systems, the objects 55 Cnc e (McArthur et al., 2004; Queloz et al., 2009; Léger et al., 2009; Demory et al., 2011) and HD 97658b (Howard et al., 2011; Henry et al., 2011) are possible Super-Earths that have also been detected via transit.

GJ 1214b has been subject to several follow-up efforts since its discovery. Photometric follow-up confirmed the transiting nature of the system (Sada et al., 2010) and several additional lightcurves have shown that the host star may be active, as evidenced by signs of starspots, low energy flares and long-term flux modulations (Carter et al., 2011; Kundurthy et al., 2011; Berta et al., 2011; de Mooij et al., 2012). Transmission spectroscopy follow-up observations have been made in the optical (Bean et al., 2010) and the near-infrared (Crossfield et al., 2011; Croll et al., 2011; Bean et al., 2011; Berta et al., 2012). The resulting spectrophotometry in combination with photometry from *Spitzer* (Désert et al., 2011b) have shown that GJ 1214b has a remarkably flat spectrum (see Berta et al., 2012, for the plot of full spectral coverage).

The flat spectrum is best explained by an atmosphere for GJ 1214b whose major component is of large mean molecular weight (Berta et al., 2012). This type of atmosphere is consistent with the proposition by Rogers & Seager (2010) and Nettelmann et al. (2011) for a planet with an ice-rock core surrounded by an atmosphere of mostly sublimated ices (H_2O/CO_2) and a small amount of primordial gas (H/He).

APOSTLE observations of GJ 1214b have been previously published in Kundurthy et al. (2011). This dissertation contains new observations in addition to those published previously and describes a renewed analysis of these data with the Multi-Filter and Multi-Depth MTQ model.

5.1 Six Transits

The transit of GJ 1214b was observed 6 times during the Spring/Summer peak observing months for the object, in 2010 and 2011. A summary of its 6 r'–band observations is given in Table 5.1.

GJ 1214 is a M4.5V type main sequence star with a Johnson R mag of 13.8 (Monet et al., 2003), making it the faintest of all the APOSTLE targets. For the differential photometry, we used USNO-B1.0 0949-0280051, 95″ to the north of GJ 1214 as the comparison star. Our uncalibrated differential photometry showed that this object was a factor of $\sim$ 1.4 times brighter than GJ 1214 in the r'–band (see 'Flux Norm.' in Table 5.1), which is consistent with the comparison's Johnson R of 13.6 (Monet et al., 2003). The observing conditions for the six nights were mostly clear, resulting in complete lightcurves on all occasions. We used 45 second exposures for the first 3 nights, and mostly 75 second exposures for the final 3 GJ 1214 nights to reduce the effects of correlated noise. All lightcurves are shown in Figure 5.1. The observations on UTD 2010-04-21 (#1) showed a sharp rise in flux in the out-of-eclipse portion of the lightcurve. In addition, the nights of UTD 2010-06-06 (#2), 2011-05-26 (#4) and 2011-06-25 (#5) show (mostly positive) deviations from the transit shape during eclipse. These 4 features in the lightcurve do not correlate with trends in the

Nuisance, since they remain in place even after detrending. Although we cannot rule out the fact they could be associated with uncharacterized sources of correlated noise, the features in the lightcurve could be evidence for stellar activity. The feature in lightcurve #1 is similar to a minor flare event and the features in lightcurves #2, #4 and #5 could be spot-crossing events. These anomalous features are represented by open circles in Figure 5.1. Stellar activity is discussed further in § 5.3.

Table 5.1: APOSTLE Observing Summary for GJ1214

T#	UTD	Obs. Cond.	Filter	Exp.	Bin	Phot. Ap.	RMS (ppm)	%Rej.	Flux Norm.	Error Scaling
(1)	(2)	(3)	(4)	(5)	(6)	(7)	(8)	(9)	(10)	(11)
1	2010-04-21	Clear	r'	45	-	12	1044	2%	0.7195	1.3696
2	2010-06-06	Clear	r'	45	-	16	1357	1%	0.7138	1.5376
3	2010-07-06	Clear	r'	45	-	18	983	$< 1\%$	0.7026	1.1274
4	2011-05-26	Clear	r'	45,75	-	17	1040	4%	0.7214	1.5527
5	2011-06-25	Clear	r'	75	-	20	941	2%	0.7057	1.3436
6	2011-08-02	Clear	r'	75	-	30	638	8%	0.7203	0.7484

(1) Transit Number, (2) Universal Time Date, (3) Observing Conditions, (4) Observing Filter, (5) Exposure Time (seconds)

(6) Bin size in seconds, (7) Optimal Aperture Radius (pixels), (8) Scatter in the residuals

(9) % frames rejected due to saturation or other effects, (10) Flux normalization between the target and comparison star

(11) The factor by which the photometric errors were scaled

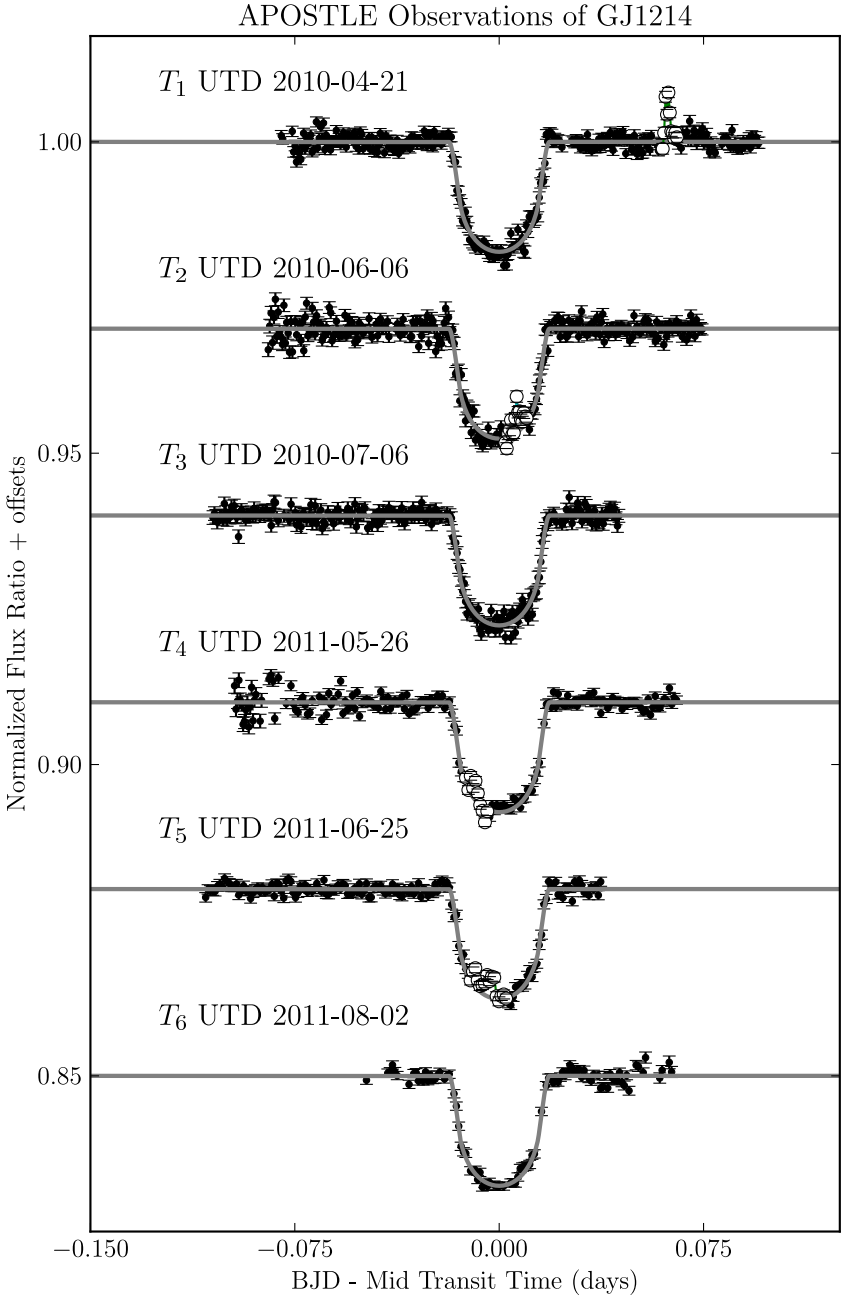

Figure 5.1: Six r' filter lightcurves of GJ 1214b, with time from mid-transit on the horizontal axis and the normalized flux ratio on the vertical axis. The grey line with the transit model was computed using the Fixed LDC parameters. The out-of-eclipse region of the lightcurve observed on UTD 2010-04-21 (#1) shows a possible flare marked by open circles. The in-eclipse portions of the lightcurves observed on UTD 2010-06-06 (#2), UTD 2011-05-26 (#4) and UTD 2011-06-25 (#5) show mostly positive deviations (open circles) from the transit shape that could be signs of planet-spot crossings.

5.2 System Parameters

We fit 3 lightcurve models for GJ 1214b as described in Ch. 4: the first two fits using (1) Fixed LDC and (2) Open LDC Multi-Filter $\boldsymbol{\theta}_{\text{Multi-Filter}}$ parameter sets, and the third using the Fixed LDC Multi-Depth model $\boldsymbol{\theta}_{\text{Multi-Depth}}$ parameter set, described in Ch. 3. Table 5.2 lists information for these three chains, such as the version of the chain ('Chain') the corresponding Model Vectors and the number of free parameters (N_{free}) in each set. All GJ 1214b chains use t_G, t_T and include the 6 transit times $T0_i$. In the Fixed LDC and Multi-Depth Fixed LDC chains the limb-darkening coefficients are held fixed at values taken from the literature (Claret & Bloemen, 2011). In the Open LDC chain the limb-darkening parameters are allowed to vary in the Markov chain optimization process.

Table 5.2: `TMCMC` Chains for GJ 1214

Chain	Model Vector	N_{free}	Chain Length	Corr. Length	Eff Length	χ^2	DOF
FLDC	$\boldsymbol{\theta}_{\text{Multi-Filter}}$	9	1,900,001	45	42,222	2057.23	1241
OLDC	$\boldsymbol{\theta}_{\text{Multi-Filter}}$	11	1,900,001	4,969	382	2056.89	1239
MDFLDC	$\boldsymbol{\theta}_{\text{Multi-Depth}}$	14	1,723,354	77	22,381	2040.57	1236

The remaining columns in Table 5.2 note various Markov chain statistics like the auto-correlation length ('Corr. Length') and effective length ('Eff. Length'); see p. 39. These statistics are computed for all free parameters in the chains and the parameter with the longest 'Eff. Length' (lowest statistical significance) is chosen to represent the robustness of the Markov chain. Effective lengths > 1000 are seen for both chains where the LDC's are fixed. As noted previously in Kundurthy et al. (2011) the r'–band limb-darkening is difficult to characterize using transit models. This is true in the reanalysis of GJ 1214b, as evidenced by the poor sampling of

posterior distributions in the Open LDC chain. The parameters with the lowest effective lengths in the open LDC chains were the limb-darkening coefficients $v_1(r')$ and $v_2(r')$. The final two columns list the goodness of fit (*i.e.* lowest χ^2 in the MCMC ensemble) and Degrees-of-freedom (DOF) from the respective chain. The resulting best-fit parameter estimates are listed in Table 5.3 for the Multi-Filter models, and in Table 5.4 for the Multi-Depth models. One must note that despite scaling the photometric errors by the factors shown in the last column of Table 5.1, the reduced χ^2 of the fits indicate an underestimation of error bars (χ^2/DOF ~ 1.7). We attribute this to the lower photometric precision for several of the 45 sec GJ 1214 lightcurves. For example, one can see greater scatter near the beginning of lightcurves #2 and #4 where the sky-brightness was larger.

The joint probability distributions (JPDs) from the Fixed LDC are plotted in Figure 5.2. There are no significant correlations between these parameters. The posterior probabilities of various system parameters derived from the JPDs in Figure 5.2 are plotted in Figure 5.3. Also overplotted are estimates of these same system parameters from other studies. Most system parameters are in good agreement except for the orbital period, due to the fact that accuracy in the estimated orbital period increases with the number of transit times measured. Hence, there are differences between the various estimates of the orbital period on the order of a few seconds. Due to the large number of transit times, we do not show them on the JPD plots. The transit times are among the least correlated of the parameters from the Markov chain analysis. The fits from the Multi-Depth chains and the evidence for stellar activity are discussed in § 5.3.

5.3 Stellar Activity

Evidence of spot-crossings or low energy flares in transiting systems have been noted by several studies (Pont et al., 2007; Silva-Valio, 2008; Dittmann et al., 2009; Basri et al., 2011; Walkowicz et al., 2011). For GJ 1214 in particular there have been several

Table 5.3: GJ 1214 Parameters for $\boldsymbol{\theta}_{\text{Multi-Filter}}$

Parameter	FLDC	OLDC	Unit
MTQ Parameters			
t_G	0.0042±0.0002	0.0042±0.0003	days
t_T	0.0326±0.0001	0.0326±0.0003	days
$D_{(\text{r'})}$	0.0177±0.0001	0.0177±0.0001	-
v_1(r')	(0.8885)	0.8502±0.0800	-
v_2(r')	(0.3843)	0.4962±0.1664	-
Derived Parameters			
$(R_p/R_\star)_{(\text{r'})}$	0.1166±0.0009	0.1169±0.0016	-
b	$0.29^{+0.06}_{-0.07}$	$0.30^{+0.08}_{-0.02}$	-
$a/R_\star$	14.73±0.30	14.73±0.34	-
i_{orb}	88.86±0.30	$88.82^{+0.05}_{-0.10}$	$^o(deg)$
$\nu/R_\star$	58.58±1.20	58.57±1.37	days^{-1}
$\rho_\star$	24.23±1.49	24.22±1.66	g/cc
P (1.5804 days +)	381±25	381±25	milli-sec

reports of activity and long-term flux modulations (Carter et al., 2011; Kundurthy et al., 2011; Berta et al., 2011; de Mooij et al., 2012). Many lower main-sequence stars are known to be magnetically active and low-mass stars are known especially for their variability as a result of this activity. Some of the most active M-dwarfs are believed to lie at masses below the transition between partially and fully convective stellar interiors ($< 0.35\text{M}_\odot$, Reiners & Basri, 2009). The increased activity is often thought to be a result of asymmetric magnetic field topologies for fully convective low mass stars. Although GJ 1214 ($0.153\text{M}_\odot$, Kundurthy et al., 2011) lies well within this mass range, it has been classified as an inactive M-dwarf by Hawley et al. (1996) based on the lack of Hα activity.

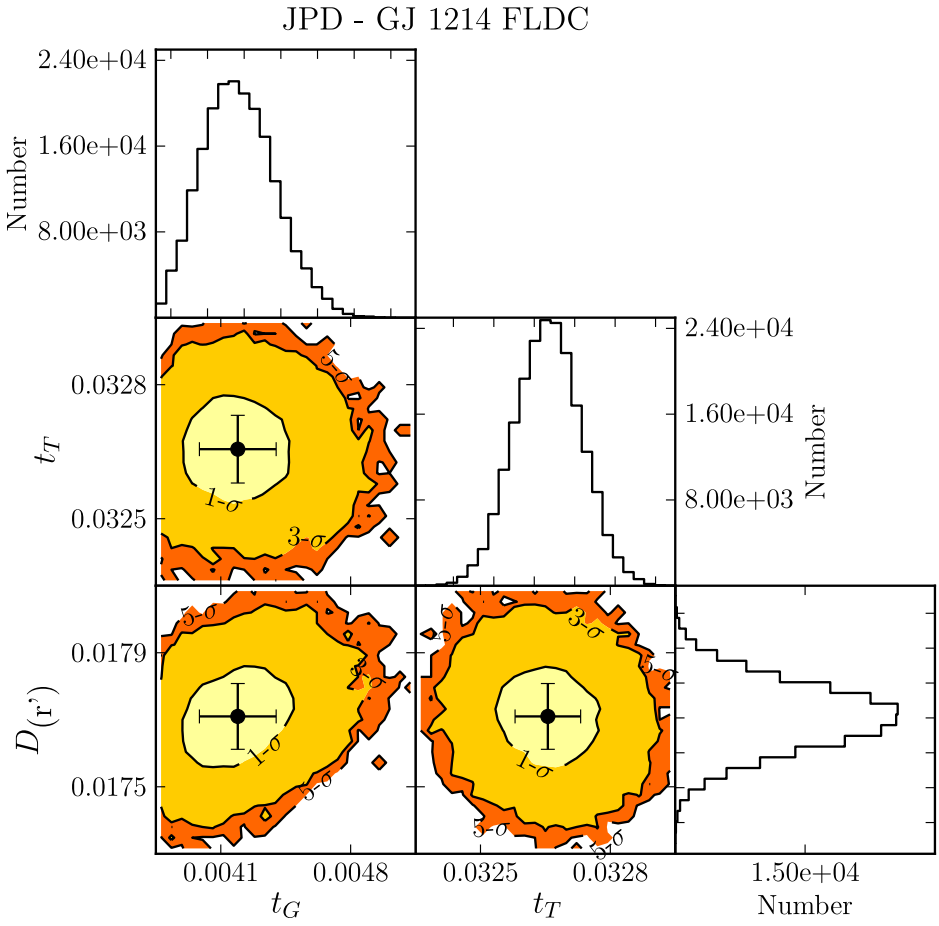

Figure 5.2: Plots of the Joint Probability Distributions (JPD) of parameters from the Fixed LDC chains. These demonstrate that the parameters chosen for $\boldsymbol{\theta}_{\text{Multi-Filter}}$ are generally uncorrelated. Table 5.3 gives units.

There are two features of stellar activity that can be easily detected in APOSTLE data: (i) Flares and (ii) spot-crossing events. Flares are short–term events which are believed to be caused by the sudden release of energy from the reconnection of magnetic field lines above an active surface region. Spot-crossings on the other hand can be detected during a transit by rising or declining lightcurves for cool or hot spots

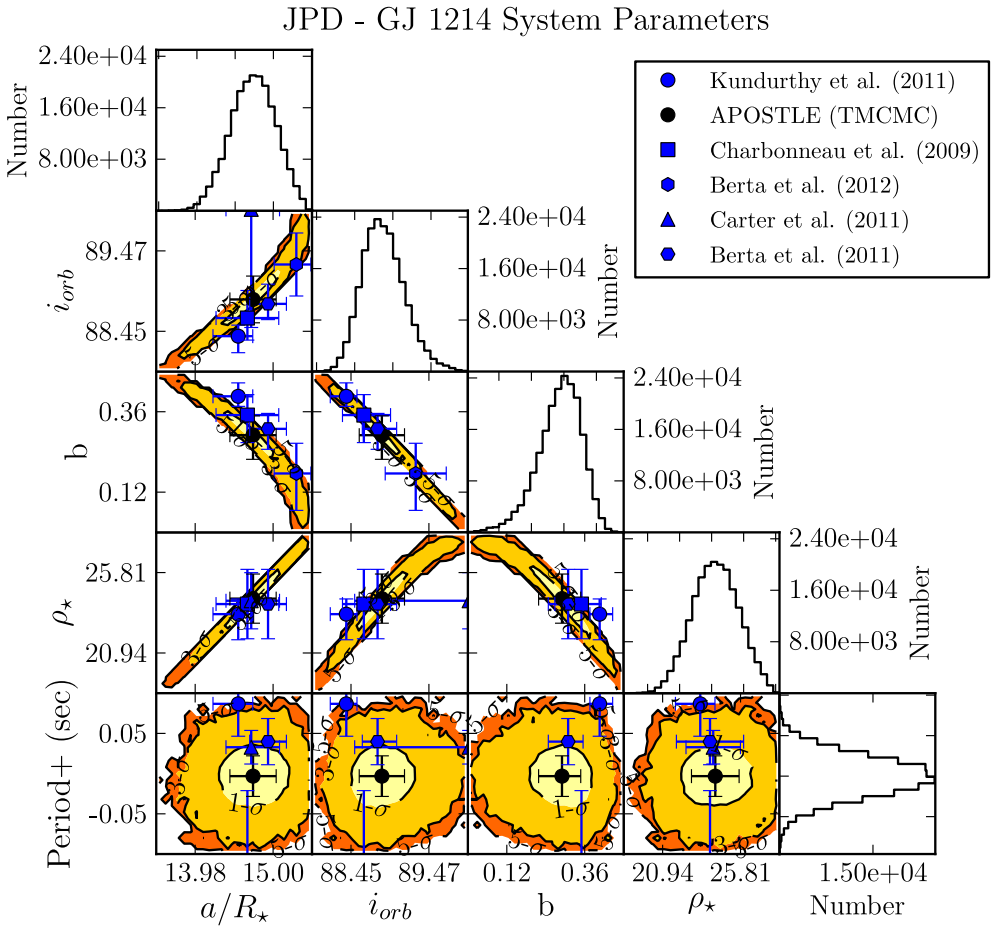

Figure 5.3: Plots of the Joint Probability Distributions (JPD) of derived system parameters from the Fixed LDC chains. Parameter estimates available in the literature are overplotted. Table 5.3 gives units.

respectively. These changes in the flux are seen during the eclipse portion of transit lightcurves as a result of the planet obscuring an active surface region with respect to the line-of-sight of the observer. We believe that our r'–band observations show evidence for a low-energy stellar flare on GJ 1214 and possible eclipses of cool spots on the stellar surface by the planet.

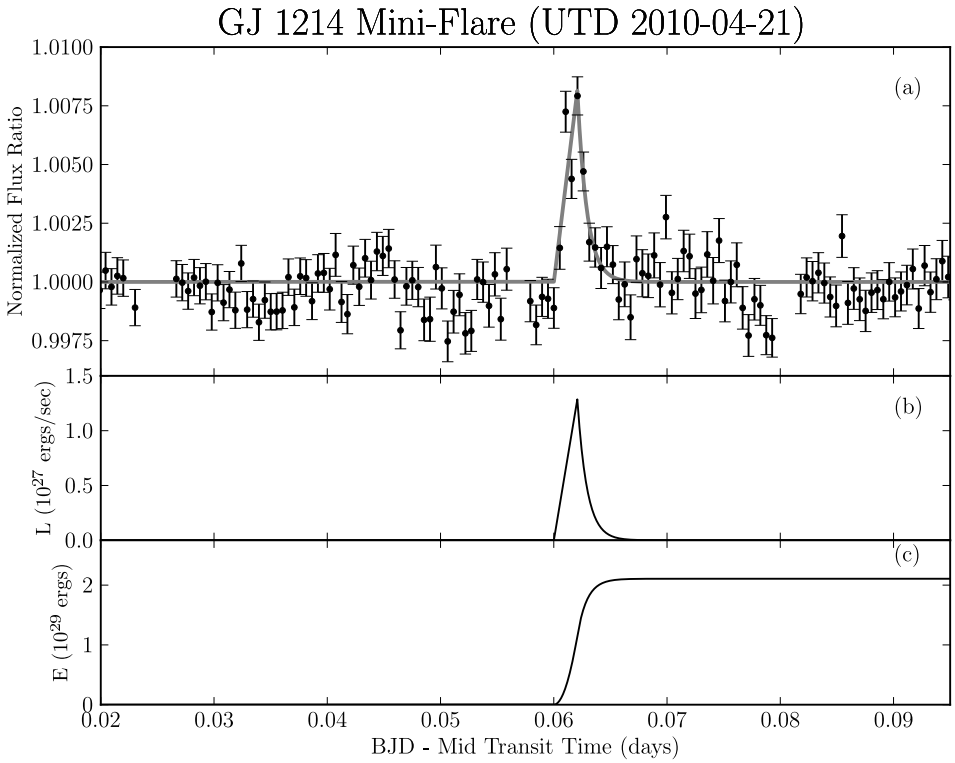

Figure 5.4: (a) Shows the flare event observed on UTD 2010-04-21. The gray line is the best-fit FRED model. The data points of the lightcurves have been normalized by the best-fit transit model. Even though only the points after mid-transit are shown, the fit was made using all lightcurve points. Panel (b) shows the r'–band luminosity as a function of time and panel (c) shows the total energy output by the flare above the quiescent r'–band level as a function of time.

The sharp rising and falling trend seen in the out-of-eclipse lightcurve on UTD 2010-04-21 (Figure 5.1) is similar to the fast-rise exponential decay (FRED) shape commonly associated with stellar flares (Hawley & Pettersen, 1991). Panel (a) in Figure 5.4 shows this event in greater detail. We built a lightcurve model with two components: 1) a linear rise phase and 2) an exponential decay phase. We fit for the start time, peak time, peak flux and the e-folding time of the exponential phase. The

model is roughly described by,

$$F(t) = \begin{cases} 1 & , t < T_{\rm S} \\ \dfrac{F_{\rm P}-1}{T_{\rm P}-T_{\rm S}}(t-T_{\rm S})+1 & , T_{\rm S} <= t < T_{\rm P} \\ (F_{\rm P}-1)\exp\left(-\dfrac{(t-T_{\rm P})}{T_{\rm decay}}\right)+1 & , t > T_{\rm P} \end{cases} \quad (5.1)$$

where t is the time coordinate, F is the lightcurve, $T_{\rm S}$ is the time when the fast-rise begins, $T_{\rm P}$ is the time when the flare peaks, $T_{\rm decay}$ is the e-folding time of the exponential part, and $F_{\rm P}$ is the peak flare flux. The best-fit lightcurve derived using `TMCMC` is shown as the solid gray line in Figure 5.4 (a). The $\Delta\chi^2$ for this flare model compared to a straight line fit to the data is 217.5. This result can be considered significant if it satisfies the Bayesian information criterion of $\Delta\chi^2 > N_{\rm free}\log(N_{\rm data})$, where $N_{\rm free}$ is the number of free parameters in the model and $N_{\rm data}$ the number of data points. Given 4 free parameters in the flare model $N_{\rm free}\log(N_{\rm data})$ =23.02, which makes this result significant. The r'–band flux of the star rose to a peak 0.8% above the quiescent level and decayed over ∼75 sec (e-folding time). Since we lacked flux-calibrated photometry, we used synthetic stellar spectra (Hauschildt et al., 1999) to estimate the energy output by this event. We determined the r'–band flux by integrating the synthetic spectra of a star with T_{eff} = 2949 K and $\log g = 4.94$ (from Kundurthy et al., 2011) over the spectral response of the r'–band (Ivezić et al., 2007; Maíz Apellániz, 2006). Using a stellar radius of $0.21 R_{\odot}$, we computed the quiescent luminosity in the r'–band to be $\sim 1.6\times10^{29}$ ergs/sec. Panel (b) in Figure 5.4 shows the flare model in luminosity units above the quiescent level for GJ 1214. Following the method described in Hawley et al. (2003) and Kowalski et al. (2010) we integrated under the flare lightcurve and estimated the total energy output by the flare in the r'–band to be $\sim 2.1\times10^{29}$ ergs (see Figure 5.4(c)). The time it would take for the non-flaring star to emit this amount of energy (referred to as the *equivalent duration* in the M-dwarf flare community) is 1.33 seconds. Compared to typical M-dwarf flares, this event is short-lived and of low energy. In fact, such events are likely to be drowned out

by noise for most flare monitoring campaigns as milli-mag precision is not commonly attained when looking at the most active stars. That being said, this event would be easily detected at shorter wavelengths where the flare energies peak, and where most flare observations are made. Hawley et al. (2003) reported flare energies between 8–58 $\times 10^{30}$ ergs from Johnson R-filter observations of the active star AD Leonis. The activity observed on GJ 1214 is at least 2 orders of magnitude lower in energy than some lower energy flares observed on AD Leo (an M3–M4 star). AD Leo has been identified as a member of the young galactic disk population (Montes et al., 2001). West et al. (2008) have established that stellar activity decreases with age. Even though the age for GJ 1214 has not been measured there is no indication that it is young like AD Leo, and hence the differences in the activity levels may also indicate different ages for these two stars.

During the transits on UTD 2010-06-06 (T_2), 2011-05-26 (T_4) and 2011-06-25 (T_5) we observed slight brightenings in the lightcurves during the eclipse (see open circles in Figure 5.1). Figure 5.5 shows these events in greater detail. The flare model described above provided poor fits to this type of signal; the shapes are somewhat flat-topped unlike the sharp-peaked FRED flares. The symmetry in the rise and drop, and the fact that these occurred during the transit makes it likely that we observed spot-crossing events (see Figure 3.2 in Ch. 3). We modeled the spot-crossing signal based on the analytic expressions in Mandel & Agol (2002) for the area of intersection between two circles, assuming the spot was of roughly circular shape. We did not account for the deformation of the spot due to the curvature of the star, and we assumed a zero spot-planet impact parameter. We fit for the spot-crossing duration ($t_{T,sp}$), signal height and central crossing time. The signal height is proportional to the square of the radius ratio of the spot to the planet (R_{sp}^2/R_p^2) and also depends on the brightness contrast between the spot and the star (Silva-Valio, 2003). Spots on the Sun are cooler than the surface by roughly 1000K, and can be several Earth-radii in size. It has been empirically estimated that the surface-spot temperature

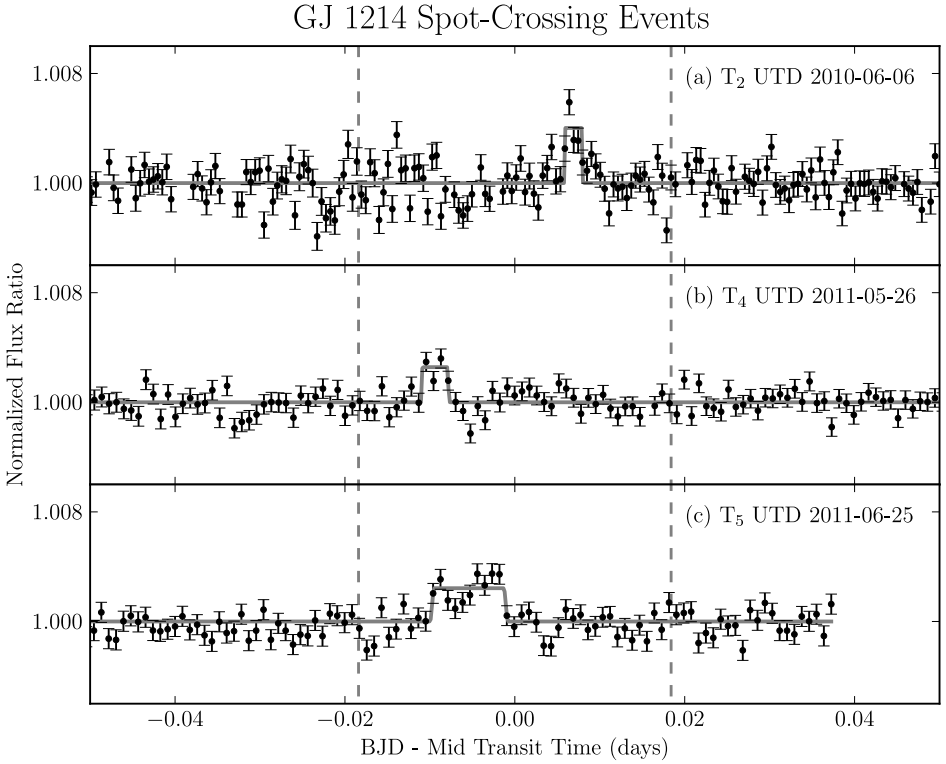

Figure 5.5: Possible spot-crossing events from 3 different transits of GJ 1214b on UTD 2010-06-06, UTD 2011-05-26 and UTD 2011-06-25. The transit signal was removed by normalizing the lightcurve with the best-fit transit model. The dashed vertical lines approximately mark the start (t_I) and end of the transit (t_{IV}). The gray line shows a fit using a simplified spot model.

difference falls at late spectral types. From data in the literature (Berdyugina, 2005) empirically shows that $\Delta T_{\text{star-to-spot}}$ ranges between 800-200K for early to late M-type dwarfs. We fixed the spot temperature (T_{sp} =2700K) to be 250K cooler than the stellar photosphere of GJ 1214 and computed a spot-to-star contrast of 50% (Silva-Valio, 2003). The fit using `TMCMC` yielded spot-sizes of 0.17 $R_\oplus$, 0.14 $R_\oplus$ and 0.14 $R_\oplus$ from the events seen on T_2, T_4 and T_5 respectively. We assumed the planetary radius for GJ 1214b to be 2.74 $R_\oplus$ (Kundurthy et al., 2011). The best-fit models shown in Figure 5.5 fit the data better than a flat-line, with relative goodness of fit, $\Delta\chi^2$ of 68.8,

45.9 and 109.8 for T_2, T_4 and T_5 respectively. Each of these $\Delta\chi^2$ satisfy the Bayesian information criterion by being greater than $N_{\rm free} \log(N_{\rm data})$ of 16.9, 15.6 and 15.4 for T_2, T_4 and T_5 respectively, given 3 free parameters in the spot model. The spot sizes estimated using this method must be interpreted as lower-limits to the true spot size, since (1) we do not account for grazing transits, (2) we ignore the latitudinal extent of the spots and deformation due to the curvature of the stellar surface, and (3) we fix the temperature differentials and hence avoid the size-contrast degeneracy for the spot.

The duration of spot-crossing ($t_{T,sp}$) can also be used to estimate the longitudinal extent of the cool region as $l_{sp} \propto 2R_{sp} \propto t_{T,sp}a/\text{Period}$ (Rabus et al., 2009). Given $t_{T,sp}$, the transit properties derived in this work and, the absolute stellar parameters from Kundurthy et al. (2011), we estimate the longitudinal extent of the spots to be $0.22\text{R}_\oplus$, $0.34\text{R}_\oplus$ and $0.93\text{R}_\oplus$ for T_2, T_4 and T_5 respectively. The two sets of spot size estimates are not consistent, and the differences can be understood by the fact that, in the first method we fix the spot-temperature and hence ignore a strong degeneracy between the spot size and the spot-to-star contrast. If we assume that the spot-sizes estimated from the second method (using spot-crossing duration) are accurate we can work backward and estimate the spot-temperatures using these sizes and the peak heights of the singals. Doing so, we find the spot temperatures to be 2920K, 2942K and 2948K, for T_2, T_4 and T_5 respectively. All three estimates place the spot temperatures too close the effective stellar temperature ($T_{\rm eff}$ = 2950K), leading to the conclusion that the method using the spot-crossing duration to define the spot-sizes is faulty due to its assumption of a single circular spot. The true situation for our observations could be that, we are likely observing clusters of small spots that span longitudinal regions on the star, between 0.2–0.9 Earth-radii in size. Resolving degeneracies between spot-size, spot-temperature and multiplicity would lead to a better understanding of the observational phenomenon of spot-crossing.

Recently Carter et al. (2011) reported similar anomalies in their lightcurves of

GJ 1214b, which they attributed to spots. Their analysis extended to quantifying the variations in transit depth over many epochs caused by spots. We refrain from such an analysis due to our limited dataset. Detailed calculations of spot-crossing have been made by long term monitoring of active stars with planets like CoRoT-2b, CoRoT-6b, CoRoT-7b and Kepler-17b (Lanza et al., 2009, 2010, 2011; Désert et al., 2011a).

Table 5.4: GJ 1214 Parameters for $\boldsymbol{\theta}_{\text{Multi-Depth}}$

Transit Depths	Value	Units	$R_p/R_\star$	Value	Units
$(D)_1$	0.0182±0.0002	-	$(R_p/R_\star)_1$	0.1180±0.0010	-
$(D)_2$	0.0179±0.0003	-	$(R_p/R_\star)_2$	0.1171±0.0012	-
$(D)_3$	0.0180±0.0003	-	$(R_p/R_\star)_3$	0.1174±0.0011	-
$(D)_4$	0.0169±0.0003	-	$(R_p/R_\star)_4$	0.1144±0.0011	-
$(D)_5$	0.0175±0.0003	-	$(R_p/R_\star)_5$	0.1159±0.0013	-
$(D)_6$	0.0175±0.0002	-	$(R_p/R_\star)_6$	0.1161±0.0011	-
Other MTQ Parameters					
Parameter	Value	Units	Parameter	Value	Units
t_G	0.0042±0.0002	days	t_T	0.0326±0.0001	days
v_1(r')	(0.8885)	-	v_2(r')	(0.3843)	-
Derived Parameters					
b	0.30±0.06	-	$a/R_\star$	14.71±0.29	-
i_{orb}	88.83±0.27	$^o(deg)$	$\nu/R_\star$	58.47±1.16	days^{-1}
$\rho_\star$	24.09±1.41	g/cc	-	-	-

Long-term variations in the transit depth could also indicate the presence of spots. For the situation when there are no spot-crossings during transit but cool spots exist, the observed transit depth will be deeper than when there are no spots on the surface due to the fact that spots lower the overall surface brightness of the

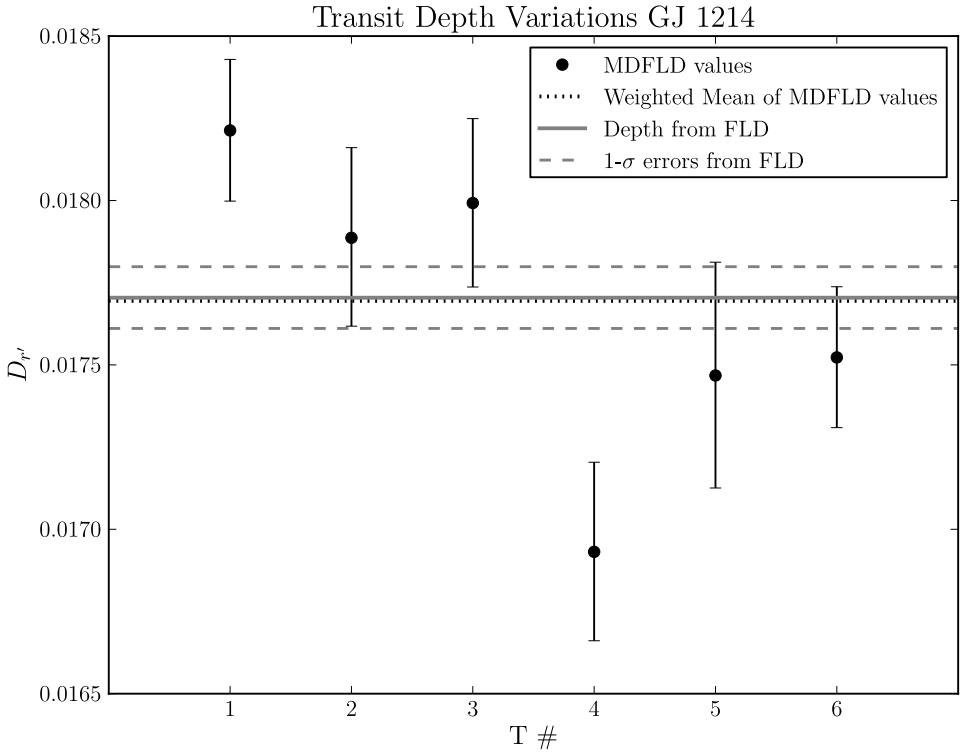

Figure 5.6: The transit depth D as a function of transit number for r'–band observations of GJ 1214b. The solid horizontal and dashed lines represent the best-fit value and errors respectively for D from the Fixed LDC `TMCMC` fit. The dotted line is the weighted mean of transit depth values from the Multi-Depth Fixed LDC chains.

stellar disk (see Figure 3.2). This effect would be easier to detect if APOSTLE had greater coverage of sequential transits. With the given data we can only hope to measure strong deviations in the transit-depth resulting from spots rotating in and out of view.

We list the parameter fits from the Multi-Depth chain in Table 5.4, and the corresponding plot of the depth variations are presented in Figure 5.6. Even though there are large differences between the individual estimates of transit depth and the joint fit to the depth (from Fixed LDC), most individual depth estimates are within

3σ of $D_{(r')}$ (using the uncertainties from the Multi-Depth fits). Only $(D)_4$ differs from the joint fit depth estimate by -3.3σ. This deviation can be explained by the fact that several of the in-eclipse points from T_4 were excluded due to the spot-crossing event hence lowering the accuracy of the transit depth measurement.

5.4 Transit Timing Analysis

GJ 1214 has been followed up by several teams since it is an easily observable Super-Earth for ground-based observers. The target star is also nearby and bright enough to be followed up easily with RV and other observations. We included transit times from the studies of Charbonneau et al. (2009); Sada et al. (2010); Carter et al. (2011); Kundurthy et al. (2011); Berta et al. (2011); Bean et al. (2011); Croll et al. (2011); Désert et al. (2011b); de Mooij et al. (2012) and Berta et al. (2012), in addition to the 6 times reported by this work. We exclude 1 point each from Carter et al. (2011) and Berta et al. (2012) where the timing precisions were worse than 2 minutes.

There are two versions of APOSTLE transit times presented, one from the Fixed LDC chain, and the other from the TAP fit to APOSTLE lightcurves. A linear ephemeris was fit to all the data using Eq. 3.3a, resulting in a best fit ephemeris of:

$$P = 1.580405350 \pm 0.000000088 \quad \text{days}$$
$$T0 = 2454964.9445104 \pm 0.0000257 \quad \text{BJD}$$

with a goodness of fit $\chi^2 = 370.7$ for 70 Degrees-of-freedom. The large reduced chi-squared $\chi^2/\nu = 5.3$ indicates that the linear fit is not robust. Even though the O-C points follow the zero variation line there is significant scatter between the various measurements. The largest deviation is $\sim$ 63 sec, with the overall scatter in the O-C values being $\sim$ 23 sec. These deviations could be a result of the diversity of fitting methods used, which are (1) unable to converge accurately on the same transit times, and (2) likely to underestimate timing errors. The O-C data do not show any non-

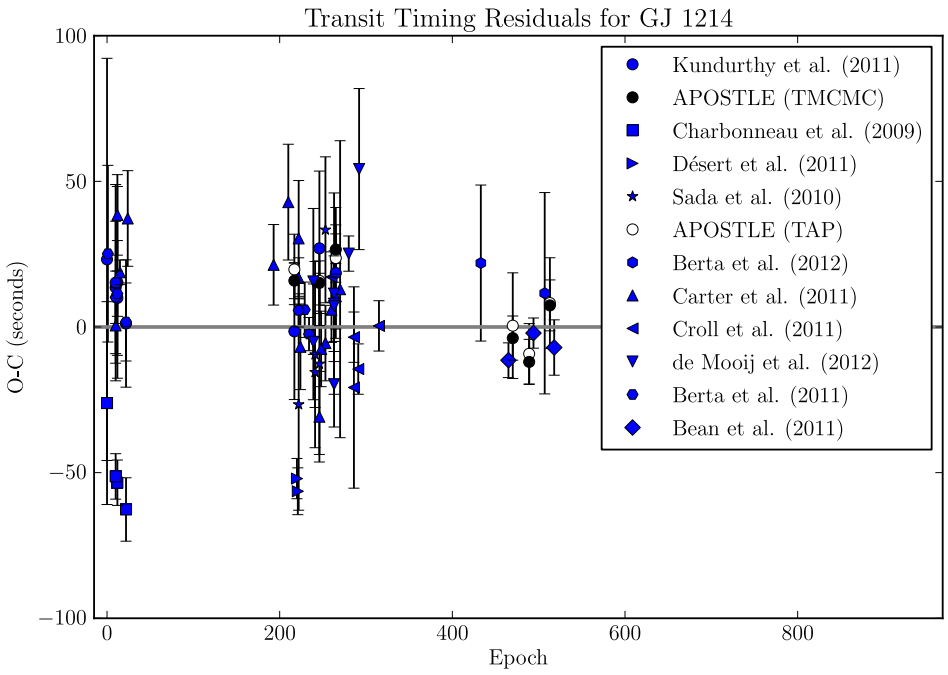

Figure 5.7: The Observed minus Computed Transit Times for GJ 1214b. Values from APOSTLE's `TMCMC` fit, TAP and the literature are plotted. The horizontal axis represents the transit Epoch. The zero-line ephemeris is described in § 5.4

linear or periodic tends, and hence we cannot claim planets as being the cause of the observed imprecise linear-fit to the ephemeris.

We also fit for a linear ephemeris to the APOSTLE data, using (1) the `TMCMC` and (2) the TAP values for the transit times (presented in Table 5.5). The difference between the periods derived for these subsets and the period derived from all available transit times is $\sim$ 80 milli-seconds, and hence insignificant. The reduced χ^2 of these fits are 1.4 and 0.4 for the `TMCMC` and TAP subsets respectively, showing that TAP gives more conservative errors for the transit times, owing to the red-noise analysis done during parameter estimation.

Table 5.5: APOSTLE Transit Times for GJ1214

Epoch	T0 (TMCMC) 2,400,000+ (BJD)	σ_{T0} (BJD)	T0 (TAP) 2,400,000+ (BJD)	σ_{T0} (BJD)
217	55307.8926553	0.0000715	55307.8927000	0.0001400
246	55353.7244015	0.0000876	55353.7244100	0.0001300
265	55383.7522361	0.0000979	55383.7522020	0.0000960
470	55707.7349807	0.0000878	55707.7350300	0.0002100
489	55737.7625878	0.0000895	55737.7626200	0.0001200
513	55775.6925407	0.0001012	55775.6925500	0.0001800

Chapter 6

XO-2b: Long Term Monitoring

XO-2b is a Hot-Jupiter on a 2.6 day orbit around an early type K dwarf (V = 11.2, Burke et al., 2007). The planet is known to have a mass of 0.555 $M_{\rm Jup}$ and a radius of 0.992 $R_{\rm Jup}$ (Southworth, 2010). The system is not known to have any other planet-mass objects. Transit timing measurements from the ground are consistent with a linear ephemeris (Fernandez et al., 2009; Sing et al., 2011), although both studies note that there are statistically significant deviations in the measurement of the orbital periods (see § 6.3). A search for additional eclipses using the EPOXI mission by Ballard et al. (2011) yielded no interesting information as the eclipse was not fully sampled. *Spitzer* observations of the secondary eclipse of XO-2b show IRAC 3.6, 4.5 and 5.8 μm fluxes which are consistent with the presence of a temperature inversion (Machalek et al., 2009). There have also been detections of optical absorbers such as potassium from narrow band optical transmission spectrophotometry (Sing et al., 2011). Models of irradiated gas giant atmospheres predict that warmer (strongly irradiated) planets will have temperature inversions caused by a variety of absorbers (Hubeny et al., 2003; Burrows et al., 2007; Fortney et al., 2008). The planetary atmosphere classification system developed by Fortney et al. (2008) places XO-2b in an transition zone between planets with (pM) and without (pL) thermal inversions. XO-2b is one of a handful of Hot-Jupiters in this regions. The host star is known to be a high metallicity ([Fe/H] = 0.45 ± 0.02), high proper motion star ($\mu_{\rm Tot}$ = 157 mas/yr) in a visual binary (Burke et al., 2007). Spectral activity indices show that XO-2 is fairly inactive compared to other stars of similar spectral type. This chapter describes APOSTLE observations, and the resulting analysis of XO-2b.

6.1 Ten Transits

XO-2b was an early APOSTLE target and was observed by members from the APOSTLE team over a timespan of 3 years from early 2008 till the spring of 2011. The summary of observations is given in Table 6.1. Early observations were made in the I–band with several data sets taken with short exposure times (see also § 2.1). The initial observations between 2008-2009 are credited to A. C. Becker, and the remaining observations, from 2010 onwards, were made by the author (P. Kundurthy).

XO-2 (TYC 3413-5-1) and its visual binary companion TYC 3413-210-1 (separated by $\sim$ 30") were the only stars that fit in *Agile*'s field of view. Both stars are of identical spectral type (K0V) and nearly identical brightnesses in the filters used by APOSTLE; with their Johnson R and I magnitudes at 10.8 and 10.5 respectively (Monet et al., 2003). Our uncalibrated differential photometry also showed good agreement in their brightnesses, with the out-of-eclipse, un-normalized flux ratios being different by only 4% and 3% in the I–band and r'–band respectively (Column 'Flux Norm.' in Table 6.1). The observations were made over a variety of observing conditions (Column 'Obs. Conditions' in Table 6.1). The tabulated transits are those for which we were able capture the whole transit or at least a partial transit. Partial transits are those where portions of the in-eclipse lightcurve were lost due to bad weather or instrumental failure. Several data points were lost for the nights of UTD 2008-09-22 (#4), 2009-02-06 (#5), 2009-03-12 (#6) and 2010-12-27 (#8). However we do include these nights since we did manage to obtain reasonable portions of the in-eclipse and out-of-eclipse data, which in turn make it possible to determine transit properties (albeit at a loss of accuracy and precision). The 10 transits of XO-2b are shown in Figure 6.1 in normalized flux ratios (with offsets for clarity). The plotted data result from the data reduction and model fitting processes described in Ch. 2.2 and Ch. 3 respectively.

Table 6.1: APOSTLE Observing Summary for XO2

T#	UTD	Obs. Cond.	Filter	Exp.	Bin	Phot. Ap.	RMS (ppm)	%Rej.	Flux Norm.	Error Scaling
(1)	(2)	(3)	(4)	(5)	(6)	(7)	(8)	(9)	(10)	(11)
1	2008-01-09	Clear	I	0.5	45	13	557	3%	0.9561	1.0000
2	2008-02-12	Clear	I	0.5	45	24	510	$< 1\%$	0.9561	1.0000
3	2008-03-04	Clear	I	0.5	45	15	411	$< 1\%$	0.9632	1.0000
4	2008-11-23	Poor Weather	I	10,25,45	45	27	939	1%	0.9756	1.0000
5	2009-02-07	Poor Weather	I	45	-	31	1085	11%	0.9721	1.0000
6	2009-03-13	Poor Weather	I	45	-	46	405	11%	0.9766	1.0000
7	2010-10-25	Clear	r'	45	-	35	553	2%	0.9676	1.0000
8	2010-12-27	Poor Weather	r'	45	-	43	775	5%	0.9643	1.0000
9	2011-01-30	Clear	r'	45	-	48	354	1%	0.9646	1.0000
10	2011-03-05	Clear	r'	45	-	43	693	$< 1\%$	0.9660	1.0000

(1) Transit Number, (2) Universal Time Date, (3) Observing Conditions, (4) Observing Filter, (5) Exposure Time (seconds)

(6) Bin size in seconds, (7) Optimal Aperture Radius (pixels), (8) Scatter in the residuals

(9) % frames rejected due to saturation or other effects, (10) Flux normalization between the target and comparison star

(11) The factor by which the photometric errors were scaled

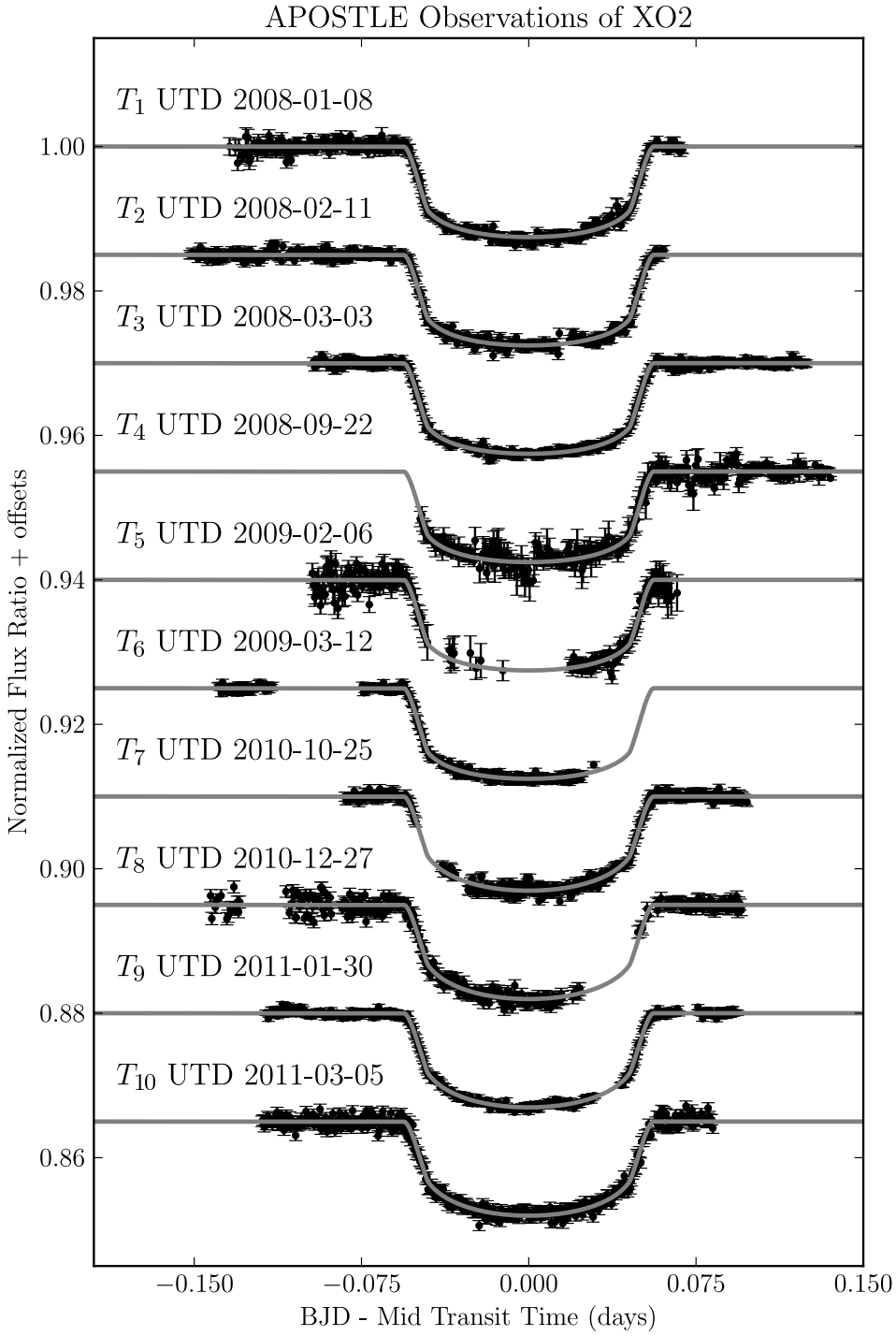

Figure 6.1: Six I–band and four r'–band lightcurves of XO-2b. The vertical axis is in normalized flux ratio units. The horizontal axis shows time from the mid-transit time in days, computed by subtracting the appropriate mid-transit time for each transit from the best-fit values in the Fixed LDC chain.

6.2 System Parameters

As described in Ch. 4 we ran 2 chains for the parameter set $\boldsymbol{\theta}_{\text{Multi-Filter}}$, and 1 for the $\boldsymbol{\theta}_{\text{Multi-Depth}}$. Table 6.2 lists information of these three chains, such as the version of the chain ('Chain') (see § 4.1 on p. 35) and the Model Vectors (see Ch. 3 p. 28) and the number of free parameters (N_{free}). All XO-2 b chains use t_G, t_T and include the transit times $T0$ for each of the 10 transits. The Fixed LDC and Multi-Depth Fixed LDC chains hold the 4 LDC fixed (2 each for the I–band and r'–band), while the Open LDC chain tries to fit for these. The Multi-Filter chains (Fixed LDC & Open LDC) have 2 transit depths (one for each filter) and the Multi-Depth (Multi-Depth Fixed LDC) chain fits each of the 10 XO-2 transits depths separately.

Table 6.2: `TMCMC` Chains for XO-2

Chain	Model Vector	N_{free}	Chain Length	Corr. Length	Eff Length	χ^2	DOF
FLDC	$\boldsymbol{\theta}_{\text{Multi-Filter}}$	14	1,900,001	100	19,000	3272.94	3312
OLDC	$\boldsymbol{\theta}_{\text{Multi-Filter}}$	18	1,900,001	4,949	383	3268.48	3308
MDFLDC	$\boldsymbol{\theta}_{\text{Multi-Depth}}$	22	1,900,001	588	3,231	3197.53	3304

Several of the remaining columns are from the auto-correlation analysis (see p. 39). The 'Chain Length' describes the number of points in the Markov Chain ensemble after cropping the initial burn-in and stabilization phases. The correlation and effective lengths are computed on these cropped chains (see p. 39). The numbers are extracted for all free parameters in the chain, and the parameter with the longest 'Eff. Length' (lowest statistical significance) is chosen to represent the level of robustness of the Markov chain result. Typically an MCMC result is considered significant if the effective length is > 1000, which for the XO-2b chains is true for both the Fixed Limb-Darkening Coefficient chains, and untrue for the Open LDC

chain. The final two columns list the goodness of fit (*i.e.* lowest χ^2 in the MCMC ensemble) and Degrees-of-freedom (DOF) from the respective chain. The resulting best-fit parameter estimates are listed in Table 6.3 for the Multi-Filter models, and in Table 6.4 for the Multi-Depth model.

Table 6.3: XO-2 Parameters for $\boldsymbol{\theta}_{\text{Multi-Filter}}$

Parameter	FLDC	OLDC	Unit
MTQ Parameters			
t_G	0.0107±0.0002	0.0108±0.0002	days
t_T	0.1008±0.0001	0.1004±0.0002	days
$D_{(\mathrm{I})}$	0.0126±0.0001	0.0126±0.0001	-
$D_{(\mathrm{r'})}$	0.0130±0.0001	0.0131±0.0001	-
v_1(I)	(0.5944)	0.5440±0.0313	-
v_1(r')	(0.6980)	$0.6411^{+0.0332}_{-0.0249}$	-
v_2(I)	(0.1452)	0.2806±0.0904	-
v_2(r')	(0.3524)	$0.4786^{+0.0734}_{-0.0992}$	-
Derived Parameters			
$(R_p/R_\star)_{(\mathrm{I})}$	0.1030±0.0003	0.1033±0.0004	-
$(R_p/R_\star)_{(\mathrm{r'})}$	0.1024±0.0003	0.1029±0.0004	-
b	$0.17^{+0.04}_{-0.02}$	0.21±0.03	-
$a/R_\star$	8.14±0.06	8.11±0.07	-
i_{orb}	88.79±0.15	$88.53^{+0.02}_{-0.10}$	$^o(deg)$
$\nu/R_\star$	19.55±0.15	19.48±0.17	days^{-1}
$\rho_\star$	1.49±0.03	1.48±0.04	g/cc
P (2.6159 days +)	-3467±22	-3466±22	milli-sec

These tables also list the derived system parameters (see § 3.1). Contour plots showing the joint probability distributions for the fit and derived parameters are

Table 6.4: XO-2 Parameters for $\boldsymbol{\theta}_{\text{Multi-Depth}}$

Transit Depths	Value	Units	$R_p/R_\star$	Value	Units
$(D)_1$	0.0134±0.0001	-	$(R_p/R_\star)_1$	0.1061±0.0005	-
$(D)_2$	0.0130±0.0002	-	$(R_p/R_\star)_2$	0.1047±0.0007	-
$(D)_3$	0.0123±0.0001	-	$(R_p/R_\star)_3$	0.1019±0.0005	-
$(D)_4$	0.0120±0.0001	-	$(R_p/R_\star)_4$	0.1009±0.0005	-
$(D)_5$	0.0121±0.0004	-	$(R_p/R_\star)_5$	0.1013±0.0015	-
$(D)_6$	0.0127±0.0002	-	$(R_p/R_\star)_6$	0.1035±0.0006	-
$(D)_7$	0.0133±0.0001	-	$(R_p/R_\star)_7$	0.1032±0.0004	-
$(D)_8$	0.0132±0.0002	-	$(R_p/R_\star)_8$	0.1030±0.0006	-
$(D)_9$	0.0131±0.0001	-	$(R_p/R_\star)_9$	0.1026±0.0003	-
$(D)_{10}$	0.0130±0.0001	-	$(R_p/R_\star)_{10}$	0.1024±0.0005	-
Other MTQ Parameters					
Parameter	Value	Units	Parameter	Value	Units
t_G	0.0108±0.0001	days	t_T	0.1008±0.0001	days
v_1(I)	(0.5944)	-	v_1(r')	(0.6980)	-
v_2(I)	(0.1452)	-	v_2(r')	(0.3524)	-
Derived Parameters					
b	0.24±0.02	-	$a/R_\star$	$8.02^{+0.03}_{-0.04}$	-
i_{orb}	88.29±0.15	$^o(deg)$	$\nu/R_\star$	$19.27^{+0.08}_{-0.10}$	days^{-1}
$\rho_\star$	1.43±0.02	g/cc	-	-	-

shown in Figures 6.2 and 6.3 respectively. All system parameters are in good agreement with previously published values in literature.

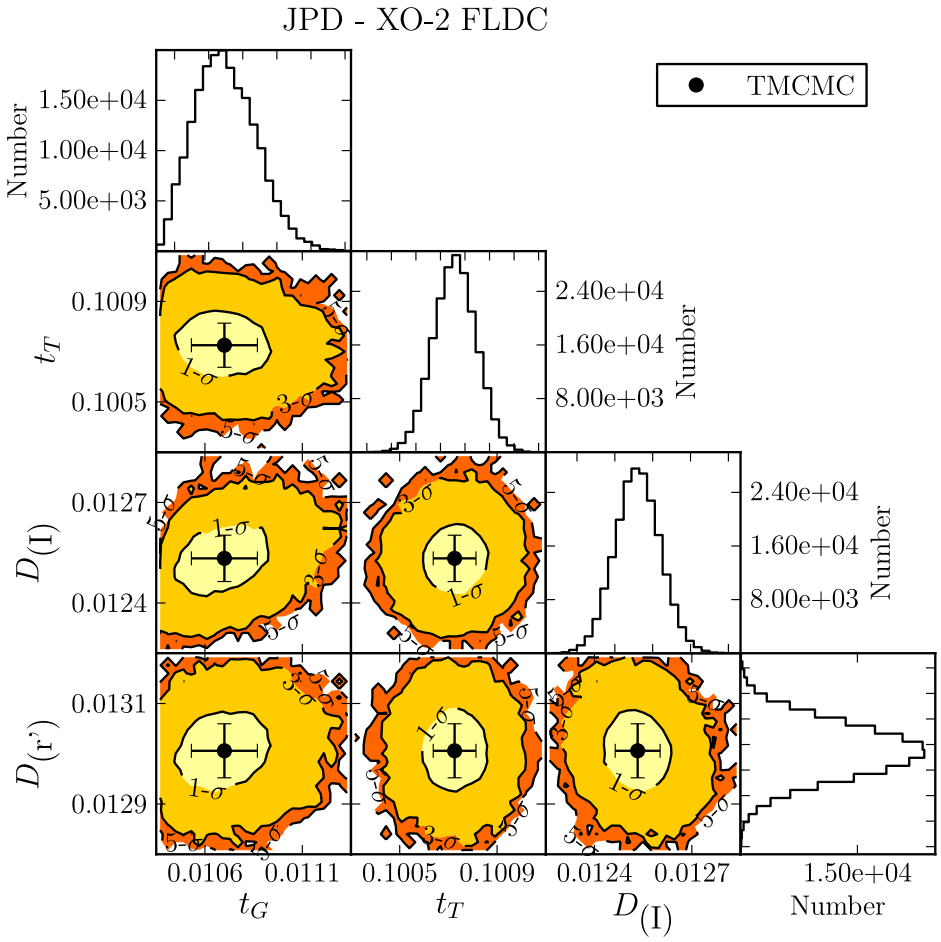

Figure 6.2: Plots of the Joint Probability Distributions (JPD) of parameters from the Fixed LDC chains, demonstrating that parameters chosen for $\boldsymbol{\theta}_{\text{Multi-Filter}}$ are generally uncorrelated. Table 6.3 gives units.

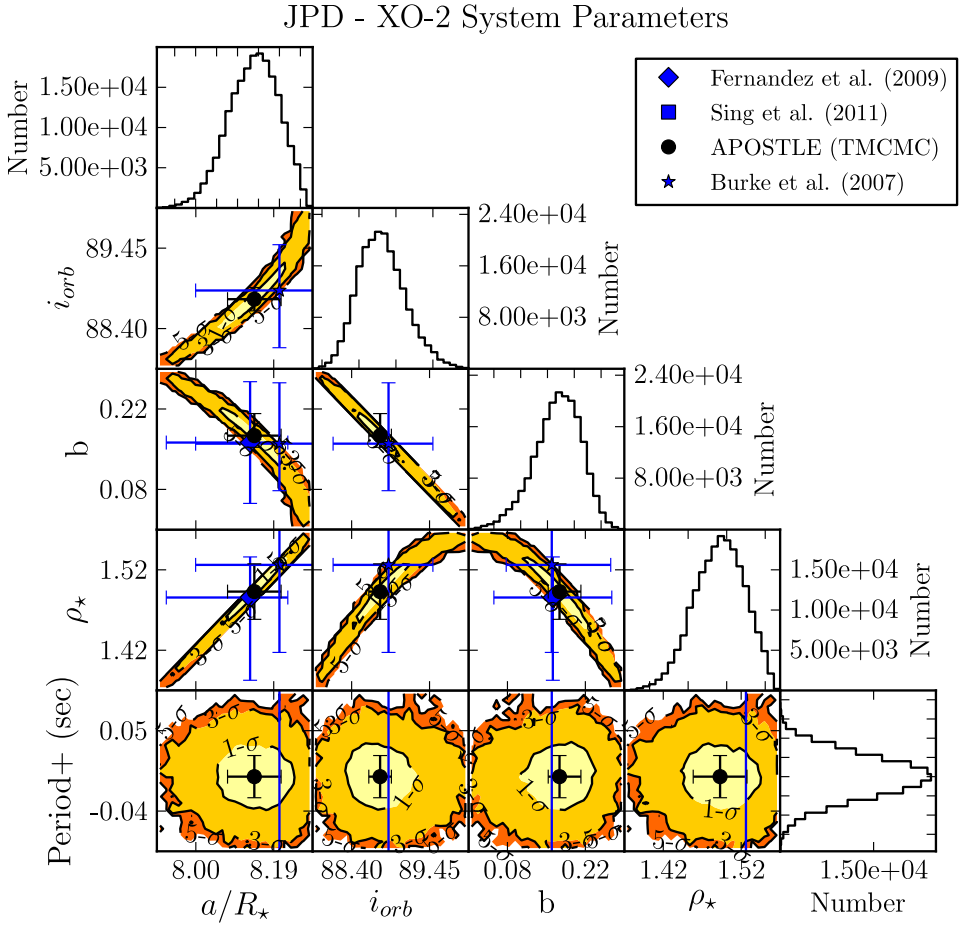

Figure 6.3: Plots of the Joint Probability Distributions (JPD) of derived system parameters from the Fixed LDC chains. Parameter estimates available in the literature are overplotted. Table 6.3 gives units.

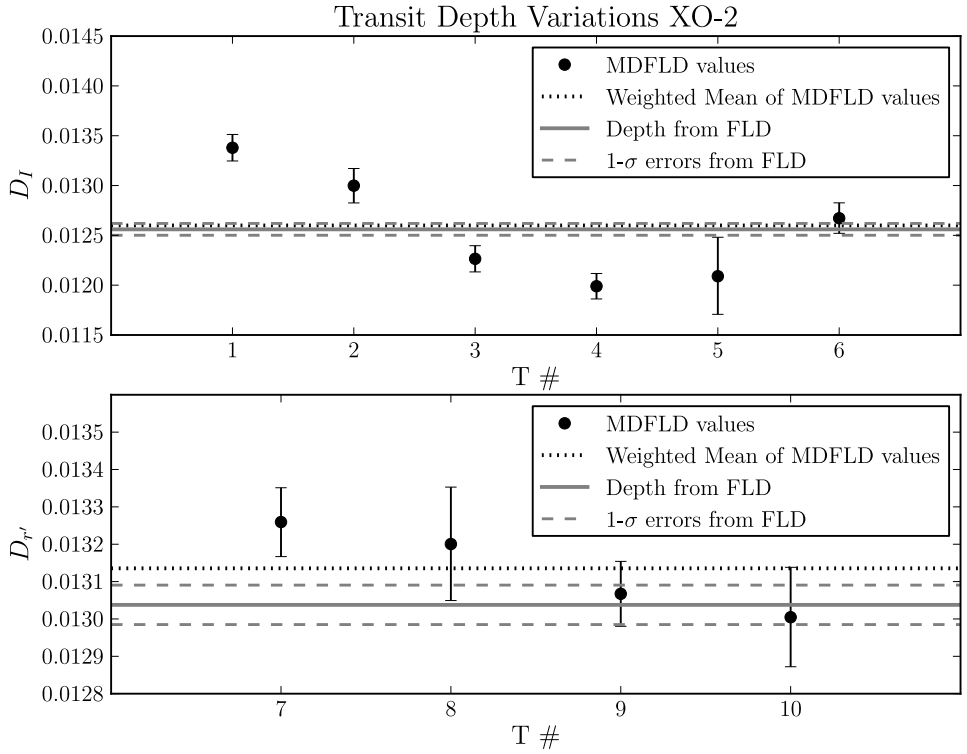

Figure 6.4: The transit depth D as a function of transit number for both I–band and r'–band observations of XO-2b. The solid horizontal and dashed lines represent the best-fit value and errors respectively for D from the Fixed LDC `TMCMC` fit. The dotted line is the weighted mean of transit depth values from the Multi-Depth Fixed LDC chains.

Figure 6.4 shows transit depth vs. transit epoch for the I–band (top panel) and r'–band (bottom panel). The overall variations in the I–band depth are $\sim 0.05\%$ compared to the 0.01% uncertainty in $D_{(I)}$ from the joint fit to depths in the Fixed LDC chain. Depth variations can be caused by spots (see Figure 3.2). Even though the variations we present are significant we refrain from claming the detection of depth variations since these deviations are likely due to the incomplete sampling of several transits rather than spots. Spots influence stellar brightness to a greater extent at shorter wavelengths, so the r'–band would be more conducive to showing depth variations caused by spot-modulation. The overall depth variation in the r'–band lightcurves is of the order 0.01% and is consistent with the errors on $D_{(r')}$ from the joint fits of the Fixed LDC chain (Table 6.3).

6.3 Transit Timing Analysis

Available transit times from the literature for XO-2 b include those of the discovery paper by Burke et al. (2007), and the follow-up observations by Fernandez et al. (2009) and Sing et al. (2011). We excluded the 11 transit times from Burke et al. (2007) as the reported timing errors were on the order of $\sim$ 3min, and are too large to provide meaningful constraints on the orbital ephemeris. We do include transit times from the other two studies, mentioned above.

There are two versions of APOSTLE transit times presented, one from the Fixed LDC chain, and the other from the TAP fit to APOSTLE lightcurves. Since TAP fits for rednoise components in the data, it has been shown that timing estimates are more accurate than when rednoise is included. A linear ephemeris was fit to all the data using Eq. 3.3a, resulting in a best fit ephemeris of:

$$P = 2.615860010 \pm 0.000000172 \quad \text{days}$$

$$T0 = 2454466.8852440 \pm 0.0000486 \quad \text{BJD}$$

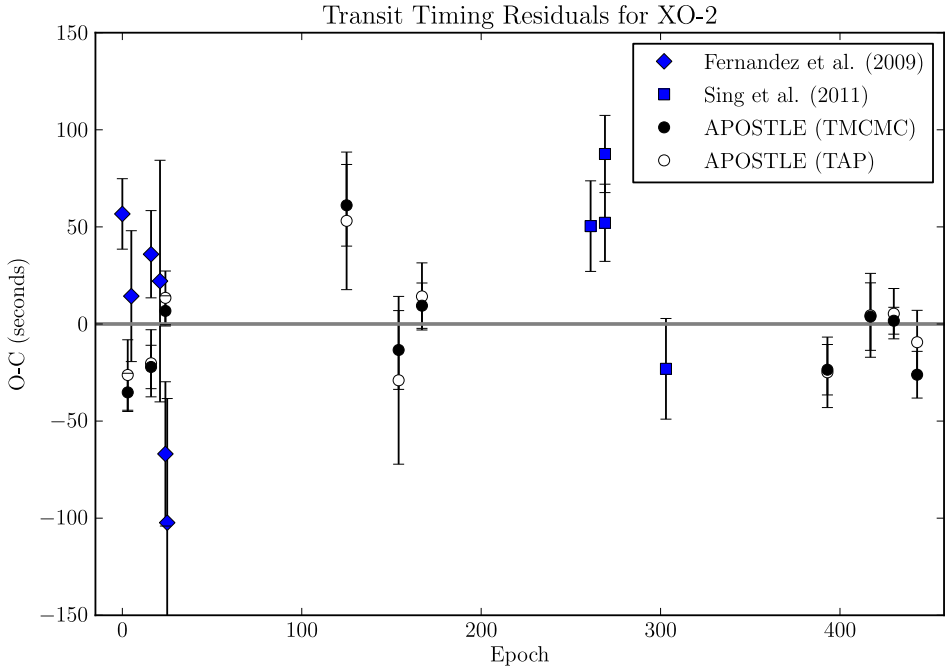

Figure 6.5: The Observed minus Computed Transit Times for XO-2b. Values from APOSTLE's `TMCMC` fit, TAP and the literature are plotted. The horizontal axis represents the transit Epoch. The zero-line ephemeris is described in § 6.3

with a goodness of fit $\chi^2 = 95.53$ for 28 Degrees-of-freedom. The reduced chi-squared $\chi^2/\nu = 3.41$ indicates that the linear fit is not robust, and is either due to the large timing deviations in the data or underestimated errors. For example, several of the Sing et al. (2011) data points lie far from the zero O-C line, with the largest deviation being $\sim$ 102sec. The scatter in the O-C values as a whole is $\sim$ 39sec which makes the 102sec deviation fall within the 3σ confidence interval of the collective data set. Though the linear ephemeris does not accurately fit the timing data, the level of variation is not significant enough for us to claim unseen planets as the cause.

In order to compare the ephemerides derived with and without rednoise analysis, we fit for a linear ephemeris to the APOSTLE transit times from `TMCMC` and TAP respectively (presented in Table 6.5). The difference between the periods derived

for these subsets and the period derived from all available transit times was < 7 milli-seconds. The reduced χ^2s were 3.96 and 1.26 for the `TMCMC` and TAP subsets respectively, confirming that TAP gives more conservative errors for the transit times thanks to the red-noise analysis.

Table 6.5: APOSTLE Transit Times for XO2

Epoch	T0 (TMCMC) 2,400,000+ (BJD)	σ_{T0} (BJD)	T0 (TAP) 2,400,000+ (BJD)	σ_{T0} (BJD)
3	54474.7324165	0.0001138	54474.7325200	0.0002100
16	54508.7387480	0.0001293	54508.7387700	0.0002000
24	54529.6659623	0.0000900	54529.6660400	0.0001600
125	54793.8684527	0.0002433	54793.8683600	0.0004100
154	54869.7275307	0.0002348	54869.7273500	0.0005000
167	54903.7339748	0.0001352	54903.7340300	0.0002000
393	55494.9179555	0.0001503	55494.9179400	0.0002100
417	55557.6989124	0.0002012	55557.6989200	0.0002500
430	55591.7050679	0.0000800	55591.7051100	0.0001500
443	55625.7109263	0.0001392	55625.7111200	0.0001900

Chapter 7

TrES-3b: A Hot Jupiter with a Near-Grazing Transit

TrES-3b is a very close-in Hot-Jupiter with one of the shortest orbital periods known (P=1.3 days O'Donovan et al., 2007). The planet orbits a G-type star (T_{eff} 5720K), and has a mass and radius of M_p =1.92 $M_{\rm Jup}$ and R_p =1.29 $R_{\rm Jup}$ respectively (O'Donovan et al., 2007). Due to its large impact parameter, TrES-3b's transit has more of a v-shape than the typical u-shape. However, the transit is not grazing and the ability of various observers to consistently measure the transit parameters seem to indicate that the planet's disk completely enters the stellar disk during the transit (O'Donovan et al., 2007; Sozzetti et al., 2009; Gibson et al., 2009). The v-shape would however make it challenging to make measurements of transit properties at bluer wavelengths where stellar limb-darkening further degrades the trapezoidal u-shape of the transit. The proximity of TrES-3b to the host star indicates that the planet is probably one of the warmest Hot-Jupiters, and the level of insolation received on the dayside should place this planet in the pM category of exoplanet atmosphere (Fortney et al., 2008). However, secondary eclipse observations from the ground and space have shown that the evidence for an inversion layer is not strong (de Mooij & Snellen, 2009; Fressin et al., 2010). TrES-3b's lack of an inversion layer is consistent with the idea that UV radiation from chromospherically active stars (like TrES-3b's parent star) systematically destroys absorbers in the upper planetary atmosphere, thereby preventing the formation of an inversion layer (Knutson et al., 2010).

The ultra close-in orbit of TrES-3b makes it a great target for follow-up transit

monitoring. It has been suggested that planets with very short periods are likely to be falling into their host stars. Some have looked for transit timing variations indicative of such orbital decay (for e.g. OGLE-TR-56b Adams et al., 2011). TrES-3b is similar to OGLE-TR-56b in many regards, including the orbital period ($<$ 1.5days), size ($\sim 1R_{\rm Jup}$) and impact parameter ($b > 0.8$). Though there has been no strong evidence for TTVs for OGLE-TR-56b, it is one object that warrants long term study (Adams et al., 2011). Transit monitoring of TrES-3b by other teams has so far confirmed its linear ephemeris (Sozzetti et al., 2009; Gibson et al., 2009). A search for additional transiting companions using the EPOXI mission has yielded no detections, since the likelihood of detecting a planetary sibling in a coplanar orbit with TrES-3b is lower for an outer planet given the inclination of the system (Ballard et al., 2011); inner planets are not expected since TrES-3b is already quite close to its parent star.

7.1 Eleven Transits

TrES-3b was observed by APOSTLE over a time span of 2 years between the summer of 2009 and the fall of 2011. The summary of its 11 r'–band observations is given in Table 7.1.

The parent star (GSC 03089-00929) is a G type star with a Johnson R magnitude of 12.2. The comparison star used was USNO-B1.0 1275-0332540 situated $\sim$ 90"away, with Johnson R of 12.9 (Monet et al., 2003). Our uncalibrated differentrial photometry shows that TrES-3 was the brighter of the two by a factor of $\sim$ 1.8 in the r'–band. There seems however, to be a greater variation in the uncalibrated flux between TrES-3 and its reference star, when compared to those of XO-2 and GJ 1214, with about 20% differece between the highest (#7 UTD 2011-03-24) and lowest (#3 UTD 2010-03-22) values. The observations were made over a variety of observing conditions (Column 'Obs. Conditions' in Table 7.1). The listed nights include both complete and partial transits (where data were lost due to poor weather or issues with the instrument). Some of these partial transits include UTD 2009-05-14 (#1),

2009-06-13 (#2) and 2010-06-02 (#10). Small portions of the in-eclipse data were lost for the transits on UTD 2010-03-22 (#3) and UTD 2011-04-27 (#8), and the night of UTD 2011-05-14 (#9) had exceptionally poor observing conditions (seeing > 2"). Even though these data will affect the fit, we keep them since they can be used to determine transit times, and in conjuction with more complete and higher precision data can be used to constrain transit parameters. The 11 transits of TrES-3b are shown in Figure 7.1 in normalized flux ratios (with offsets for clarity). The plotted data result from the data reduction and model fitting processes described in Ch. 2.2 and Ch. 3 respectively.

Table 7.1: APOSTLE Observing Summary for TRES3

T#	UTD	Obs. Cond.	Filter	Exp.	Bin	Phot. Ap.	RMS (ppm)	%Rej.	Flux Norm.	Error Scaling
(1)	(2)	(3)	(4)	(5)	(6)	(7)	(8)	(9)	(10)	(11)
1	2009-05-14	Clear	r'	45	-	30	777	2%	1.9179	0.5618
2	2009-06-13	Poor Weather	r'	45	-	22	610	13%	1.9083	0.5135
3	2010-03-22	Clear	r'	45	-	20	962	$< 1\%$	1.7788	0.7436
4	2010-05-16	Clear	r'	45	-	21	877	1%	1.8954	0.7769
5	2010-06-02	Poor Weather	r'	45	-	30	703	$< 1\%$	1.8670	0.2287
6	2010-10-12	Clear	r'	45	-	24	896	$< 1\%$	1.8832	0.7804
7	2011-03-24	Clear	r'	45	-	19	644	1%	1.9809	0.5644
8	2011-04-27	Poor Weather	r'	45	-	14	1022	1%	1.8932	0.9787
9	2011-05-14	Poor Seeing	r'	45	-	15	2960	$< 1\%$	1.8887	2.8965
10	2011-06-21	Clear	r'	45	-	26	1221	$< 1\%$	1.9227	0.9683
11	2011-08-24	Clear	r'	45	-	19	1240	7%	1.8016	0.7597

(1) Transit Number, (2) Universal Time Date, (3) Observing Conditions, (4) Observing Filter, (5) Exposure Time (seconds)

(6) Bin size in seconds, (7) Optimal Aperture Radius (pixels), (8) Scatter in the residuals

(9) % frames rejected due to saturation or other effects, (10) Flux normalization between the target and comparison star

(11) The factor by which the photometric errors were scaled

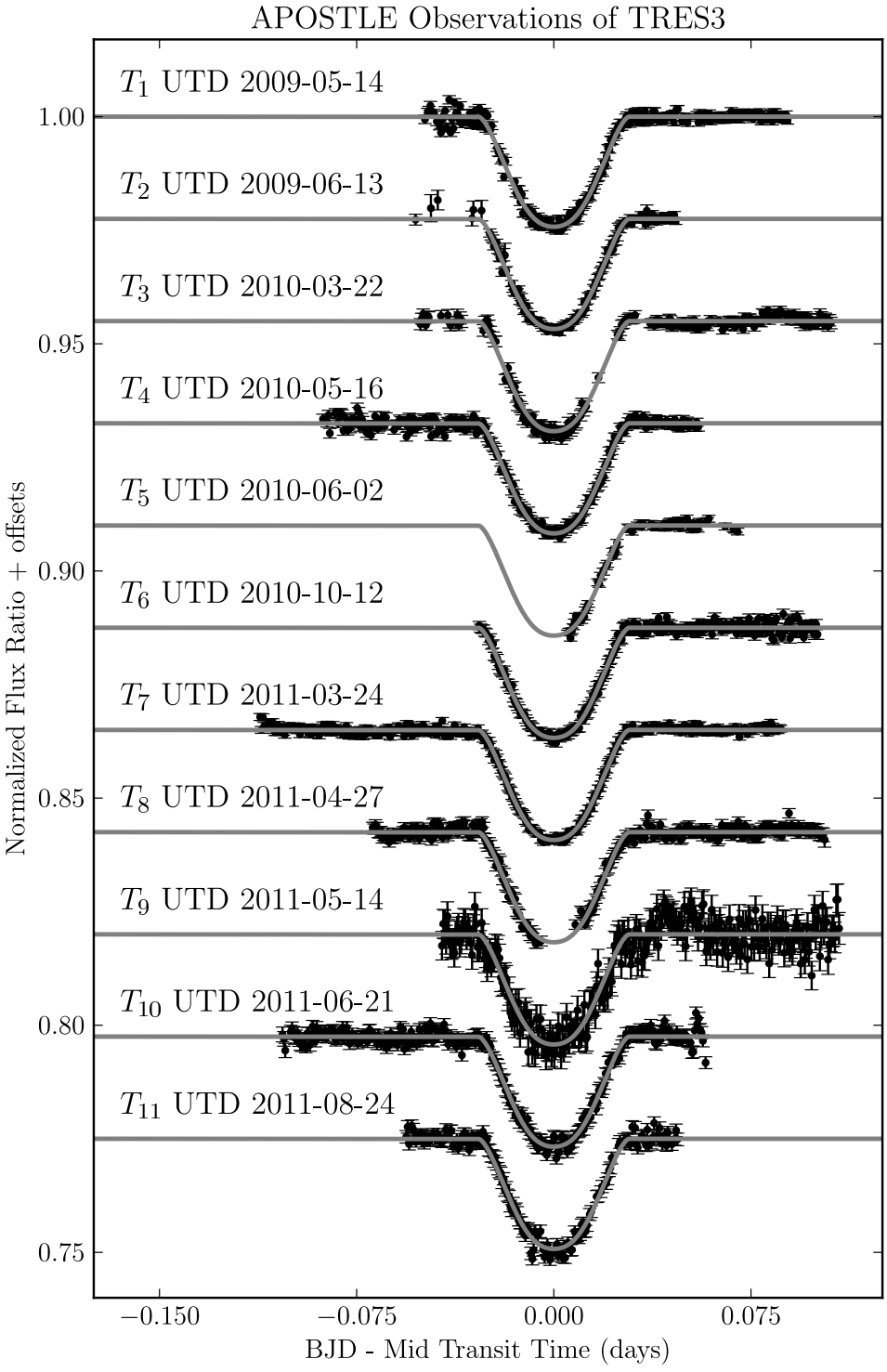

Figure 7.1: Eleven r'–band lightcurves of TrES-3b. The vertical axis is in normalized flux ratio units. The horizontal axis shows time from the mid-transit time in days, computed by subtracting the appropriate mid-transit time for each transit from the best-fit values in the Fixed LDC chain.

7.2 System Parameters

We ran the standard $\boldsymbol{\theta}_{\text{Multi-Filter}}$ and $\boldsymbol{\theta}_{\text{Multi-Depth}}$ chains as described in Ch. 4. Post processing statistics and other data for these chains are listed in Table 7.2. See Ch. 4 § 4.1 on p. 35 and Ch. 3 (p. 28) for the definitions of the 'Model Vectors' and `TMCMC` setup. All TrES-3b chains use t_G, t_T and include the transit times $T0$ for the 11 transits. Since all TrES-3b observations were taken in the r'–band, the Fixed LDC and Multi-Depth Fixed LDC chains fit for 2 LDC for the r'–band. The Multi-Depth chain was setup similarly, but with 11 free parameters for the transit depths.

Table 7.2: `TMCMC` Chains for TrES-3

Chain	Model Vector	N_{free}	Chain Length	Corr. Length	Eff Length	χ^2	DOF
FLDC	$\boldsymbol{\theta}_{\text{Multi-Filter}}$	14	1,900,001	318	5,974	2503.67	2575
OLDC	$\boldsymbol{\theta}_{\text{Multi-Filter}}$	16	1,900,001	4,996	380	2519.14	2573
MDFLDC	$\boldsymbol{\theta}_{\text{Multi-Depth}}$	24	1,900,001	2,866	662	2692.94	2565

The statistics from the auto-correlation analysis are listed under 'Chain Length', 'Corr. Length' and 'Eff. Length' (see p. 39). All chains were run for approximately 2 Million steps, but about 100,000 of the initial steps were removed to account for "burn-in" and selection rate stabilization. The TrES-3b chains all have quite low effective lengths indicating poor Markov chain statistics. Only the Fixed LDC, $\boldsymbol{\theta}_{\text{Multi-Filter}}$ model satisfies the condition of a well sampled posterior distribution (effective length is > 1000). The final two columns list the goodness of fit (*i.e.* lowest χ^2 in the MCMC ensemble) and Degrees-of-freedom (DOF) from the respective chain. The resulting best-fit parameter estimates are listed in Table 7.3 for the Multi-Filter models, and in Table 7.4 for the Multi-Depth models.

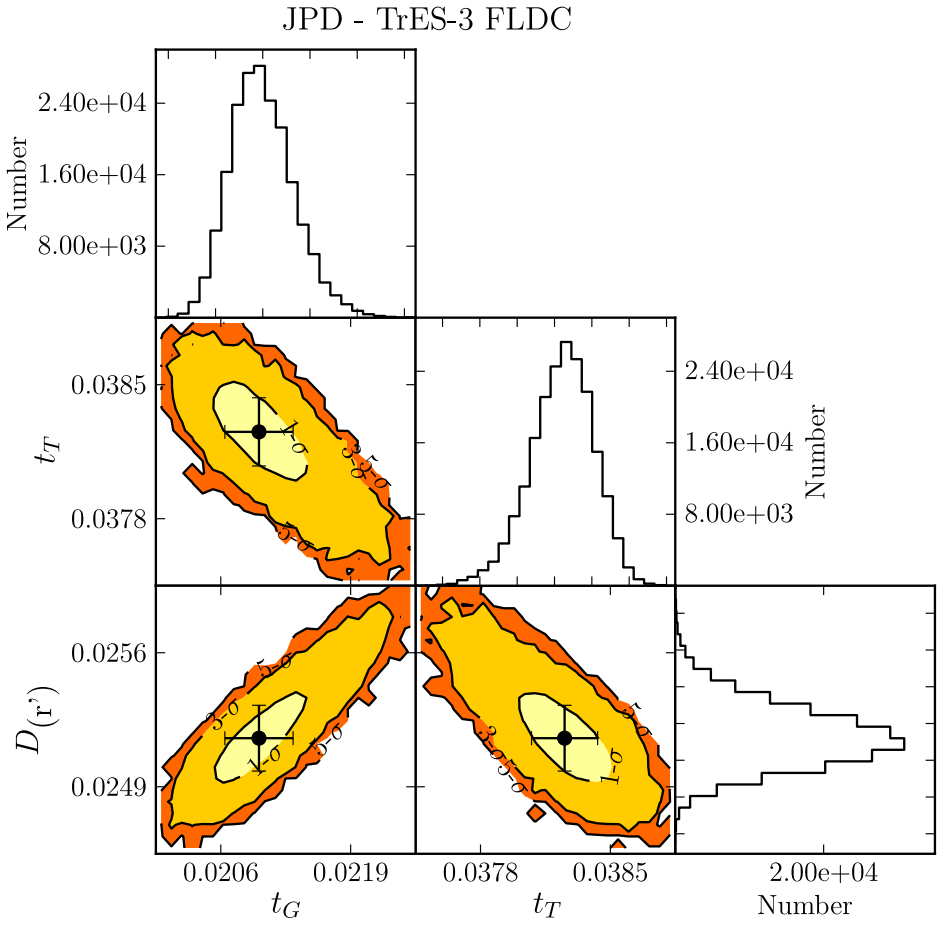

Figure 7.2: Plots of the Joint Probability Distributions (JPD) of parameters from the Fixed LDC chains, showing that due to the system's near-grazing transit the parameters chosen in $\boldsymbol{\theta}_{\text{Multi-Filter}}$ show correlations, unlike the cases for other systems discussed in this work. Table 7.3 gives units.

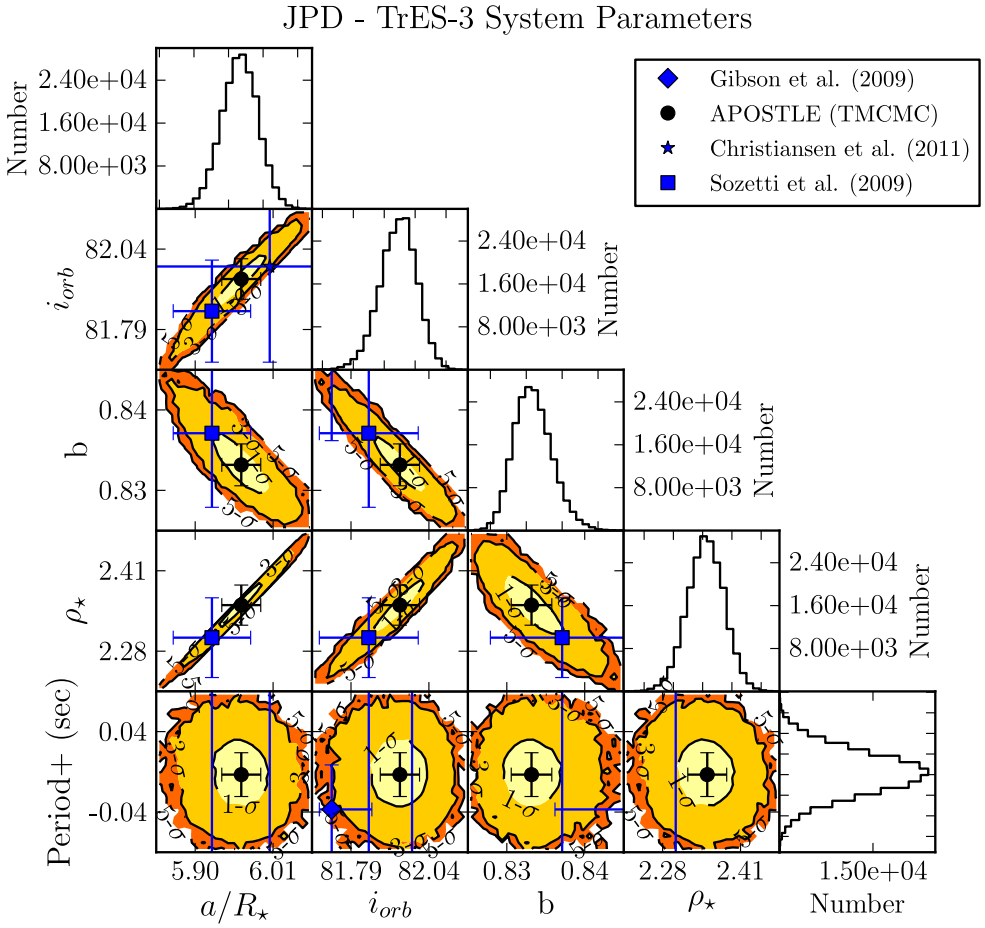

Figure 7.3: Plots of the Joint Probability Distributions (JPD) of derived system parameters from the Fixed LDC chains. Parameter estimates available in the literature are overplotted. Table 7.3 gives units.

Table 7.3: TrES-3 Parameters for $\boldsymbol{\theta}_{\text{Multi-Filter}}$

Parameter	FLDC	OLDC	Unit
MTQ Parameters			
t_G	0.0210±0.0004	$0.0212^{+0.0007}_{-0.0006}$	days
t_T	0.0383±0.0002	0.0385±0.0010	days
$D_{(\text{r'})}$	0.0251±0.0002	0.0255±0.0003	-
v_1(r')	(0.6767)	0.7371±0.1279	-
v_2(r')	(0.3008)	-0.1782±0.4955	-
Derived Parameters			
$(R_p/R_\star)_{(\text{r'})}$	0.1652±0.0009	0.1649±0.0015	-
b	0.84±0.00	0.84±0.01	-
$a/R_\star$	5.97±0.03	$5.91^{+0.04}_{-0.05}$	-
i_{orb}	81.95±0.06	$81.86^{+0.08}_{-0.26}$	$^o(deg)$
$\nu/R_\star$	28.71±0.14	$28.42^{+0.19}_{-0.26}$	days^{-1}
$\rho_\star$	2.36±0.03	$2.29^{+0.05}_{-0.06}$	g/cc
P (1.3062 days +)	-1141±21	-1109±22	milli-sec

Table 7.4: TrES-3 Parameters for $\boldsymbol{\theta}_{\text{Multi-Depth}}$

Transit Depths	Value	Units	$R_p/R_\star$	Value	Units
$(D)_1$	0.0249±0.0007	-	$(R_p/R_\star)_1$	0.1676±0.0025	-
$(D)_2$	0.0261±0.0009	-	$(R_p/R_\star)_2$	0.1711±0.0030	-
$(D)_3$	0.0276±0.0007	-	$(R_p/R_\star)_3$	0.1754±0.0024	-
$(D)_4$	0.0256±0.0005	-	$(R_p/R_\star)_4$	0.1696±0.0021	-
$(D)_5$	0.0237±0.0010	-	$(R_p/R_\star)_5$	0.1638±0.0034	-
$(D)_6$	0.0261±0.0006	-	$(R_p/R_\star)_6$	0.1710±0.0024	-
$(D)_7$	0.0259±0.0005	-	$(R_p/R_\star)_7$	0.1705±0.0021	-
$(D)_8$	0.0269±0.0006	-	$(R_p/R_\star)_8$	0.1734±0.0024	-
$(D)_9$	0.0274±0.0012	-	$(R_p/R_\star)_9$	0.1750±0.0038	-
$(D)_{10}$	0.0254±0.0005	-	$(R_p/R_\star)_{10}$	0.1690±0.0022	-
$(D)_{11}$	0.0277±0.0007	-	$(R_p/R_\star)_{11}$	0.1758±0.0025	-
Other MTQ Parameters					
Parameter	Value	Units	Parameter	Value	Units
t_G	0.0232±0.0007	days	t_T	0.0358±0.0004	days
v_1(r')	(0.6767)	-	v_2(r')	(0.3008)	-
Derived Parameters					
b	0.86±0.00	-	$a/R_\star$	5.96±0.03	-
i_{orb}	81.72±0.09	$^o(deg)$	$\nu/R_\star$	28.66±0.15	days^{-1}
$\rho_\star$	2.35±0.04	g/cc	-	-	-

These tables also list the derived system parameters (see Ch. 3.1). Contour plots showing the joint probability distributions for the fit and derived parameters are shown in Figures 7.2 and 7.3 respectively. System parameters agree somewhat with previously published values in literature, as seen by the over lap of the uncertainties in the JPD plot (Figure 7.3). It is interesting to note that there is a clear degeneracy in

the MTQ parameters as seen by the correlations in the posterior distributions of three parameters (D, t_G and t_T) shown in Figure 7.2. From the impact parameters ($b = 0.86$) we note that TrES-3b has a near-grazing transit. The correlation in the JPDs seen in Figure 7.2 can be understood from Equations 3.2b and 3.3b. Rearranging these give an expression where $\frac{t_G}{t_T} \propto \frac{D}{1-b^2}$. Carter et al. (2008) have shown that when $b \rightarrow 1$ (transit is close to grazing), the fraction t_G/t_T rises and the covariances between D, t_G and t_T rapidly deviate from zero. This degeneracy may be the primary reason why there is greater disagreement between the estimates of the system parameters for TrES-3b reported by various groups.

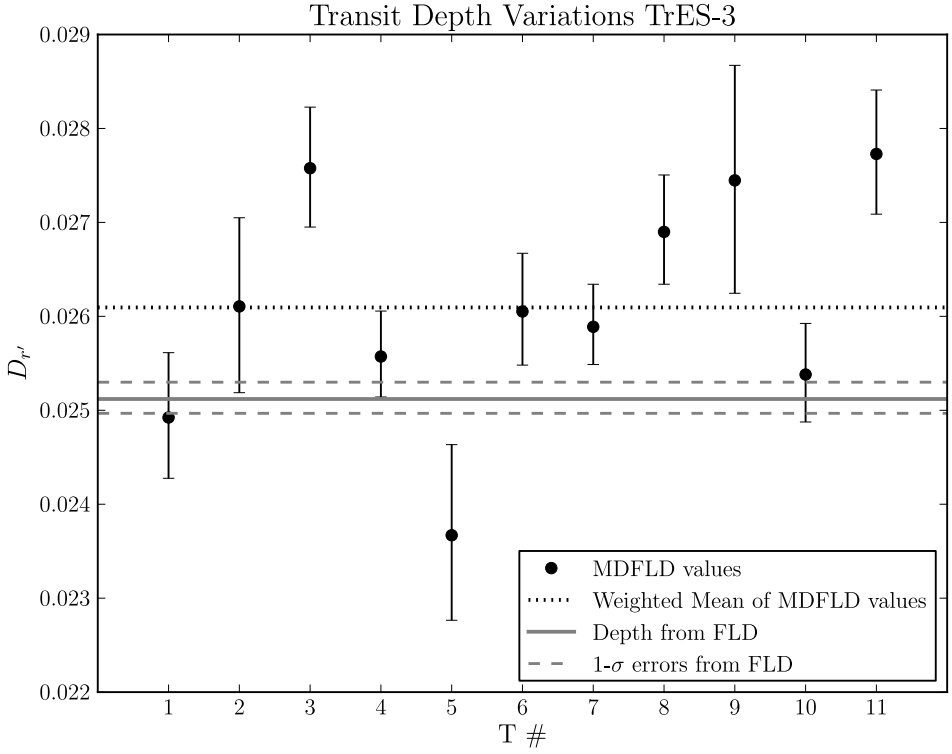

Figure 7.4: The transit depth D as a function of transit number for r'–band observations of TrES-3b. The solid horizontal and dashed lines represent the best-fit value and errors respectively for D from the Fixed LDC `TMCMC` fit. The dotted line is the weighted mean of transit depth values from the Multi-Depth Fixed LDC chains.

Figure 7.4 shows the transit depth vs. transit epoch for the r'–band observations. The overall variations in the r'–band depth are 0.1% compared to the 0.02% uncertainty in $D_{(r')}$ from the joint fit to depths in the Fixed LDC chain (Table 7.3). There are several facts about TrES-3 which would support the notion that the depth variability seen in Figure 7.4 is due to stellar activity. Firstly, the activity index reported for TrES-3 by Knutson et al. (2010) classifies it as an active star. Secondly, the r'–band is known to be affected by spots as the spot-to-star contrast ratios are enhanced at shorter wavelengths. Thirdly, the possibility that TrES-3 is variable is evidenced by the changing flux-ratio with its comparison star (Column 'Flux Norm.' in Table 7.1); though this fact could just as easily be explained by variability in the comparison. This being stated, one must also note that the TrES-3 dataset was plauged with several issues related to the incompleteness of lightcurves. At least 5 of the 11 lightcurves had data loss, which could have lead to inaccuracies in depth estimates. In summary, we can say that APOSTLE's TrES-3 data show several signs of variability which are consistent with prior knowledge of the activity of the host star. However, there have been no indications of spot-crossing events in the transit data (a sure sign of stellar activity); this could be due to a large impact parameter and the greater likelihood of starspots being equatorial.

7.3 Transit Timing Analysis

We gathered transit times published by Sozzetti et al. (2009), Gibson et al. (2009) and Christiansen et al. (2011), and pooled them alongside `TMCMC` and TAP measurements of 11 TrES-3 transit times. The O-C plot is shown in Figure 7.5. A linear ephemeris was fit to all the data using Eq. 3.3a, resulting in a best fit ephemeris of:

$$P = 1.306186483 \pm 0.000000070 \quad \text{days}$$

$$T0 = 2454185.9109932 \pm 0.0000502 \quad \text{BJD}$$

with a goodness of fit $\chi^2 = 204.1$ for 52 Degrees-of-freedom. The large reduced chi-squared $\chi^2/\nu = 3.92$ indicates that a linear fit does not precisely fit the transit times, and there are significant large timing deviations in the data. The largest timing deviation is ~ 127 sec from the Christiansen et al. (2011) data set. As previously noted, these deviations could either be due to underestimated timing errors or unaccounted timing systematics between different studies. The standard deviation of the O-C values is ~ 43 sec. The largest timing deviation is very close to being a 3-σ outlier. Several features of the O-C plot seem to indicate that these timing variation are likely due to inconsistencies between the various methods used to derive transit times. For example, Christiansen et al. (2011)'s times are consistently early when compared to the expected transit times (*i.e.* O-Cs are all negative); these measurements are all from the space-based EPOXI mission. A possible reason for this may be errors in time coordinate conversions between space-telescope time and BJD. Removing the Christiansen et al. (2011) transit times from the ephemeris fit results in a millisecond change in the fit period, but improves the goodness of fit slightly to $\chi^2/\nu = 3.5$, with the largest timing deviation and scatter being 78, and 35 seconds respectively. Given these discrepancies in the data we cannot claim any TTVs for TrES-3.

In order to compare the ephemerides derived with and without rednoise analysis, we fit for a linear ephemeris to the APOSTLE transit times from `TMCMC` and TAP respectively (presented in Table 7.5). The difference between the periods derived for these subsets and the period derived from all available transit times was < 12 milli-seconds. The reduced χ^2s were 7.99 and 1.33 for the `TMCMC` and TAP subsets respectively, confirming that TAP gives more conservative errors for the transit times thanks to the red-noise analysis.

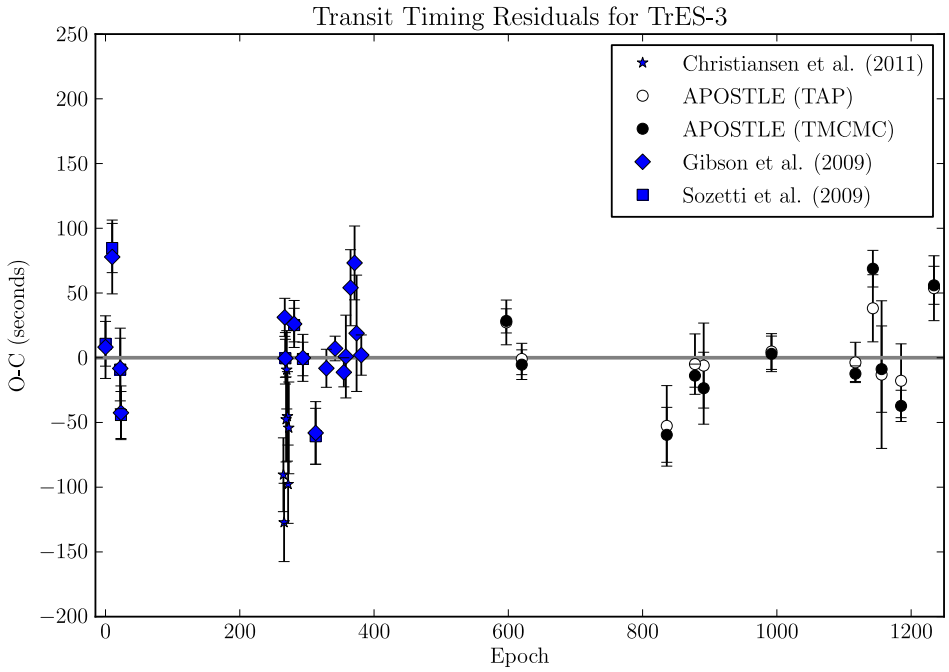

Figure 7.5: The Observed minus Computed Transit Times for TrES-3b. Values from APOSTLE's `TMCMC` fit, TAP and the literature are plotted. The horizontal axis represents the transit Epoch. The zero-line ephemeris is described in § 7.3

Table 7.5: APOSTLE Transit Times for TRES3

Epoch	T0 (TMCMC) 2,400,000+ (BJD)	σ_{T0} (BJD)	T0 (TAP) 2,400,000+ (BJD)	σ_{T0} (BJD)
597	54965.7046437	0.0001079	54965.7046300	0.0002000
620	54995.7465390	0.0001326	54995.7465900	0.0001400
836	55277.8821699	0.0002456	55277.8822500	0.0003600
878	55332.7425269	0.0001033	55332.7426300	0.0002700
891	55349.7228375	0.0003216	55349.7230400	0.0003800
992	55481.6479691	0.0001589	55481.6479900	0.0001600
1117	55644.9210892	0.0000699	55644.9211900	0.0001800
1143	55678.8828740	0.0001637	55678.8825200	0.0003000
1156	55695.8623990	0.0003861	55695.8623500	0.0006600
1185	55733.7414753	0.0001397	55733.7417000	0.0003300
1234	55797.7456860	0.0001699	55797.7456600	0.0002900

Chapter 8

Conclusions

I. Experimental Setup & Tracking Errors: APOSTLE has successfully produced a catalog of 36 transit lightcurves of previously known transiting systems over a period of 4 years between 2007 and 2011. Using the high-speed photometer *Agile* on the ARC 3.5m telescope at Apache Point, APOSTLE attained photometric precision on the order of ∼350 ppm. For the 3 targets discussed in this dissertation, GJ 1214b, XO-2b and TrES-3b's, photometric precisions ranged between 600–1400ppm, 350–1000ppm and 600–1200ppm respectively (excluding nights with poor seeing). The summary of observational results are presented in the Tables 5.1, 6.1 and 7.1, for GJ 1214b, XO-2b and TrES-3b respectively. The corresponding results for the other APOSTLE target WASP-2b will be published in an upcoming article (Becker et al., in prep).

We developed a customized processing pipeline, which carried out reductions for *Agile* and tracked various uncertainties through each step (Ch. 2, see § 2.2). We noted uncertainties from dark-subtraction, flat-fielding, non-linearity corrections and fringe corrections to generate error frames. These frames were later used along with the processed science frames for circular aperture photometry, from which the fluxes and errors are derived. Tracking errors in this manner provided slightly more conservative errors than those yielded by commonly used packages like PHOT. We also extracted several nuisance parameters which were used to remove long-term trends in the data resulting from differential extinction, centroid wandering, and fringing etc. In order to avoid making premature claims of interesting signals, we recommend the detailed

accounting of as many sources of error as possible when extracting transit photometry.

II. A Transit Model Suited for Bayesian Analysis: Following the prescription detailed in Carter et al. (2008) we fit for transit parameters such as the transit depth (D), limb-crossing duration (t_G), transit duration (t_T) and the transit times. These parameters have few mutual degeneracies and hence are suited for Bayesian inference techniques like Markov Chain Monte Carlo. The model (`MultiTransitQuick`) is described in Ch. 3. We also developed a Markov Chain Monte Carlo analyzer designed to use `MultiTransitQuick` to fit for the transit parameters using APOSTLE data (described in Ch. 4). The routine `TMCMC`, uses the Metropolis-Hasting algorithm with the adaptive jump-controller system described in Collier Cameron et al. (2007b). A major limitation in the use of `MultiTransitQuick` and `TMCMC` is the inability to accurately fit for red-noise in the data. We performed comparisons of `TMCMC` with the TAP (Gazak et al., 2011) transit model (which includes a red-noise analysis) and found that `TMCMC` underestimates the errors on certain system parameters.

III. GJ 1214b System Parameters & Stellar Activity: Our six r'–band observations of GJ 1214b yielded new and improved estimates of several system parameters. We do not find any significant disagreements in the system parameters when compared to previous transit studies of GJ 1214. Our r'–band transit depth, noted in Table 5.3 is consistent with findings of a flat transmission spectrum for GJ 1214b (Bean et al., 2011; Berta et al., 2012). Notably, our depth measurement is more precise, by a factor of 2, when compared to narrow-band spectro-photometry from the VLT[1] (see FORS Blue data Channel 1, Bean et al., 2011). Markov chains where the limb-darkening coefficients were set as free parameters failed to converge. Hence, we conclude that APOSTLE did not achieve the photometric precision required to

[1]Very Large Telescope

constrain limb-darkening coefficients for GJ 1214.

The detection of a low energy stellar flare on UTD 2010-04-21 and the possible transit of the planet over star-spots on three occasions (see Ch. 5, Figures 5.4 and 5.5) indicate that GJ 1214 is active. The r'–band flare energy indicates that this event was of lower energy than typical observed r'–band flares on active stars (like AD Leo, Hawley et al., 1996, 2003). We find a fast-rise exponential decay profile fits the flare signal quite well.

We also observed three anomalous increases in the normalized flux ratios during the transits on UTD 2010-06-06 (# 2), 2011-05-26 (# 4) and 2011-06-25 (# 5), indicative of spot-crossing events – where the planet occults star-spots on the surface of GJ 1214 during transit. We placed estimates on the minimum spot-sizes using two different techniques; (1) we assumed zero-impact spot-crossing, and fixed the spot-temperature to estimated temperatures of cool regions on M-dwarfs (Berdyugina, 2005), and fit for the spot-crossing duration, central time and the peak of the signal. (2) We used the fit to spot-crossing durations to compute the longitudinal extent of the cool regions. The size estimates were inconsistent and we conclude that degeneracies between spot-size, spot-temperature and spot multiplicity make it difficult to accurately describe the geometries of active regions from spot-crossing signals. It is also useful to note that the level of spot deformation due to the curvature of the stellar surface, and the latitudinal extent of spots also cannot be easily understood.

Spots and stellar rotation should result in long-term transit depth variations (Carter et al., 2011; Berta et al., 2011). However, analysis of depth-variations of APOSTLE data do not indicate a significant influence of spot-modulation on the transit depth.

IV. XO-2b System Parameters: From our analysis of 10 lightcurves of XO-2b, we were able to confirm and improve previous estimates of system parameters for the XO-2 system. We note interesting variations in the transit depth for our I–band

observations, but refrain from attributing spot-modulation as the cause for these variations (see Figure 6.4 in Ch. 6). Markov chains where limb-darkening coefficients were set as free parameters failed to converge. Hence, we conclude that APOSTLE did not achieve the photometric precision required to constrain limb-darkening coefficients for XO-2, in spite of the fact that we achieved sub-milli-magnitude precision on many of its lightcurves.

V. TrES-3b System Parameters: From our analysis of 11 lightcurves of TrES-3b, we were able to confirm and improve previous estimates of system parameters for the TrES-3 system. Due to the system's near grazing transit we note that several free parameters from `MultiTransitQuick` showed strong correlations in their Joint-Probabilities (see Figure 7.2). Such correlations are not suited for MCMC analysis, yet we were able produce Markov chain which converged and hence derive statistically significant measurements of system parameters and uncertainties (esp. the FLDC chain). Markov chains where limb-darkening coefficients were set as free parameters failed to converge. Hence, we conclude that APOSTLE did not achieve the photometric precision required to constrain limb-darkening coefficients for TrES-3.

VI. APOSTLE Transit Timing Variations: The transit timing precisions achieved by APOSTLE easily allow for the detection of TTV signals $>$ 1min. However, we were unable to detect significant timing variations for GJ 1214b, XO-2b and TrES-3b in our data. We find that fitting for transit parameters while accounting for red-noise, provided more conservative error estimates on transit times. The significance of timing deviations seen in the `TMCMC` analysis of APOSTLE data were lessened when the same dataset was analyzed with TAP (Carter & Winn, 2009; Gazak et al., 2011).

Transit times published in the literature are derived using different techniques for fitting transit parameters. We think, that a proper analysis of transit times would need a simultaneous analysis of transit lightcurves using a transit model which is, (1)

suited for Bayesian inference (*i.e.* with a fairly uncorrelated parameter set, Carter et al., 2008) and (2) a transit model which can adequately account for red-noise in the data (like TAP, Gazak et al., 2011). The catalog of transit times accumulated in the literature, and used in our cumulative study of transit times is not derived from such an analysis. It is likely that the deviation we detect are a result of this fact.

More than 200 transiting exoplanets have been characterized (as of July 2012, exoplanet.eu). APOSTLE surveyed only 4 systems from this set over four years, and 3 of these systems were Hot-Jupiters. Extrapolations from *Kepler* planetary candidate data seem to indicate that small planets may be ubiquitous (Borucki et al., 2011b). Interesting trends that have been noted are, (1) Hot-Jupiters tend be alone, *i.e.* lacking other transiting planet siblings (Latham et al., 2011; Steffen et al., 2012) and (2) members of multi-planet systems with short period planets (Period $<$ 10 days) are more likely to be Hot-Neptunes (Latham et al., 2011; Lissauer et al., 2011b). This trend seems to reveal the existence of different formation pathways among volatile-rich planets. Hence the lack of detections of multi-planet systems among the APOSTLE candidates is consistent with *Kepler*'s findings.

8.1 Ground-based Transit Observations & Follow-up

Over its mission life-span, the *Kepler* mission will provide a wealth of information from its time-series monitoring of over 150,000 stars. The nearby stellar population is likely to provide a similar treasure of knowledge once fully studied. Given that there are no major space-based projects in the works for such an endeavor, the onus falls on ground-based programs. Transit search programs, like the Wide Angle Search for Exoplanets (WASP, Kane et al., 2003; Street et al., 2003), HATNET (Bakos et al., 2009) and the XO Project (McCullough et al., 2005) are continuing to find exoplanets around the brightest nearby stars. Unlike the *Kepler* mission, whose targets span a small portion of the sky, the nearby stars are harder to monitor with a single instrument for obvious reasons. Even though we may never completely monitor the

whole night-sky and the nearby bright stars for transits, the existent target list for ground-based follow-up is numerous.

Several projects (similar to APOSTLE) have made follow-up transit observations for the purpose of deriving high precision measurements of system parameters and transit timing. The Rapid Imager to Search for Exoplanets (RISE) camera (Steele et al., 2008) has been used to follow-up several transiting systems. Observations using RISE of TrES-3b from the 2m Liverpool Telescope by Gibson et al. (2009) yielded photometric precisions between on the order of > 1000 ppm (comparable to APOSTLE). The RISE project has added an instrument to the 2.3m ARISTARCHOS telescope (RISE2) in La Palma (Boumis et al., 2010). The Asiago Search for Transit timing variations of Exoplanets (TASTE) have made follow-up transit observations of HAT-P-3b, HAT-P-14b (Nascimbeni et al., 2011a) and HAT-P-13b (Nascimbeni et al., 2011b) using the 1.82m Asiago Astrophysical Observatory, and achieved photometric precisions ranging between 1000-3000ppm. The most prolific ground-based follow-up has so far been by the Transit Light Curve (TLC) Project (Holman & Winn, 2006; Holman et al., 2006), which has consistently achieved milli-magnitude photometric precision on several targets.

To match the wealth of data from the *Kepler* mission, the future goals of ground-based transit observations can be broadly noted as:

1. To discover more transiting systems, by surveying greater numbers of stars and improving the precisions of wide-angle discovery surveys in order to find more Neptune and Earth-sized planets.

2. To make high photometric precision transit follow-up by the use of intermediate to large aperture telescopes ($> 2m$), and possibly the use of detectors that allow for photon counting at optical wavelengths (like STJ[2] imagers, Stankov et al., 2007).

---

[2]Superconducting Transistor Junction

3. To obtain data with continuous coverage in order to sample more transits, and characterize stellar variability. Deriving transit times from continuous monitoring can confirm trends in transit times easily, whereas long-term monitoring improves the chances of catching large timing deviations. Projects like the Las Cumbres Observatory Global Telescope Network (Tufts et al., 2008) are poised for such work.

Appendix A

Notes on the *Agile* Reduction Pipeline

Most of the *Agile* reduction pipeline simply applies standard photometric processing methods. The following are some image processing steps unique to *Agile*.

A.1 Agile's Frame Shift

The fringe frame was created during the early life of *Agile*, when the image coordinates of the pixels were slightly shifted from the image coordinates of the later *Agile* images. Early attempts at fringe subtraction fared poorly, leaving behind residual fringe patterns since the fringe pattern on the model frame and science frames did not match. It was found that there was roughly a shift of 5 pixels in the x and y directions between readouts from these two epochs, since an additional 5 pixel column and row readout buffer was added by the instrumentalist during *Agile*'s calibration (A. Mukadam). We empirically confirmed this shift by matching the locations of hot-pixels on the frames that went into creating the model fringe frame and the later APOSTLE science frames. Hot-pixels are semiconductor elements on the CCD array which are faulty, usually showing significantly more charge than its neighbors. The positions of these faulty pixels are more or less permanent and hence served the purpose of matching images whose pixel coordinates had been offset. Matching the fringe frame to the science target needed to be carried out for I–band images taken after Summer of 2008.

A.2 Robust Outlier Rejection

Image processing steps like dark or flat-combining needed a routine to compute outlier resistant means and medians; such routines are available in standard image processing software like IRAF. However, since we developed a customized pipeline in IDL we wrote an outlier resistant mean/median estimator based of the freely available IDL routine `RESISTANT_MEAN.pro` by H. Fruendenreich. Given an array A, and a cut-off factor $N_{\sigma_{\rm cut}}$ the routine computes the median absolute deviation (MAD), an outlier resistant alternative to the standard deviation, and computes the level of deviation for each point in the array A. The points which are greater than $N_{\sigma_{\rm cut}}$ are thrown out, and the required mean or median is computed from the remaining points.

Appendix B

Metropolis-Hastings Algorithm with Adaptive Jump Controller

Step: 1 Input

- Starting Model Parameters and Jump array ($\boldsymbol{\theta}$, $\boldsymbol{\sigma}_\theta$), with $N_{\rm par}$ free parameters
- NSteps - Number of steps to run the Markov Chain
- Lightcurve (x, y, yerr)
- Parameter bound information

Step: 2 Initiate Variables

- Model Lightcurve (ymod), χ^2(y, yerr, ymod)
- Starting Step: $j_{\rm step} = 0$
- Number of Selected Step: $N_{\rm selected} = 0$
- Acceptance Rate: acr = 0
- Adaptive step-size controller: $f = 1$

Step: 3 Markov Chain

3.1 Check Acceptance Rate

if $j_{\rm step} > 0$ **then:**

acr = $N_{\rm selected}/j_{\rm step}$

else: pass

3.2 Check Accepted Steps

if $N_{\text{selected}} = 100$ **then:**

if $N_{\text{par}} > 1$: $f = 434\ f$/Number of Attempted Steps

if $N_{\text{par}} = 1$: $f = 225\ f$/Number of Attempted Steps

$N_{\text{selected}} = 0$

else: pass

3.3 Check Bounds / Make Jump[1]

while $\boldsymbol{\theta}$ in Bounds:

$\boldsymbol{\theta}_{\text{new}} = \boldsymbol{\theta} + \mathcal{G}(0, \boldsymbol{\sigma}_{\theta}^2) f$

3.4 Compute New Model and Goodness of Fit

- ymod_{new}, χ^2_{new}(y, yerr, ymod_{new})
- $\alpha = e^{-\frac{1}{2}(\chi^2_{\text{new}} - \chi^2)}$
- $u = \text{RandomUniform}(0, 1)$

3.5 Accept or Reject

if $u \leq \min(1, \alpha)$ **then:**

$\boldsymbol{\theta} = \boldsymbol{\theta}_{\text{new}}$

$N_{\text{selected}} = N_{\text{selected}} + 1$

else:

$\boldsymbol{\theta} = \boldsymbol{\theta}$

3.6 Update Variables

- Compute $\text{ymod}_{\text{updated}}$ with $\boldsymbol{\theta}$

[1]Eastman et al. (2012) note that steps out of bounds must be treated as failed selections, and previous steps selected as part of the chain, otherwise the posterior distributions near the bound is undersampled. We do not apply this. This likely affects only the results of the Open LDC chains, since for other chians the integrator spends little time near any parameter bounds.

- Compute χ^2(y, yerr, $\text{ymod}_{\text{updated}}$)
- $j = j + 1$

Appendix C

Sextic Transit Depth Derivation and Solver from TMCMC

The normalized planetary radius ($R_p/R_\star$) can be determined from the transit depth equation 3.2a and 3.2b.

$$D = \frac{R_p^2}{R_\star^2}\frac{(1-u_1(1-\sqrt{1-b^2})-u_2(1-\sqrt{1-b^2})^2)}{(1-\frac{u_1}{3}-\frac{u_2}{6})} \tag{C.1}$$

The normalized radius ($R_p/R_\star$) is implicit in the impact parameter terms, from 3.3b:

$$b = \sqrt{1-(t_T/t_G)(R_p/R_\star)} \tag{C.2a}$$

which can be re-arranged to get,

$$\sqrt{1-b^2} = \sqrt{\frac{t_T}{t_G}\frac{R_p}{R_\star}} \tag{C.2b}$$

when substituted in Eq. C.1, and representing $x = (R_p/R_\star)^{1/2}$, and t_T/t_G as $T_{\rm Ratio}$,

$$D = x^4\frac{1-u_1(1-x\sqrt{T_{\rm Ratio}})-u_2(1-x\sqrt{T_{\rm Ratio}})^2}{1-u_1/3-u_2/6} \tag{C.3a}$$

expanding the square term and multiplying through by the x^4 term gives,

$$D = \frac{(1-u_1-u_2)}{(1-u_1/3-u_2/6)}x^4 + \frac{\sqrt{T_{\rm Ratio}}(u_1+2u_2)}{(1-u_1/3-u_2/6)}x^5 - \frac{u_2T_{\rm Ratio}}{(1-u_1/3-u_2/6)}x^6 \tag{C.3b}$$

which is a sextic polynomial in $\sqrt{\frac{R_p}{R_\star}}$. Some of the coefficients can be simplified,

$$x^6 - \frac{\sqrt{T_{\rm Ratio}}(u_1+2u_2)}{u_2T_{\rm Ratio}}x^5 - \frac{(1-u_1-u_2)}{u_2T_{\rm Ratio}}x^4 + \frac{(1-u_1/3-u_2/6)}{u_2T_{\rm Ratio}}D = 0 \tag{C.3c}$$

$$x^6 + a_5x^5 + a_4x^4 + a_0 = 0 \tag{C.3d}$$

where the coefficients of the polynomial terms are

$$\begin{aligned} a_5 &= \frac{-(u_1+2u_2)}{u_2\sqrt{T_{\rm Ratio}}} \\ a_4 &= \frac{-(1-u_1-u_2)}{u_2 T_{\rm Ratio}} \\ a_0 &= \frac{(1-u_1/3-u_2/6)}{u_2 T_{\rm Ratio}} D \end{aligned}$$

The sextic equation in x has no analytic solution, so we use Newton's method to determine its roots when there are real roots. Sturm's theorem states that the number of real roots of a polynomial inside an interval is given by the number of sign changes of the Sturm sequence evaluated at the end points of this interval. The Sturm sequence (or Sturm chain) is a finite set of polynomials of decreasing degree, which for the sextic in Eq. C.3d are,

$$\begin{aligned} f_6 &= a_0 + a_4 x^4 + a_5 x^5 + x^6 \\ f_5 &= 4a_4 x^3 + 5a_5 x^4 + 6x^5 \\ f_4 &= \left(\frac{12a_4 - 5a_5^2}{36}\right) x^4 - \frac{1}{9} a_4 a_5 x^3 + a_0 \\ f_3 &= \frac{144 a_4^2 \left(4a_4 - a_5^2\right)}{\left(12a_4 - 5a_5^2\right)^2} x^3 - \frac{216 a_0}{12a_4 - 5a_5^2} x + \frac{36 a_0 a_5 \left(25a_5^2 - 84a_4\right)}{\left(12a_4 - 5a_5^2\right)^2} \\ f_2 &= \frac{a_0 \left(12a_4 - 5a_5^2\right)^2}{24 a_4^2 \left(4a_4 - a_5^2\right)} x^2 + \frac{5 a_0 a_5 \left(12a_4 - 5a_5^2\right)^2}{144 a_4^2 \left(4a_4 - a_5^2\right)} x + \frac{a_0 \left(12a_4 - 5a_5^2\right)^2}{36 a_4 \left(4a_4 - a_5^2\right)} \\ f_1 &= -\frac{4\left(\left(25a_5^4 - 124 a_4 a_5^2 + 96 a_4^2\right) a_4^2 + 54 a_0 \left(12a_4 - 5a_5^2\right)\right)}{\left(12a_4 - 5a_5^2\right)^2} x \\ &\quad + \frac{4a_5 \left(20 a_4^3 \left(4a_4 - a_5^2\right) - 9a_0 \left(84a_4 - 25a_5^2\right)\right)}{\left(12a_4 - 5a_5^2\right)^2} \\ f_0 &= \Big(a_0 \left(12a_4 - 5a_5^2\right)^2 \Big(256 \left(4a_4 - a_5^2\right) a_4^5 + 46656 a_0^2 \\ &\quad + a_0 \left(-3125 a_5^6 + 22500 a_4 a_5^4 - 43200 a_4^2 a_5^2 + 13824 a_4^3\right)\Big)\Big) \\ &\quad / 16 \left(\left(25a_5^4 - 124 a_4 a_5^2 + 96 a_4^2\right) a_4^2 + 54 a_0 \left(12a_4 - 5a_5^2\right)\right)^2 \end{aligned}$$

the two highest order polynomials in the Sturm chain are the polynomial to be evaluated, and its first derivative. The remaining functions are lower order polynomials determined by polynomial division, computed using `PolynomialRemainder`

(in *Mathematica 7* Wolfram Research, Inc., 2008). After computing the two highest order polynomials in the Sturm chain, the remaining are computed using $f_n = \texttt{PolynomialRemainder}(f_{n+2}, f_{n+1})$, where n is the order of the Sturm polynomial to be computed. Before looking for the root of the sextic, the Sturm chain is evaluated at $x = (0,1)$[1], the range of physically acceptable values for x. The difference between the number of sign changes for the lower bounds $[f_6(0) \rightarrow f_5(0) \rightarrow f_4(0) \rightarrow f_3(0) \rightarrow f_2(0) \rightarrow f_1(0) \rightarrow f_0(0)]$ and upper bounds $[f_6(1) \rightarrow f_5(1) \rightarrow f_4(1) \rightarrow f_3(1) \rightarrow f_2(1) \rightarrow f_1(1) \rightarrow f_0(1)]$ gives the number of real roots. So an equal number of sign changes in both evaluations mean there are no real roots in the given range. For most transit parameters real roots exist, and the evaluation of the root is done using Newton's method. The root is isolated by iterative evaluations of the intersection of the tangent of the polynomial with the x-axis;

$$x_{j+1} = x_j - \frac{f_6(x_j)}{f_5(x_j)} \tag{C.4}$$

until $f_6(x_j)/f_5(x_j) <$ 1e-10 (the tolerance level).

Doing this analytic check for real-roots avoided the return of false roots, and prevented the root finder from stagnating around local minima or maxima.

[1]the lower limit was numerically set to 1e-8 to avoid overflow errors

Appendix D

MCMC Statistics

D.1 Supplementary Tables: Pearson's r & Spearman's ρ

Markov Chains are likely to converge and accurately describe the posterior distributions when the mutual correlations between the given parameters are small. The following figures tabulate the Pearson's r (Correlation Coefficient) and Spearman's ρ (Rank Correlation Coefficient) for all Markov chains run in this study. The Pearson's r notes the strength of linear trends in the scatter data of two variables, with 0 indicating no linear trend, and 1 indicating a perfectly linear relation between the two distributions. Note that we present the absolute values of the coefficients so the presented values may include negative correlations. The scatter distribution of two variables could easily have a non-linear (but non-random) relation which does not show a linear relation (e.g. a sine function). To roughly quantify such relations we can use the rank correlation (Spearman's ρ). In other words Spearman's ρ notes how well the scatter distribution of two variables can be represented by a monotonic function. A ρ of 1 shows strong rank correlation and 0 shows none. Spearman's ρ is good for finding "banana" degeneracies. Once again, we present only absolute values of ρ. Joint-Probabilities which have both Pearson's r and Spearman's ρ close to zero are well suited for M-H. When significant correlations (> 0.5) are seen, the entries are bolded in the tables that follow.

Table D.1: Correlation Stats for GJ 1214 Chain Parameters

Params ↓	Chain →	FLDC		OLDC		MDFLDC	
1	2	$\lvert r\rvert$	$\lvert\rho\rvert$	$\lvert r\rvert$	$\lvert\rho\rvert$	$\lvert r\rvert$	$\lvert\rho\rvert$
T_1	T_2	< 0.01	< 0.01	< 0.01	< 0.01	< 0.01	< 0.01
T_1	T_3	< 0.01	< 0.01	< 0.01	< 0.01	< 0.01	< 0.01
T_1	T_4	< 0.01	< 0.01	< 0.01	< 0.01	< 0.01	< 0.01
T_1	T_5	< 0.01	< 0.01	< 0.01	< 0.01	< 0.01	< 0.01
T_1	T_6	0.01	< 0.01	< 0.01	< 0.01	< 0.01	< 0.01
T_1	$D_{(r')}$	0.08	0.08	0.04	0.04	–	–
T_1	t_G	< 0.01	< 0.01	0.05	0.05	0.01	0.01
T_1	t_T	0.03	0.03	0.05	0.05	0.04	0.04
T_2	T_3	< 0.01	< 0.01	< 0.01	< 0.01	< 0.01	< 0.01
T_2	T_4	< 0.01	< 0.01	< 0.01	< 0.01	< 0.01	< 0.01
T_2	T_5	< 0.01	< 0.01	< 0.01	< 0.01	< 0.01	< 0.01
T_2	T_6	< 0.01	< 0.01	0.01	0.01	0.02	0.01
T_2	$D_{(r')}$	< 0.01	< 0.01	< 0.01	< 0.01	–	–
T_2	t_G	0.02	0.02	0.03	0.02	0.03	0.03
T_2	t_T	0.05	0.05	0.02	0.02	0.05	0.05
T_3	T_4	< 0.01	< 0.01	< 0.01	< 0.01	< 0.01	< 0.01
T_3	T_5	< 0.01	< 0.01	< 0.01	< 0.01	< 0.01	< 0.01
T_3	T_6	< 0.01	< 0.01	< 0.01	< 0.01	< 0.01	< 0.01
T_3	$D_{(r')}$	< 0.01	< 0.01	0.03	0.03	–	–
T_3	t_G	0.02	0.02	0.04	0.04	0.02	0.02
T_3	t_T	0.02	0.02	0.02	0.01	0.02	0.02
T_4	T_5	< 0.01	< 0.01	< 0.01	< 0.01	< 0.01	< 0.01
T_4	T_6	< 0.01	< 0.01	< 0.01	< 0.01	< 0.01	< 0.01
T_4	$D_{(r')}$	0.01	< 0.01	0.02	0.01	–	–
T_4	t_G	0.03	0.03	0.04	0.04	0.02	0.02
T_4	t_T	0.05	0.05	0.04	0.05	0.04	0.04
T_5	T_6	< 0.01	< 0.01	< 0.01	< 0.01	< 0.01	< 0.01
T_5	$D_{(r')}$	0.02	0.02	0.02	0.02	–	–
T_5	t_G	0.04	0.04	0.03	0.03	0.03	0.03
T_5	t_T	< 0.01	< 0.01	< 0.01	< 0.01	< 0.01	< 0.01
T_6	$D_{(r')}$	0.02	0.02	< 0.01	< 0.01	–	–
T_6	t_G	0.05	0.05	0.06	0.05	0.05	0.04
T_6	t_T	0.13	0.12	0.04	0.04	0.12	0.12
$D_{(r')}$	t_G	0.32	0.30	0.04	0.04	–	–
$D_{(r')}$	t_T	0.10	0.09	0.03	0.02	–	–
t_G	t_T	0.04	0.03	**0.51**	0.49	0.04	0.03
T_1	T_2	< 0.01	< 0.01	< 0.01	< 0.01	< 0.01	< 0.01

continued on next page...

Table D.1 – Correlation Stats for GJ 1214 continued from previous page							
Params ↓	Chain →	FLDC		OLDC		MDFLDC	
1	2	$\lvert r\rvert$	$\lvert\rho\rvert$	$\lvert r\rvert$	$\lvert\rho\rvert$	$\lvert r\rvert$	$\lvert\rho\rvert$
T_1	T_3	< 0.01	< 0.01	< 0.01	< 0.01	< 0.01	< 0.01
T_1	T_4	< 0.01	< 0.01	< 0.01	< 0.01	< 0.01	< 0.01
T_1	T_5	< 0.01	< 0.01	< 0.01	< 0.01	< 0.01	< 0.01
T_1	T_6	0.01	< 0.01	< 0.01	< 0.01	< 0.01	< 0.01
T_1	$D_{(r')}$	0.08	0.08	0.04	0.04	–	–
T_1	t_G	< 0.01	< 0.01	0.05	0.05	0.01	0.01
T_1	t_T	0.03	0.03	0.05	0.05	0.04	0.04
T_1	$v1_{(r')}$	–	–	0.05	0.05	–	–
T_1	$v2_{(r')}$	–	–	< 0.01	< 0.01	–	–
T_2	T_3	< 0.01	< 0.01	< 0.01	< 0.01	< 0.01	< 0.01
T_2	T_4	< 0.01	< 0.01	< 0.01	< 0.01	< 0.01	< 0.01
T_2	T_5	< 0.01	< 0.01	< 0.01	< 0.01	< 0.01	< 0.01
T_2	T_6	< 0.01	< 0.01	0.01	0.01	0.02	0.01
T_2	$D_{(r')}$	< 0.01	< 0.01	< 0.01	< 0.01	–	–
T_2	t_G	0.02	0.02	0.03	0.02	0.03	0.03
T_2	t_T	0.05	0.05	0.02	0.02	0.05	0.05
T_2	$v1_{(r')}$	–	–	0.05	0.05	–	–
T_2	$v2_{(r')}$	–	–	0.05	0.05	–	–
T_3	T_4	< 0.01	< 0.01	< 0.01	< 0.01	< 0.01	< 0.01
T_3	T_5	< 0.01	< 0.01	< 0.01	< 0.01	< 0.01	< 0.01
T_3	T_6	< 0.01	< 0.01	< 0.01	< 0.01	< 0.01	< 0.01
T_3	$D_{(r')}$	< 0.01	< 0.01	0.03	0.03	–	–
T_3	t_G	0.02	0.02	0.04	0.04	0.02	0.02
T_3	t_T	0.02	0.02	0.02	0.01	0.02	0.02
T_3	$v1_{(r')}$	–	–	< 0.01	< 0.01	–	–
T_3	$v2_{(r')}$	–	–	0.03	0.03	–	–
T_4	T_5	< 0.01	< 0.01	< 0.01	< 0.01	< 0.01	< 0.01
T_4	T_6	< 0.01	< 0.01	< 0.01	< 0.01	< 0.01	< 0.01
T_4	$D_{(r')}$	0.01	< 0.01	0.02	0.01	–	–
T_4	t_G	0.03	0.03	0.04	0.04	0.02	0.02
T_4	t_T	0.05	0.05	0.04	0.05	0.04	0.04
T_4	$v1_{(r')}$	–	–	0.02	0.02	–	–
T_4	$v2_{(r')}$	–	–	0.01	< 0.01	–	–
T_5	T_6	< 0.01	< 0.01	< 0.01	< 0.01	< 0.01	< 0.01
T_5	$D_{(r')}$	0.02	0.02	0.02	0.02	–	–
T_5	t_G	0.04	0.04	0.03	0.03	0.03	0.03
T_5	t_T	< 0.01	< 0.01	< 0.01	< 0.01	< 0.01	< 0.01
T_5	$v1_{(r')}$	–	–	0.01	0.01	–	–

continued on next page...

Table D.1 – Correlation Stats for GJ 1214 continued from previous page

Params ↓	Chain →	FLDC		OLDC		MDFLDC	
1	2	$\|r\|$	$\|\rho\|$	$\|r\|$	$\|\rho\|$	$\|r\|$	$\|\rho\|$
T_5	$v2_{(r')}$	–	–	0.01	0.01	–	–
T_6	$D_{(r')}$	0.02	0.02	< 0.01	< 0.01	–	–
T_6	t_G	0.05	0.05	0.06	0.05	0.05	0.04
T_6	t_T	0.13	0.12	0.04	0.04	0.12	0.12
T_6	$v1_{(r')}$	–	–	0.01	< 0.01	–	–
T_6	$v2_{(r')}$	–	–	0.02	0.02	–	–
$D_{(r')}$	t_G	0.32	0.30	0.04	0.04	–	–
$D_{(r')}$	t_T	0.10	0.09	0.03	0.02	–	–
$D_{(r')}$	$v1_{(r')}$	–	–	0.11	0.11	–	–
$D_{(r')}$	$v2_{(r')}$	–	–	0.41	0.39	–	–
t_G	t_T	0.04	0.03	**0.51**	0.49	0.04	0.03
t_G	$v1_{(r')}$	–	–	0.40	0.39	–	–
t_G	$v2_{(r')}$	–	–	0.09	0.10	–	–
t_T	$v1_{(r')}$	–	–	**0.89**	**0.89**	–	–
t_T	$v2_{(r')}$	–	–	**0.52**	**0.54**	–	–
$v1_{(r')}$	$v2_{(r')}$	–	–	**0.79**	**0.80**	–	–
T_1	T_2	< 0.01	< 0.01	< 0.01	< 0.01	< 0.01	< 0.01
T_1	T_3	< 0.01	< 0.01	< 0.01	< 0.01	< 0.01	< 0.01
T_1	T_4	< 0.01	< 0.01	< 0.01	< 0.01	< 0.01	< 0.01
T_1	T_5	< 0.01	< 0.01	< 0.01	< 0.01	< 0.01	< 0.01
T_1	T_6	0.01	< 0.01	< 0.01	< 0.01	< 0.01	< 0.01
T_1	$D_{(1)}$	–	–	–	–	0.17	0.16
T_1	$D_{(2)}$	–	–	–	–	< 0.01	< 0.01
T_1	$D_{(3)}$	–	–	–	–	< 0.01	< 0.01
T_1	$D_{(4)}$	–	–	–	–	< 0.01	< 0.01
T_1	$D_{(5)}$	–	–	–	–	< 0.01	< 0.01
T_1	$D_{(6)}$	–	–	–	–	< 0.01	< 0.01
T_1	t_G	< 0.01	< 0.01	0.05	0.05	0.01	0.01
T_1	t_T	0.03	0.03	0.05	0.05	0.04	0.04
T_2	T_3	< 0.01	< 0.01	< 0.01	< 0.01	< 0.01	< 0.01
T_2	T_4	< 0.01	< 0.01	< 0.01	< 0.01	< 0.01	< 0.01
T_2	T_5	< 0.01	< 0.01	< 0.01	< 0.01	< 0.01	< 0.01
T_2	T_6	< 0.01	< 0.01	0.01	0.01	0.02	0.01
T_2	$D_{(1)}$	–	–	–	–	< 0.01	< 0.01
T_2	$D_{(2)}$	–	–	–	–	< 0.01	< 0.01
T_2	$D_{(3)}$	–	–	–	–	< 0.01	< 0.01
T_2	$D_{(4)}$	–	–	–	–	< 0.01	< 0.01
T_2	$D_{(5)}$	–	–	–	–	< 0.01	< 0.01

continued on next page...

Table D.1 – Correlation Stats for GJ 1214 continued from previous page

Params ↓	Chain →	FLDC		OLDC		MDFLDC	
1	2	$\lvert r\rvert$	$\lvert\rho\rvert$	$\lvert r\rvert$	$\lvert\rho\rvert$	$\lvert r\rvert$	$\lvert\rho\rvert$
T_2	$D_{(6)}$	–	–	–	–	< 0.01	< 0.01
T_2	t_G	0.02	0.02	0.03	0.02	0.03	0.03
T_2	t_T	0.05	0.05	0.02	0.02	0.05	0.05
T_3	T_4	< 0.01	< 0.01	< 0.01	< 0.01	< 0.01	< 0.01
T_3	T_5	< 0.01	< 0.01	< 0.01	< 0.01	< 0.01	< 0.01
T_3	T_6	< 0.01	< 0.01	< 0.01	< 0.01	< 0.01	< 0.01
T_3	$D_{(1)}$	–	–	–	–	< 0.01	< 0.01
T_3	$D_{(2)}$	–	–	–	–	< 0.01	< 0.01
T_3	$D_{(3)}$	–	–	–	–	0.03	0.03
T_3	$D_{(4)}$	–	–	–	–	< 0.01	< 0.01
T_3	$D_{(5)}$	–	–	–	–	< 0.01	< 0.01
T_3	$D_{(6)}$	–	–	–	–	< 0.01	< 0.01
T_3	t_G	0.02	0.02	0.04	0.04	0.02	0.02
T_3	t_T	0.02	0.02	0.02	0.01	0.02	0.02
T_4	T_5	< 0.01	< 0.01	< 0.01	< 0.01	< 0.01	< 0.01
T_4	T_6	< 0.01	< 0.01	< 0.01	< 0.01	< 0.01	< 0.01
T_4	$D_{(1)}$	–	–	–	–	0.01	0.01
T_4	$D_{(2)}$	–	–	–	–	< 0.01	< 0.01
T_4	$D_{(3)}$	–	–	–	–	< 0.01	< 0.01
T_4	$D_{(4)}$	–	–	–	–	0.02	0.02
T_4	$D_{(5)}$	–	–	–	–	< 0.01	< 0.01
T_4	$D_{(6)}$	–	–	–	–	< 0.01	< 0.01
T_4	t_G	0.03	0.03	0.04	0.04	0.02	0.02
T_4	t_T	0.05	0.05	0.04	0.05	0.04	0.04
T_5	T_6	< 0.01	< 0.01	< 0.01	< 0.01	< 0.01	< 0.01
T_5	$D_{(1)}$	–	–	–	–	< 0.01	< 0.01
T_5	$D_{(2)}$	–	–	–	–	< 0.01	< 0.01
T_5	$D_{(3)}$	–	–	–	–	< 0.01	< 0.01
T_5	$D_{(4)}$	–	–	–	–	< 0.01	< 0.01
T_5	$D_{(5)}$	–	–	–	–	0.03	0.02
T_5	$D_{(6)}$	–	–	–	–	< 0.01	< 0.01
T_5	t_G	0.04	0.04	0.03	0.03	0.03	0.03
T_5	t_T	< 0.01	< 0.01	< 0.01	< 0.01	< 0.01	< 0.01
T_6	$D_{(1)}$	–	–	–	–	< 0.01	< 0.01
T_6	$D_{(2)}$	–	–	–	–	0.01	0.01
T_6	$D_{(3)}$	–	–	–	–	0.01	0.01
T_6	$D_{(4)}$	–	–	–	–	< 0.01	< 0.01
T_6	$D_{(5)}$	–	–	–	–	0.01	0.01

continued on next page...

Table D.1 – Correlation Stats for GJ 1214 continued from previous page

Params ↓	Chain →	FLDC		OLDC		MDFLDC	
1	2	$\|r\|$	$\|\rho\|$	$\|r\|$	$\|\rho\|$	$\|r\|$	$\|\rho\|$
T_6	$D_{(6)}$	–	–	–	–	< 0.01	< 0.01
T_6	t_G	0.05	0.05	0.06	0.05	0.05	0.04
T_6	t_T	0.13	0.12	0.04	0.04	0.12	0.12
$D_{(1)}$	$D_{(2)}$	–	–	–	–	0.03	0.03
$D_{(1)}$	$D_{(3)}$	–	–	–	–	0.04	0.04
$D_{(1)}$	$D_{(4)}$	–	–	–	–	0.02	0.02
$D_{(1)}$	$D_{(5)}$	–	–	–	–	0.03	0.03
$D_{(1)}$	$D_{(6)}$	–	–	–	–	0.15	0.14
$D_{(1)}$	t_G	–	–	–	–	0.09	0.09
$D_{(1)}$	t_T	–	–	–	–	< 0.01	< 0.01
$D_{(2)}$	$D_{(3)}$	–	–	–	–	0.04	0.04
$D_{(2)}$	$D_{(4)}$	–	–	–	–	0.02	0.02
$D_{(2)}$	$D_{(5)}$	–	–	–	–	0.03	0.03
$D_{(2)}$	$D_{(6)}$	–	–	–	–	0.12	0.11
$D_{(2)}$	t_G	–	–	–	–	0.11	0.11
$D_{(2)}$	t_T	–	–	–	–	0.07	0.07
$D_{(3)}$	$D_{(4)}$	–	–	–	–	0.01	0.02
$D_{(3)}$	$D_{(5)}$	–	–	–	–	0.04	0.04
$D_{(3)}$	$D_{(6)}$	–	–	–	–	0.12	0.12
$D_{(3)}$	t_G	–	–	–	–	0.10	0.10
$D_{(3)}$	t_T	–	–	–	–	0.05	0.05
$D_{(4)}$	$D_{(5)}$	–	–	–	–	0.03	0.03
$D_{(4)}$	$D_{(6)}$	–	–	–	–	0.11	0.11
$D_{(4)}$	t_G	–	–	–	–	0.04	0.04
$D_{(4)}$	t_T	–	–	–	–	< 0.01	< 0.01
$D_{(5)}$	$D_{(6)}$	–	–	–	–	0.10	0.09
$D_{(5)}$	t_G	–	–	–	–	0.09	0.09
$D_{(5)}$	t_T	–	–	–	–	0.07	0.07
$D_{(6)}$	t_G	–	–	–	–	0.20	0.19
$D_{(6)}$	t_T	–	–	–	–	0.04	0.04
t_G	t_T	0.04	0.03	**0.51**	0.49	0.04	0.03

Table D.2: Correlation Stats for XO-2 Chain Parameters

Params ↓	Chain →	FLDC		OLDC		MDFLDC	
1	2	$\lvert r\rvert$	$\lvert\rho\rvert$	$\lvert r\rvert$	$\lvert\rho\rvert$	$\lvert r\rvert$	$\lvert\rho\rvert$
T_1	T_2	0.02	0.02	< 0.01	< 0.01	< 0.01	< 0.01
T_1	T_3	0.02	0.02	< 0.01	< 0.01	< 0.01	< 0.01
T_1	T_4	< 0.01	< 0.01	0.02	0.02	< 0.01	< 0.01
T_1	T_5	0.02	0.03	< 0.01	< 0.01	< 0.01	< 0.01
T_1	T_6	0.02	0.02	0.05	0.05	0.04	0.04
T_1	T_7	0.05	0.04	< 0.01	< 0.01	< 0.01	< 0.01
T_1	T_8	0.03	0.03	< 0.01	< 0.01	< 0.01	< 0.01
T_1	T_9	< 0.01	< 0.01	< 0.01	< 0.01	< 0.01	< 0.01
T_1	T_{10}	0.01	0.01	< 0.01	< 0.01	< 0.01	< 0.01
T_1	$D_{(I)}$	0.06	0.06	0.05	0.05	–	–
T_1	$D_{(r')}$	< 0.01	0.01	< 0.01	< 0.01	–	–
T_1	t_G	0.03	0.03	0.05	0.05	0.08	0.08
T_1	t_T	0.10	0.10	0.07	0.06	0.10	0.10
T_2	T_3	< 0.01	0.01	0.02	0.02	< 0.01	< 0.01
T_2	T_4	< 0.01	0.02	< 0.01	< 0.01	< 0.01	< 0.01
T_2	T_5	0.01	0.03	< 0.01	< 0.01	< 0.01	< 0.01
T_2	T_6	< 0.01	< 0.01	0.04	0.03	0.02	0.02
T_2	T_7	0.01	0.01	< 0.01	< 0.01	0.01	0.01
T_2	T_8	0.05	0.05	< 0.01	< 0.01	< 0.01	< 0.01
T_2	T_9	0.02	0.01	0.01	< 0.01	< 0.01	0.01
T_2	T_{10}	0.01	0.02	< 0.01	< 0.01	< 0.01	< 0.01
T_2	$D_{(I)}$	0.04	0.03	0.06	0.06	–	–
T_2	$D_{(r')}$	0.04	0.04	< 0.01	< 0.01	–	–
T_2	t_G	0.03	0.03	0.02	0.02	0.03	0.02
T_2	t_T	0.06	0.06	0.03	0.03	0.05	0.04
T_3	T_4	0.03	0.03	0.01	0.01	0.01	0.01
T_3	T_5	0.02	< 0.01	< 0.01	< 0.01	< 0.01	< 0.01
T_3	T_6	0.04	0.04	0.04	0.04	< 0.01	< 0.01
T_3	T_7	< 0.01	< 0.01	< 0.01	< 0.01	0.01	0.01
T_3	T_8	< 0.01	< 0.01	< 0.01	< 0.01	< 0.01	< 0.01
T_3	T_9	0.01	0.01	< 0.01	< 0.01	< 0.01	< 0.01
T_3	T_{10}	0.02	0.03	0.01	< 0.01	< 0.01	< 0.01
T_3	$D_{(I)}$	0.11	0.10	0.12	0.12	–	–
T_3	$D_{(r')}$	< 0.01	< 0.01	< 0.01	< 0.01	–	–
T_3	t_G	0.06	0.05	0.05	0.04	0.02	0.02
T_3	t_T	0.05	0.05	0.01	< 0.01	0.05	0.05
T_4	T_5	< 0.01	< 0.01	< 0.01	0.01	0.02	0.02

continued on next page...

Table D.2 – Correlation Stats for XO-2 continued from previous page

Params ↓	Chain →	FLDC		OLDC		MDFLDC	
1	2	$\lvert r\rvert$	$\lvert\rho\rvert$	$\lvert r\rvert$	$\lvert\rho\rvert$	$\lvert r\rvert$	$\lvert\rho\rvert$
T_4	T_6	0.03	0.02	0.04	0.04	0.01	0.01
T_4	T_7	0.02	0.02	0.02	0.02	0.01	0.01
T_4	T_8	0.07	0.08	< 0.01	< 0.01	0.01	0.01
T_4	T_9	0.04	0.04	< 0.01	< 0.01	< 0.01	< 0.01
T_4	T_{10}	0.04	0.05	0.02	0.03	< 0.01	< 0.01
T_4	$D_{(I)}$	0.11	0.11	0.08	0.07	–	–
T_4	$D_{(r')}$	0.05	0.04	0.02	0.02	–	–
T_4	t_G	0.08	0.08	0.11	0.11	0.06	0.06
T_4	t_T	0.04	0.03	0.04	0.03	0.06	0.07
T_5	T_6	0.04	0.04	0.03	0.02	< 0.01	< 0.01
T_5	T_7	0.01	0.02	< 0.01	< 0.01	< 0.01	0.01
T_5	T_8	0.04	0.04	< 0.01	< 0.01	< 0.01	< 0.01
T_5	T_9	< 0.01	< 0.01	< 0.01	< 0.01	0.01	0.01
T_5	T_{10}	0.03	0.03	< 0.01	< 0.01	< 0.01	< 0.01
T_5	$D_{(I)}$	0.03	0.03	< 0.01	< 0.01	–	–
T_5	$D_{(r')}$	0.08	0.07	< 0.01	< 0.01	–	–
T_5	t_G	< 0.01	< 0.01	0.03	0.03	0.01	0.01
T_5	t_T	0.01	0.01	0.01	< 0.01	< 0.01	< 0.01
T_6	T_7	0.07	0.06	0.02	0.01	0.05	0.04
T_6	T_8	0.07	0.06	0.01	0.01	0.04	0.03
T_6	T_9	0.04	0.03	< 0.01	< 0.01	0.03	0.03
T_6	T_{10}	0.05	0.05	0.02	0.02	< 0.01	< 0.01
T_6	$D_{(I)}$	0.03	0.03	< 0.01	< 0.01	–	–
T_6	$D_{(r')}$	0.06	0.05	< 0.01	< 0.01	–	–
T_6	t_G	0.05	0.05	0.04	0.04	0.03	0.04
T_6	t_T	0.32	0.30	0.12	0.12	0.33	0.32
T_7	T_8	< 0.01	0.01	0.04	0.04	0.02	0.02
T_7	T_9	< 0.01	< 0.01	0.04	0.04	0.01	0.01
T_7	T_{10}	0.02	0.03	< 0.01	< 0.01	< 0.01	< 0.01
T_7	$D_{(I)}$	< 0.01	< 0.01	0.02	0.02	–	–
T_7	$D_{(r')}$	0.06	0.05	0.05	0.05	–	–
T_7	t_G	0.07	0.07	0.09	0.08	0.03	0.02
T_7	t_T	0.17	0.17	0.07	0.06	0.17	0.16
T_8	T_9	0.01	0.01	< 0.01	< 0.01	< 0.01	< 0.01
T_8	T_{10}	< 0.01	< 0.01	< 0.01	< 0.01	< 0.01	< 0.01
T_8	$D_{(I)}$	0.06	0.06	< 0.01	< 0.01	–	–
T_8	$D_{(r')}$	0.10	0.10	0.05	0.04	–	–
T_8	t_G	0.03	0.03	0.02	0.02	< 0.01	< 0.01

continued on next page...

Table D.2 – Correlation Stats for XO-2 continued from previous page

Params ↓	Chain →	FLDC		OLDC		MDFLDC	
1	2	$\|r\|$	$\|\rho\|$	$\|r\|$	$\|\rho\|$	$\|r\|$	$\|\rho\|$
T_8	t_T	0.11	0.11	0.04	0.04	0.11	0.10
T_9	T_{10}	0.05	0.05	< 0.01	< 0.01	0.01	0.01
T_9	$D_{(I)}$	0.02	0.02	< 0.01	< 0.01	–	–
T_9	$D_{(r')}$	0.12	0.12	0.11	0.10	–	–
T_9	t_G	< 0.01	< 0.01	0.01	0.01	< 0.01	< 0.01
T_9	t_T	0.09	0.08	0.01	0.01	0.09	0.09
T_{10}	$D_{(I)}$	0.01	0.03	< 0.01	< 0.01	–	–
T_{10}	$D_{(r')}$	0.06	0.04	0.02	0.02	–	–
T_{10}	t_G	0.02	0.02	< 0.01	< 0.01	< 0.01	< 0.01
T_{10}	t_T	< 0.01	< 0.01	< 0.01	< 0.01	< 0.01	< 0.01
$D_{(I)}$	$D_{(r')}$	0.13	0.12	0.10	0.09	–	–
$D_{(I)}$	t_G	0.33	0.31	0.22	0.21	–	–
$D_{(I)}$	t_T	0.06	0.06	< 0.01	0.02	–	–
$D_{(r')}$	t_G	0.12	0.12	0.07	0.07	–	–
$D_{(r')}$	t_T	0.01	0.01	0.02	0.03	–	–
t_G	t_T	0.08	0.08	0.45	0.44	0.03	0.04
T_1	T_2	0.02	0.02	< 0.01	< 0.01	< 0.01	< 0.01
T_1	T_3	0.02	0.02	< 0.01	< 0.01	< 0.01	< 0.01
T_1	T_4	< 0.01	< 0.01	0.02	0.02	< 0.01	< 0.01
T_1	T_5	0.02	0.03	< 0.01	< 0.01	< 0.01	< 0.01
T_1	T_6	0.02	0.02	0.05	0.05	0.04	0.04
T_1	T_7	0.05	0.04	< 0.01	< 0.01	< 0.01	< 0.01
T_1	T_8	0.03	0.03	< 0.01	< 0.01	< 0.01	< 0.01
T_1	T_9	< 0.01	< 0.01	< 0.01	< 0.01	< 0.01	< 0.01
T_1	T_{10}	0.01	0.01	< 0.01	< 0.01	< 0.01	< 0.01
T_1	$D_{(I)}$	0.06	0.06	0.05	0.05	–	–
T_1	$D_{(r')}$	< 0.01	0.01	< 0.01	< 0.01	–	–
T_1	t_G	0.03	0.03	0.05	0.05	0.08	0.08
T_1	t_T	0.10	0.10	0.07	0.06	0.10	0.10
T_1	$v1_{(I)}$	–	–	< 0.01	< 0.01	–	–
T_1	$v1_{(r')}$	–	–	0.05	0.05	–	–
T_1	$v2_{(I)}$	–	–	0.02	0.02	–	–
T_1	$v2_{(r')}$	–	–	0.03	0.03	–	–
T_2	T_3	< 0.01	0.01	0.02	0.02	< 0.01	< 0.01
T_2	T_4	< 0.01	0.02	< 0.01	< 0.01	< 0.01	< 0.01
T_2	T_5	0.01	0.03	< 0.01	< 0.01	< 0.01	< 0.01
T_2	T_6	< 0.01	< 0.01	0.04	0.03	0.02	0.02
T_2	T_7	0.01	0.01	< 0.01	< 0.01	0.01	0.01

continued on next page...

Table D.2 – Correlation Stats for XO-2 continued from previous page

Params ↓	Chain →	FLDC		OLDC		MDFLDC	
1	2	$\lvert r\rvert$	$\lvert\rho\rvert$	$\lvert r\rvert$	$\lvert\rho\rvert$	$\lvert r\rvert$	$\lvert\rho\rvert$
T_2	T_8	0.05	0.05	< 0.01	< 0.01	< 0.01	< 0.01
T_2	T_9	0.02	0.01	0.01	< 0.01	< 0.01	0.01
T_2	T_{10}	0.01	0.02	< 0.01	< 0.01	< 0.01	< 0.01
T_2	$D_{(I)}$	0.04	0.03	0.06	0.06	–	–
T_2	$D_{(r')}$	0.04	0.04	< 0.01	< 0.01	–	–
T_2	t_G	0.03	0.03	0.02	0.02	0.03	0.02
T_2	t_T	0.06	0.06	0.03	0.03	0.05	0.04
T_2	$v1_{(I)}$	–	–	< 0.01	< 0.01	–	–
T_2	$v1_{(r')}$	–	–	0.03	0.03	–	–
T_2	$v2_{(I)}$	–	–	0.01	0.01	–	–
T_2	$v2_{(r')}$	–	–	0.03	0.03	–	–
T_3	T_4	0.03	0.03	0.01	0.01	0.01	0.01
T_3	T_5	0.02	< 0.01	< 0.01	< 0.01	< 0.01	< 0.01
T_3	T_6	0.04	0.04	0.04	0.04	< 0.01	< 0.01
T_3	T_7	< 0.01	< 0.01	< 0.01	< 0.01	0.01	0.01
T_3	T_8	< 0.01	< 0.01	< 0.01	< 0.01	< 0.01	< 0.01
T_3	T_9	0.01	0.01	< 0.01	< 0.01	< 0.01	< 0.01
T_3	T_{10}	0.02	0.03	0.01	< 0.01	< 0.01	< 0.01
T_3	$D_{(I)}$	0.11	0.10	0.12	0.12	–	–
T_3	$D_{(r')}$	< 0.01	< 0.01	< 0.01	< 0.01	–	–
T_3	t_G	0.06	0.05	0.05	0.04	0.02	0.02
T_3	t_T	0.05	0.05	0.01	< 0.01	0.05	0.05
T_3	$v1_{(I)}$	–	–	0.05	0.04	–	–
T_3	$v1_{(r')}$	–	–	0.02	0.01	–	–
T_3	$v2_{(I)}$	–	–	0.02	0.02	–	–
T_3	$v2_{(r')}$	–	–	0.01	0.01	–	–
T_4	T_5	< 0.01	< 0.01	< 0.01	0.01	0.02	0.02
T_4	T_6	0.03	0.02	0.04	0.04	0.01	0.01
T_4	T_7	0.02	0.02	0.02	0.02	0.01	0.01
T_4	T_8	0.07	0.08	< 0.01	< 0.01	0.01	0.01
T_4	T_9	0.04	0.04	< 0.01	< 0.01	< 0.01	< 0.01
T_4	T_{10}	0.04	0.05	0.02	0.03	< 0.01	< 0.01
T_4	$D_{(I)}$	0.11	0.11	0.08	0.07	–	–
T_4	$D_{(r')}$	0.05	0.04	0.02	0.02	–	–
T_4	t_G	0.08	0.08	0.11	0.11	0.06	0.06
T_4	t_T	0.04	0.03	0.04	0.03	0.06	0.07
T_4	$v1_{(I)}$	–	–	0.07	0.07	–	–
T_4	$v1_{(r')}$	–	–	0.01	0.01	–	–

continued on next page...

Table D.2 – Correlation Stats for XO-2 continued from previous page

Params ↓	Chain →	FLDC		OLDC		MDFLDC	
1	2	$\lvert r\rvert$	$\lvert\rho\rvert$	$\lvert r\rvert$	$\lvert\rho\rvert$	$\lvert r\rvert$	$\lvert\rho\rvert$
T_4	$v2_{(I)}$	–	–	0.06	0.06	–	–
T_4	$v2_{(r')}$	–	–	< 0.01	< 0.01	–	–
T_5	T_6	0.04	0.04	0.03	0.02	< 0.01	< 0.01
T_5	T_7	0.01	0.02	< 0.01	< 0.01	< 0.01	0.01
T_5	T_8	0.04	0.04	< 0.01	< 0.01	< 0.01	< 0.01
T_5	T_9	< 0.01	< 0.01	< 0.01	< 0.01	0.01	0.01
T_5	T_{10}	0.03	0.03	< 0.01	< 0.01	< 0.01	< 0.01
T_5	$D_{(I)}$	0.03	0.03	< 0.01	< 0.01	–	–
T_5	$D_{(r')}$	0.08	0.07	< 0.01	< 0.01	–	–
T_5	t_G	< 0.01	< 0.01	0.03	0.03	0.01	0.01
T_5	t_T	0.01	0.01	0.01	< 0.01	< 0.01	< 0.01
T_5	$v1_{(I)}$	–	–	< 0.01	0.01	–	–
T_5	$v1_{(r')}$	–	–	< 0.01	< 0.01	–	–
T_5	$v2_{(I)}$	–	–	0.02	0.01	–	–
T_5	$v2_{(r')}$	–	–	< 0.01	0.01	–	–
T_6	T_7	0.07	0.06	0.02	0.01	0.05	0.04
T_6	T_8	0.07	0.06	0.01	0.01	0.04	0.03
T_6	T_9	0.04	0.03	< 0.01	< 0.01	0.03	0.03
T_6	T_{10}	0.05	0.05	0.02	0.02	< 0.01	< 0.01
T_6	$D_{(I)}$	0.03	0.03	< 0.01	< 0.01	–	–
T_6	$D_{(r')}$	0.06	0.05	< 0.01	< 0.01	–	–
T_6	t_G	0.05	0.05	0.04	0.04	0.03	0.04
T_6	t_T	0.32	0.30	0.12	0.12	0.33	0.32
T_6	$v1_{(I)}$	–	–	0.10	0.10	–	–
T_6	$v1_{(r')}$	–	–	0.08	0.08	–	–
T_6	$v2_{(I)}$	–	–	0.08	0.08	–	–
T_6	$v2_{(r')}$	–	–	0.05	0.05	–	–
T_7	T_8	< 0.01	0.01	0.04	0.04	0.02	0.02
T_7	T_9	< 0.01	< 0.01	0.04	0.04	0.01	0.01
T_7	T_{10}	0.02	0.03	< 0.01	< 0.01	< 0.01	< 0.01
T_7	$D_{(I)}$	< 0.01	< 0.01	0.02	0.02	–	–
T_7	$D_{(r')}$	0.06	0.05	0.05	0.05	–	–
T_7	t_G	0.07	0.07	0.09	0.08	0.03	0.02
T_7	t_T	0.17	0.17	0.07	0.06	0.17	0.16
T_7	$v1_{(I)}$	–	–	0.07	0.06	–	–
T_7	$v1_{(r')}$	–	–	0.08	0.07	–	–
T_7	$v2_{(I)}$	–	–	0.06	0.06	–	–
T_7	$v2_{(r')}$	–	–	0.03	0.03	–	–

continued on next page...

Table D.2 – Correlation Stats for XO-2 continued from previous page

Params ↓	Chain →	FLDC		OLDC		MDFLDC	
1	2	$\lvert r\rvert$	$\lvert\rho\rvert$	$\lvert r\rvert$	$\lvert\rho\rvert$	$\lvert r\rvert$	$\lvert\rho\rvert$
T_8	T_9	0.01	0.01	< 0.01	< 0.01	< 0.01	< 0.01
T_8	T_{10}	< 0.01	< 0.01	< 0.01	< 0.01	< 0.01	< 0.01
T_8	$D_{(I)}$	0.06	0.06	< 0.01	< 0.01	–	–
T_8	$D_{(r')}$	0.10	0.10	0.05	0.04	–	–
T_8	t_G	0.03	0.03	0.02	0.02	< 0.01	< 0.01
T_8	t_T	0.11	0.11	0.04	0.04	0.11	0.10
T_8	$v1_{(I)}$	–	–	0.03	0.03	–	–
T_8	$v1_{(r')}$	–	–	0.04	0.04	–	–
T_8	$v2_{(I)}$	–	–	0.03	0.03	–	–
T_8	$v2_{(r')}$	–	–	< 0.01	< 0.01	–	–
T_9	T_{10}	0.05	0.05	< 0.01	< 0.01	0.01	0.01
T_9	$D_{(I)}$	0.02	0.02	< 0.01	< 0.01	–	–
T_9	$D_{(r')}$	0.12	0.12	0.11	0.10	–	–
T_9	t_G	< 0.01	< 0.01	0.01	0.01	< 0.01	< 0.01
T_9	t_T	0.09	0.08	0.01	0.01	0.09	0.09
T_9	$v1_{(I)}$	–	–	0.01	< 0.01	–	–
T_9	$v1_{(r')}$	–	–	0.03	0.03	–	–
T_9	$v2_{(I)}$	–	–	< 0.01	< 0.01	–	–
T_9	$v2_{(r')}$	–	–	0.04	0.03	–	–
T_{10}	$D_{(I)}$	0.01	0.03	< 0.01	< 0.01	–	–
T_{10}	$D_{(r')}$	0.06	0.04	0.02	0.02	–	–
T_{10}	t_G	0.02	0.02	< 0.01	< 0.01	< 0.01	< 0.01
T_{10}	t_T	< 0.01	< 0.01	< 0.01	< 0.01	< 0.01	< 0.01
T_{10}	$v1_{(I)}$	–	–	< 0.01	< 0.01	–	–
T_{10}	$v1_{(r')}$	–	–	< 0.01	< 0.01	–	–
T_{10}	$v2_{(I)}$	–	–	< 0.01	< 0.01	–	–
T_{10}	$v2_{(r')}$	–	–	< 0.01	< 0.01	–	–
$D_{(I)}$	$D_{(r')}$	0.13	0.12	0.10	0.09	–	–
$D_{(I)}$	t_G	0.33	0.31	0.22	0.21	–	–
$D_{(I)}$	t_T	0.06	0.06	< 0.01	0.02	–	–
$D_{(I)}$	$v1_{(I)}$	–	–	0.15	0.16	–	–
$D_{(I)}$	$v1_{(r')}$	–	–	< 0.01	0.01	–	–
$D_{(I)}$	$v2_{(I)}$	–	–	0.37	0.36	–	–
$D_{(I)}$	$v2_{(r')}$	–	–	0.02	0.02	–	–
$D_{(r')}$	t_G	0.12	0.12	0.07	0.07	–	–
$D_{(r')}$	t_T	0.01	0.01	0.02	0.03	–	–
$D_{(r')}$	$v1_{(I)}$	–	–	< 0.01	< 0.01	–	–
$D_{(r')}$	$v1_{(r')}$	–	–	0.19	0.19	–	–

continued on next page...

Table D.2 – Correlation Stats for XO-2 continued from previous page

Params ↓	Chain →	FLDC		OLDC		MDFLDC	
1	2	$\lvert r\rvert$	$\lvert\rho\rvert$	$\lvert r\rvert$	$\lvert\rho\rvert$	$\lvert r\rvert$	$\lvert\rho\rvert$
$D_{(r')}$	$v2_{(I)}$	–	–	< 0.01	< 0.01	–	–
$D_{(r')}$	$v2_{(r')}$	–	–	0.36	0.35	–	–
t_G	t_T	0.08	0.08	0.45	0.44	0.03	0.04
t_G	$v1_{(I)}$	–	–	0.43	0.42	–	–
t_G	$v1_{(r')}$	–	–	0.29	0.28	–	–
t_G	$v2_{(I)}$	–	–	0.32	0.32	–	–
t_G	$v2_{(r')}$	–	–	0.18	0.18	–	–
t_T	$v1_{(I)}$	–	–	**0.81**	**0.80**	–	–
t_T	$v1_{(r')}$	–	–	**0.75**	**0.74**	–	–
t_T	$v2_{(I)}$	–	–	**0.64**	**0.63**	–	–
t_T	$v2_{(r')}$	–	–	**0.50**	0.50	–	–
$v1_{(I)}$	$v1_{(r')}$	–	–	**0.62**	**0.60**	–	–
$v1_{(I)}$	$v2_{(I)}$	–	–	**0.88**	**0.88**	–	–
$v1_{(I)}$	$v2_{(r')}$	–	–	0.42	0.41	–	–
$v1_{(r')}$	$v2_{(I)}$	–	–	0.49	0.48	–	–
$v1_{(r')}$	$v2_{(r')}$	–	–	**0.85**	**0.85**	–	–
$v2_{(I)}$	$v2_{(r')}$	–	–	0.35	0.35	–	–
T_1	T_2	0.02	0.02	< 0.01	< 0.01	< 0.01	< 0.01
T_1	T_3	0.02	0.02	< 0.01	< 0.01	< 0.01	< 0.01
T_1	T_4	< 0.01	< 0.01	0.02	0.02	< 0.01	< 0.01
T_1	T_5	0.02	0.03	< 0.01	< 0.01	< 0.01	< 0.01
T_1	T_6	0.02	0.02	0.05	0.05	0.04	0.04
T_1	T_7	0.05	0.04	< 0.01	< 0.01	< 0.01	< 0.01
T_1	T_8	0.03	0.03	< 0.01	< 0.01	< 0.01	< 0.01
T_1	T_9	< 0.01	< 0.01	< 0.01	< 0.01	< 0.01	< 0.01
T_1	T_{10}	0.01	0.01	< 0.01	< 0.01	< 0.01	< 0.01
T_1	$D_{(1)}$	–	–	–	–	0.13	0.12
T_1	$D_{(10)}$	–	–	–	–	< 0.01	< 0.01
T_1	$D_{(2)}$	–	–	–	–	0.02	0.01
T_1	$D_{(3)}$	–	–	–	–	< 0.01	< 0.01
T_1	$D_{(4)}$	–	–	–	–	< 0.01	< 0.01
T_1	$D_{(5)}$	–	–	–	–	0.01	0.01
T_1	$D_{(6)}$	–	–	–	–	< 0.01	< 0.01
T_1	$D_{(7)}$	–	–	–	–	< 0.01	< 0.01
T_1	$D_{(8)}$	–	–	–	–	< 0.01	< 0.01
T_1	$D_{(9)}$	–	–	–	–	< 0.01	< 0.01
T_1	t_G	0.03	0.03	0.05	0.05	0.08	0.08
T_1	t_T	0.10	0.10	0.07	0.06	0.10	0.10

continued on next page...

Table D.2 – Correlation Stats for XO-2 continued from previous page

Params ↓	Chain →	FLDC		OLDC		MDFLDC	
1	2	$\lvert r\rvert$	$\lvert\rho\rvert$	$\lvert r\rvert$	$\lvert\rho\rvert$	$\lvert r\rvert$	$\lvert\rho\rvert$
T_2	T_3	< 0.01	0.01	0.02	0.02	< 0.01	< 0.01
T_2	T_4	< 0.01	0.02	< 0.01	< 0.01	< 0.01	< 0.01
T_2	T_5	0.01	0.03	< 0.01	< 0.01	< 0.01	< 0.01
T_2	T_6	< 0.01	< 0.01	0.04	0.03	0.02	0.02
T_2	T_7	0.01	0.01	< 0.01	< 0.01	0.01	0.01
T_2	T_8	0.05	0.05	< 0.01	< 0.01	< 0.01	< 0.01
T_2	T_9	0.02	0.01	0.01	< 0.01	< 0.01	0.01
T_2	T_{10}	0.01	0.02	< 0.01	< 0.01	< 0.01	< 0.01
T_2	$D_{(1)}$	–	–	–	–	0.02	0.01
T_2	$D_{(10)}$	–	–	–	–	< 0.01	< 0.01
T_2	$D_{(2)}$	–	–	–	–	0.15	0.14
T_2	$D_{(3)}$	–	–	–	–	< 0.01	< 0.01
T_2	$D_{(4)}$	–	–	–	–	< 0.01	< 0.01
T_2	$D_{(5)}$	–	–	–	–	0.01	0.01
T_2	$D_{(6)}$	–	–	–	–	< 0.01	< 0.01
T_2	$D_{(7)}$	–	–	–	–	< 0.01	< 0.01
T_2	$D_{(8)}$	–	–	–	–	< 0.01	< 0.01
T_2	$D_{(9)}$	–	–	–	–	< 0.01	< 0.01
T_2	t_G	0.03	0.03	0.02	0.02	0.03	0.02
T_2	t_T	0.06	0.06	0.03	0.03	0.05	0.04
T_3	T_4	0.03	0.03	0.01	0.01	0.01	0.01
T_3	T_5	0.02	< 0.01	< 0.01	< 0.01	< 0.01	< 0.01
T_3	T_6	0.04	0.04	0.04	0.04	< 0.01	< 0.01
T_3	T_7	< 0.01	< 0.01	< 0.01	< 0.01	0.01	0.01
T_3	T_8	< 0.01	< 0.01	< 0.01	< 0.01	< 0.01	< 0.01
T_3	T_9	0.01	0.01	< 0.01	< 0.01	< 0.01	< 0.01
T_3	T_{10}	0.02	0.03	0.01	< 0.01	< 0.01	< 0.01
T_3	$D_{(1)}$	–	–	–	–	< 0.01	< 0.01
T_3	$D_{(10)}$	–	–	–	–	< 0.01	< 0.01
T_3	$D_{(2)}$	–	–	–	–	< 0.01	< 0.01
T_3	$D_{(3)}$	–	–	–	–	0.23	0.22
T_3	$D_{(4)}$	–	–	–	–	0.01	0.01
T_3	$D_{(5)}$	–	–	–	–	< 0.01	0.01
T_3	$D_{(6)}$	–	–	–	–	< 0.01	< 0.01
T_3	$D_{(7)}$	–	–	–	–	< 0.01	< 0.01
T_3	$D_{(8)}$	–	–	–	–	< 0.01	< 0.01
T_3	$D_{(9)}$	–	–	–	–	0.01	0.01
T_3	t_G	0.06	0.05	0.05	0.04	0.02	0.02

continued on next page...

Table D.2 – Correlation Stats for XO-2 continued from previous page

Params ↓	Chain →	FLDC		OLDC		MDFLDC	
1	2	$\lvert r\rvert$	$\lvert\rho\rvert$	$\lvert r\rvert$	$\lvert\rho\rvert$	$\lvert r\rvert$	$\lvert\rho\rvert$
T_3	t_T	0.05	0.05	0.01	< 0.01	0.05	0.05
T_4	T_5	< 0.01	< 0.01	< 0.01	0.01	0.02	0.02
T_4	T_6	0.03	0.02	0.04	0.04	0.01	0.01
T_4	T_7	0.02	0.02	0.02	0.02	0.01	0.01
T_4	T_8	0.07	0.08	< 0.01	< 0.01	0.01	0.01
T_4	T_9	0.04	0.04	< 0.01	< 0.01	< 0.01	< 0.01
T_4	T_{10}	0.04	0.05	0.02	0.03	< 0.01	< 0.01
T_4	$D_{(1)}$	–	–	–	–	< 0.01	0.01
T_4	$D_{(10)}$	–	–	–	–	0.02	0.01
T_4	$D_{(2)}$	–	–	–	–	< 0.01	< 0.01
T_4	$D_{(3)}$	–	–	–	–	0.01	0.01
T_4	$D_{(4)}$	–	–	–	–	0.14	0.13
T_4	$D_{(5)}$	–	–	–	–	< 0.01	< 0.01
T_4	$D_{(6)}$	–	–	–	–	0.01	0.01
T_4	$D_{(7)}$	–	–	–	–	0.03	0.03
T_4	$D_{(8)}$	–	–	–	–	< 0.01	< 0.01
T_4	$D_{(9)}$	–	–	–	–	0.03	0.03
T_4	t_G	0.08	0.08	0.11	0.11	0.06	0.06
T_4	t_T	0.04	0.03	0.04	0.03	0.06	0.07
T_5	T_6	0.04	0.04	0.03	0.02	< 0.01	< 0.01
T_5	T_7	0.01	0.02	< 0.01	< 0.01	< 0.01	0.01
T_5	T_8	0.04	0.04	< 0.01	< 0.01	< 0.01	< 0.01
T_5	T_9	< 0.01	< 0.01	< 0.01	< 0.01	0.01	0.01
T_5	T_{10}	0.03	0.03	< 0.01	< 0.01	< 0.01	< 0.01
T_5	$D_{(1)}$	–	–	–	–	< 0.01	< 0.01
T_5	$D_{(10)}$	–	–	–	–	< 0.01	< 0.01
T_5	$D_{(2)}$	–	–	–	–	< 0.01	< 0.01
T_5	$D_{(3)}$	–	–	–	–	< 0.01	< 0.01
T_5	$D_{(4)}$	–	–	–	–	< 0.01	< 0.01
T_5	$D_{(5)}$	–	–	–	–	0.15	0.14
T_5	$D_{(6)}$	–	–	–	–	< 0.01	< 0.01
T_5	$D_{(7)}$	–	–	–	–	< 0.01	< 0.01
T_5	$D_{(8)}$	–	–	–	–	< 0.01	< 0.01
T_5	$D_{(9)}$	–	–	–	–	< 0.01	< 0.01
T_5	t_G	< 0.01	< 0.01	0.03	0.03	0.01	0.01
T_5	t_T	0.01	0.01	0.01	< 0.01	< 0.01	< 0.01
T_6	T_7	0.07	0.06	0.02	0.01	0.05	0.04
T_6	T_8	0.07	0.06	0.01	0.01	0.04	0.03

continued on next page...

Table D.2 – Correlation Stats for XO-2 continued from previous page

Params ↓	Chain →	FLDC		OLDC		MDFLDC	
1	2	$\|r\|$	$\|\rho\|$	$\|r\|$	$\|\rho\|$	$\|r\|$	$\|\rho\|$
T_6	T_9	0.04	0.03	< 0.01	< 0.01	0.03	0.03
T_6	T_{10}	0.05	0.05	0.02	0.02	< 0.01	< 0.01
T_6	$D_{(1)}$	–	–	–	–	0.01	0.01
T_6	$D_{(10)}$	–	–	–	–	0.02	0.02
T_6	$D_{(2)}$	–	–	–	–	0.03	0.03
T_6	$D_{(3)}$	–	–	–	–	0.02	0.01
T_6	$D_{(4)}$	–	–	–	–	0.02	0.02
T_6	$D_{(5)}$	–	–	–	–	0.04	0.04
T_6	$D_{(6)}$	–	–	–	–	0.08	0.08
T_6	$D_{(7)}$	–	–	–	–	< 0.01	< 0.01
T_6	$D_{(8)}$	–	–	–	–	< 0.01	< 0.01
T_6	$D_{(9)}$	–	–	–	–	< 0.01	< 0.01
T_6	t_G	0.05	0.05	0.04	0.04	0.03	0.04
T_6	t_T	0.32	0.30	0.12	0.12	0.33	0.32
T_7	T_8	< 0.01	0.01	0.04	0.04	0.02	0.02
T_7	T_9	< 0.01	< 0.01	0.04	0.04	0.01	0.01
T_7	T_{10}	0.02	0.03	< 0.01	< 0.01	< 0.01	< 0.01
T_7	$D_{(1)}$	–	–	–	–	0.02	0.02
T_7	$D_{(10)}$	–	–	–	–	< 0.01	< 0.01
T_7	$D_{(2)}$	–	–	–	–	< 0.01	< 0.01
T_7	$D_{(3)}$	–	–	–	–	< 0.01	< 0.01
T_7	$D_{(4)}$	–	–	–	–	0.03	0.02
T_7	$D_{(5)}$	–	–	–	–	< 0.01	< 0.01
T_7	$D_{(6)}$	–	–	–	–	< 0.01	< 0.01
T_7	$D_{(7)}$	–	–	–	–	0.10	0.09
T_7	$D_{(8)}$	–	–	–	–	< 0.01	< 0.01
T_7	$D_{(9)}$	–	–	–	–	0.02	0.01
T_7	t_G	0.07	0.07	0.09	0.08	0.03	0.02
T_7	t_T	0.17	0.17	0.07	0.06	0.17	0.16
T_8	T_9	0.01	0.01	< 0.01	< 0.01	< 0.01	< 0.01
T_8	T_{10}	< 0.01	< 0.01	< 0.01	< 0.01	< 0.01	< 0.01
T_8	$D_{(1)}$	–	–	–	–	< 0.01	< 0.01
T_8	$D_{(10)}$	–	–	–	–	< 0.01	< 0.01
T_8	$D_{(2)}$	–	–	–	–	0.01	0.01
T_8	$D_{(3)}$	–	–	–	–	< 0.01	< 0.01
T_8	$D_{(4)}$	–	–	–	–	< 0.01	< 0.01
T_8	$D_{(5)}$	–	–	–	–	0.01	0.01
T_8	$D_{(6)}$	–	–	–	–	< 0.01	< 0.01

continued on next page...

Table D.2 – Correlation Stats for XO-2 continued from previous page

Params ↓	Chain →	FLDC		OLDC		MDFLDC	
1	2	$\lvert r\rvert$	$\lvert\rho\rvert$	$\lvert r\rvert$	$\lvert\rho\rvert$	$\lvert r\rvert$	$\lvert\rho\rvert$
T_8	$D_{(7)}$	–	–	–	–	< 0.01	< 0.01
T_8	$D_{(8)}$	–	–	–	–	0.17	0.17
T_8	$D_{(9)}$	–	–	–	–	< 0.01	< 0.01
T_8	t_G	0.03	0.03	0.02	0.02	< 0.01	< 0.01
T_8	t_T	0.11	0.11	0.04	0.04	0.11	0.10
T_9	T_{10}	0.05	0.05	< 0.01	< 0.01	0.01	0.01
T_9	$D_{(1)}$	–	–	–	–	< 0.01	< 0.01
T_9	$D_{(10)}$	–	–	–	–	< 0.01	< 0.01
T_9	$D_{(2)}$	–	–	–	–	< 0.01	< 0.01
T_9	$D_{(3)}$	–	–	–	–	< 0.01	< 0.01
T_9	$D_{(4)}$	–	–	–	–	< 0.01	< 0.01
T_9	$D_{(5)}$	–	–	–	–	0.02	0.02
T_9	$D_{(6)}$	–	–	–	–	< 0.01	< 0.01
T_9	$D_{(7)}$	–	–	–	–	< 0.01	< 0.01
T_9	$D_{(8)}$	–	–	–	–	< 0.01	< 0.01
T_9	$D_{(9)}$	–	–	–	–	0.14	0.14
T_9	t_G	< 0.01	< 0.01	0.01	0.01	< 0.01	< 0.01
T_9	t_T	0.09	0.08	0.01	0.01	0.09	0.09
T_{10}	$D_{(1)}$	–	–	–	–	< 0.01	< 0.01
T_{10}	$D_{(10)}$	–	–	–	–	0.05	0.05
T_{10}	$D_{(2)}$	–	–	–	–	< 0.01	< 0.01
T_{10}	$D_{(3)}$	–	–	–	–	< 0.01	< 0.01
T_{10}	$D_{(4)}$	–	–	–	–	0.01	0.01
T_{10}	$D_{(5)}$	–	–	–	–	< 0.01	< 0.01
T_{10}	$D_{(6)}$	–	–	–	–	< 0.01	< 0.01
T_{10}	$D_{(7)}$	–	–	–	–	< 0.01	< 0.01
T_{10}	$D_{(8)}$	–	–	–	–	< 0.01	< 0.01
T_{10}	$D_{(9)}$	–	–	–	–	< 0.01	< 0.01
T_{10}	t_G	0.02	0.02	< 0.01	< 0.01	< 0.01	< 0.01
T_{10}	t_T	< 0.01	< 0.01	< 0.01	< 0.01	< 0.01	< 0.01
$D_{(1)}$	$D_{(10)}$	–	–	–	–	0.03	0.03
$D_{(1)}$	$D_{(2)}$	–	–	–	–	0.06	0.05
$D_{(1)}$	$D_{(3)}$	–	–	–	–	0.04	0.04
$D_{(1)}$	$D_{(4)}$	–	–	–	–	0.06	0.06
$D_{(1)}$	$D_{(5)}$	–	–	–	–	0.01	0.01
$D_{(1)}$	$D_{(6)}$	–	–	–	–	0.04	0.03
$D_{(1)}$	$D_{(7)}$	–	–	–	–	0.03	0.03
$D_{(1)}$	$D_{(8)}$	–	–	–	–	0.03	0.03

continued on next page...

Table D.2 – Correlation Stats for XO-2 continued from previous page

Params ↓	Chain →	FLDC		OLDC		MDFLDC	
1	2	$\lvert r\rvert$	$\lvert\rho\rvert$	$\lvert r\rvert$	$\lvert\rho\rvert$	$\lvert r\rvert$	$\lvert\rho\rvert$
$D_{(1)}$	$D_{(9)}$	–	–	–	–	0.05	0.05
$D_{(1)}$	t_G	–	–	–	–	0.45	0.47
$D_{(1)}$	t_T	–	–	–	–	< 0.01	< 0.01
$D_{(10)}$	$D_{(2)}$	–	–	–	–	0.03	0.03
$D_{(10)}$	$D_{(3)}$	–	–	–	–	0.02	0.02
$D_{(10)}$	$D_{(4)}$	–	–	–	–	0.15	0.14
$D_{(10)}$	$D_{(5)}$	–	–	–	–	< 0.01	< 0.01
$D_{(10)}$	$D_{(6)}$	–	–	–	–	0.02	0.02
$D_{(10)}$	$D_{(7)}$	–	–	–	–	0.04	0.03
$D_{(10)}$	$D_{(8)}$	–	–	–	–	0.02	0.02
$D_{(10)}$	$D_{(9)}$	–	–	–	–	0.04	0.04
$D_{(10)}$	t_G	–	–	–	–	0.03	0.03
$D_{(10)}$	t_T	–	–	–	–	0.04	0.04
$D_{(2)}$	$D_{(3)}$	–	–	–	–	0.02	0.01
$D_{(2)}$	$D_{(4)}$	–	–	–	–	0.08	0.07
$D_{(2)}$	$D_{(5)}$	–	–	–	–	< 0.01	< 0.01
$D_{(2)}$	$D_{(6)}$	–	–	–	–	0.01	< 0.01
$D_{(2)}$	$D_{(7)}$	–	–	–	–	0.03	0.03
$D_{(2)}$	$D_{(8)}$	–	–	–	–	0.02	0.02
$D_{(2)}$	$D_{(9)}$	–	–	–	–	0.02	0.02
$D_{(2)}$	t_G	–	–	–	–	0.09	0.08
$D_{(2)}$	t_T	–	–	–	–	0.10	0.10
$D_{(3)}$	$D_{(4)}$	–	–	–	–	0.12	0.12
$D_{(3)}$	$D_{(5)}$	–	–	–	–	< 0.01	< 0.01
$D_{(3)}$	$D_{(6)}$	–	–	–	–	0.02	0.02
$D_{(3)}$	$D_{(7)}$	–	–	–	–	0.03	0.03
$D_{(3)}$	$D_{(8)}$	–	–	–	–	0.02	0.02
$D_{(3)}$	$D_{(9)}$	–	–	–	–	0.04	0.03
$D_{(3)}$	t_G	–	–	–	–	0.06	0.06
$D_{(3)}$	t_T	–	–	–	–	0.01	0.01
$D_{(4)}$	$D_{(5)}$	–	–	–	–	0.03	0.03
$D_{(4)}$	$D_{(6)}$	–	–	–	–	0.12	0.11
$D_{(4)}$	$D_{(7)}$	–	–	–	–	0.22	0.21
$D_{(4)}$	$D_{(8)}$	–	–	–	–	0.15	0.15
$D_{(4)}$	$D_{(9)}$	–	–	–	–	0.25	0.24
$D_{(4)}$	t_G	–	–	–	–	0.12	0.11
$D_{(4)}$	t_T	–	–	–	–	0.06	0.06
$D_{(5)}$	$D_{(6)}$	–	–	–	–	< 0.01	< 0.01

continued on next page...

Table D.2 – Correlation Stats for XO-2 continued from previous page

Params ↓	Chain →	FLDC		OLDC		MDFLDC	
1	2	$\lvert r\rvert$	$\lvert\rho\rvert$	$\lvert r\rvert$	$\lvert\rho\rvert$	$\lvert r\rvert$	$\lvert\rho\rvert$
$D_{(5)}$	$D_{(7)}$	–	–	–	–	< 0.01	< 0.01
$D_{(5)}$	$D_{(8)}$	–	–	–	–	0.01	0.01
$D_{(5)}$	$D_{(9)}$	–	–	–	–	0.01	0.01
$D_{(5)}$	t_G	–	–	–	–	0.02	0.01
$D_{(5)}$	t_T	–	–	–	–	0.08	0.08
$D_{(6)}$	$D_{(7)}$	–	–	–	–	0.03	0.03
$D_{(6)}$	$D_{(8)}$	–	–	–	–	0.03	0.02
$D_{(6)}$	$D_{(9)}$	–	–	–	–	0.03	0.03
$D_{(6)}$	t_G	–	–	–	–	0.05	0.04
$D_{(6)}$	t_T	–	–	–	–	0.02	0.02
$D_{(7)}$	$D_{(8)}$	–	–	–	–	0.03	0.03
$D_{(7)}$	$D_{(9)}$	–	–	–	–	0.06	0.06
$D_{(7)}$	t_G	–	–	–	–	0.02	0.02
$D_{(7)}$	t_T	–	–	–	–	< 0.01	< 0.01
$D_{(8)}$	$D_{(9)}$	–	–	–	–	0.04	0.04
$D_{(8)}$	t_G	–	–	–	–	< 0.01	< 0.01
$D_{(8)}$	t_T	–	–	–	–	< 0.01	< 0.01
$D_{(9)}$	t_G	–	–	–	–	0.05	0.05
$D_{(9)}$	t_T	–	–	–	–	0.03	0.03
t_G	t_T	0.08	0.08	0.45	0.44	0.03	0.04

Table D.3: Correlation Stats for TrES-3 Chain Parameters

Params ↓	Chain →	FLDC		OLDC		MDFLDC	
1	2	$\lvert r\rvert$	$\lvert\rho\rvert$	$\lvert r\rvert$	$\lvert\rho\rvert$	$\lvert r\rvert$	$\lvert\rho\rvert$
T_1	T_2	0.03	0.03	0.03	0.02	0.06	0.05
T_1	T_3	0.02	0.02	< 0.01	< 0.01	< 0.01	< 0.01
T_1	T_4	< 0.01	< 0.01	0.01	0.01	0.02	0.02
T_1	T_5	< 0.01	< 0.01	0.04	0.04	0.05	0.05
T_1	T_6	0.01	< 0.01	0.02	0.02	0.03	0.03
T_1	T_7	< 0.01	< 0.01	< 0.01	< 0.01	< 0.01	< 0.01
T_1	T_8	< 0.01	< 0.01	< 0.01	< 0.01	< 0.01	< 0.01
T_1	T_9	0.02	< 0.01	< 0.01	< 0.01	0.02	0.02
T_1	T_{10}	< 0.01	< 0.01	0.03	0.03	0.02	0.02
T_1	T_{11}	0.01	0.01	< 0.01	< 0.01	0.02	0.02
T_1	$D_{(r')}$	0.01	< 0.01	0.06	0.06	–	–
T_1	t_G	0.03	0.03	0.04	0.03	0.06	0.06
T_1	t_T	0.04	0.03	0.02	0.03	0.16	0.15
T_2	T_3	0.05	0.04	0.01	0.01	< 0.01	< 0.01
T_2	T_4	0.02	0.02	< 0.01	< 0.01	0.02	0.01
T_2	T_5	0.01	0.02	0.02	0.02	0.03	0.03
T_2	T_6	0.02	0.01	< 0.01	< 0.01	< 0.01	< 0.01
T_2	T_7	< 0.01	< 0.01	< 0.01	< 0.01	< 0.01	< 0.01
T_2	T_8	0.02	0.02	< 0.01	< 0.01	< 0.01	< 0.01
T_2	T_9	0.02	0.02	0.01	0.01	< 0.01	< 0.01
T_2	T_{10}	0.01	0.01	0.01	0.01	0.02	0.02
T_2	T_{11}	< 0.01	< 0.01	< 0.01	< 0.01	0.01	0.01
T_2	$D_{(r')}$	0.09	0.09	0.11	0.11	–	–
T_2	t_G	0.06	0.06	0.10	0.10	0.12	0.11
T_2	t_T	0.14	0.14	0.08	0.07	0.16	0.15
T_3	T_4	0.02	< 0.01	< 0.01	< 0.01	< 0.01	< 0.01
T_3	T_5	< 0.01	< 0.01	0.01	0.01	< 0.01	< 0.01
T_3	T_6	< 0.01	< 0.01	< 0.01	< 0.01	< 0.01	< 0.01
T_3	T_7	< 0.01	< 0.01	< 0.01	< 0.01	< 0.01	< 0.01
T_3	T_8	0.03	0.04	< 0.01	< 0.01	< 0.01	< 0.01
T_3	T_9	0.02	0.01	< 0.01	< 0.01	< 0.01	< 0.01
T_3	T_{10}	0.01	< 0.01	< 0.01	< 0.01	< 0.01	< 0.01
T_3	T_{11}	0.01	0.02	< 0.01	< 0.01	< 0.01	< 0.01
T_3	$D_{(r')}$	0.03	0.02	< 0.01	< 0.01	–	–
T_3	t_G	0.03	0.03	0.05	0.05	0.03	0.03
T_3	t_T	0.05	0.04	0.07	0.07	0.04	0.04
T_4	T_5	0.04	0.03	< 0.01	< 0.01	0.02	0.01

continued on next page...

Table D.3 – Correlation Stats for TrES-3 continued from previous page

Params ↓	Chain →	FLDC		OLDC		MDFLDC	
1	2	$\lvert r\rvert$	$\lvert\rho\rvert$	$\lvert r\rvert$	$\lvert\rho\rvert$	$\lvert r\rvert$	$\lvert\rho\rvert$
T_4	T_6	< 0.01	< 0.01	0.01	0.01	< 0.01	< 0.01
T_4	T_7	< 0.01	0.01	< 0.01	< 0.01	< 0.01	< 0.01
T_4	T_8	< 0.01	< 0.01	< 0.01	< 0.01	< 0.01	< 0.01
T_4	T_9	0.01	0.01	< 0.01	< 0.01	< 0.01	0.01
T_4	T_{10}	< 0.01	< 0.01	0.01	< 0.01	< 0.01	< 0.01
T_4	T_{11}	0.02	0.01	< 0.01	< 0.01	< 0.01	< 0.01
T_4	$D_{(r')}$	0.06	0.05	0.05	0.05	–	–
T_4	t_G	0.01	0.01	0.01	< 0.01	0.03	0.03
T_4	t_T	0.05	0.04	0.01	< 0.01	0.06	0.05
T_5	T_6	< 0.01	< 0.01	< 0.01	< 0.01	0.02	0.01
T_5	T_7	0.02	0.01	< 0.01	< 0.01	0.01	0.01
T_5	T_8	< 0.01	< 0.01	< 0.01	< 0.01	0.01	0.01
T_5	T_9	< 0.01	0.01	< 0.01	< 0.01	< 0.01	< 0.01
T_5	T_{10}	< 0.01	0.01	0.01	0.01	0.02	0.02
T_5	T_{11}	0.02	< 0.01	< 0.01	< 0.01	0.01	0.01
T_5	$D_{(r')}$	0.02	0.03	0.03	0.03	–	–
T_5	t_G	< 0.01	0.01	0.06	0.06	0.02	0.02
T_5	t_T	0.08	0.08	0.05	0.05	0.03	0.03
T_6	T_7	0.01	0.01	< 0.01	< 0.01	< 0.01	< 0.01
T_6	T_8	< 0.01	< 0.01	< 0.01	< 0.01	< 0.01	< 0.01
T_6	T_9	0.04	0.03	< 0.01	< 0.01	< 0.01	< 0.01
T_6	T_{10}	0.01	0.01	< 0.01	< 0.01	< 0.01	< 0.01
T_6	T_{11}	< 0.01	< 0.01	< 0.01	< 0.01	< 0.01	< 0.01
T_6	$D_{(r')}$	0.02	0.02	0.01	0.01	–	–
T_6	t_G	0.05	0.05	0.02	0.02	0.06	0.06
T_6	t_T	< 0.01	< 0.01	0.06	0.06	0.03	0.03
T_7	T_8	< 0.01	< 0.01	< 0.01	< 0.01	< 0.01	< 0.01
T_7	T_9	< 0.01	< 0.01	< 0.01	< 0.01	< 0.01	< 0.01
T_7	T_{10}	0.03	0.03	< 0.01	< 0.01	< 0.01	< 0.01
T_7	T_{11}	< 0.01	< 0.01	< 0.01	< 0.01	< 0.01	< 0.01
T_7	$D_{(r')}$	< 0.01	< 0.01	0.03	0.02	–	–
T_7	t_G	< 0.01	< 0.01	0.02	0.02	< 0.01	< 0.01
T_7	t_T	< 0.01	< 0.01	0.03	0.02	< 0.01	< 0.01
T_8	T_9	0.03	0.03	< 0.01	< 0.01	0.01	0.01
T_8	T_{10}	0.02	0.02	< 0.01	< 0.01	< 0.01	< 0.01
T_8	T_{11}	< 0.01	0.02	< 0.01	< 0.01	< 0.01	< 0.01
T_8	$D_{(r')}$	< 0.01	< 0.01	0.02	0.02	–	–
T_8	t_G	0.03	0.02	< 0.01	< 0.01	< 0.01	< 0.01

continued on next page...

Table D.3 – Correlation Stats for TrES-3 continued from previous page

Params ↓	Chain →	FLDC		OLDC		MDFLDC	
1	2	$\|r\|$	$\|\rho\|$	$\|r\|$	$\|\rho\|$	$\|r\|$	$\|\rho\|$
T_8	t_T	0.04	0.04	< 0.01	0.01	< 0.01	< 0.01
T_9	T_{10}	< 0.01	< 0.01	< 0.01	< 0.01	0.02	0.02
T_9	T_{11}	0.06	0.04	< 0.01	< 0.01	< 0.01	< 0.01
T_9	$D_{(r')}$	< 0.01	< 0.01	0.04	0.03	–	–
T_9	t_G	< 0.01	< 0.01	0.06	0.05	0.02	0.01
T_9	t_T	0.02	0.01	0.06	0.05	< 0.01	< 0.01
T_{10}	T_{11}	< 0.01	< 0.01	< 0.01	< 0.01	< 0.01	< 0.01
T_{10}	$D_{(r')}$	0.02	0.02	0.02	0.02	–	–
T_{10}	t_G	0.02	0.02	< 0.01	< 0.01	< 0.01	< 0.01
T_{10}	t_T	0.02	0.01	0.03	0.03	0.02	0.02
T_{11}	$D_{(r')}$	0.02	0.02	0.01	0.01	–	–
T_{11}	t_G	< 0.01	< 0.01	0.03	0.03	0.02	0.02
T_{11}	t_T	0.02	0.02	0.02	0.01	< 0.01	< 0.01
$D_{(r')}$	t_G	**0.86**	**0.85**	**0.61**	**0.52**	–	–
$D_{(r')}$	t_T	**0.74**	**0.71**	0.27	0.17	–	–
t_G	t_T	**0.76**	**0.72**	**0.89**	**0.87**	**0.94**	**0.94**
T_1	T_2	0.03	0.03	0.03	0.02	0.06	0.05
T_1	T_3	0.02	0.02	< 0.01	< 0.01	< 0.01	< 0.01
T_1	T_4	< 0.01	< 0.01	0.01	0.01	0.02	0.02
T_1	T_5	< 0.01	< 0.01	0.04	0.04	0.05	0.05
T_1	T_6	0.01	< 0.01	0.02	0.02	0.03	0.03
T_1	T_7	< 0.01	< 0.01	< 0.01	< 0.01	< 0.01	< 0.01
T_1	T_8	< 0.01	< 0.01	< 0.01	< 0.01	< 0.01	< 0.01
T_1	T_9	0.02	< 0.01	< 0.01	< 0.01	0.02	0.02
T_1	T_{10}	< 0.01	< 0.01	0.03	0.03	0.02	0.02
T_1	T_{11}	0.01	0.01	< 0.01	< 0.01	0.02	0.02
T_1	$D_{(r')}$	0.01	< 0.01	0.06	0.06	–	–
T_1	t_G	0.03	0.03	0.04	0.03	0.06	0.06
T_1	t_T	0.04	0.03	0.02	0.03	0.16	0.15
T_1	$v1_{(r')}$	–	–	0.01	0.01	–	–
T_1	$v2_{(r')}$	–	–	< 0.01	< 0.01	–	–
T_2	T_3	0.05	0.04	0.01	0.01	< 0.01	< 0.01
T_2	T_4	0.02	0.02	< 0.01	< 0.01	0.02	0.01
T_2	T_5	0.01	0.02	0.02	0.02	0.03	0.03
T_2	T_6	0.02	0.01	< 0.01	< 0.01	< 0.01	< 0.01
T_2	T_7	< 0.01	< 0.01	< 0.01	< 0.01	< 0.01	< 0.01
T_2	T_8	0.02	0.02	< 0.01	< 0.01	< 0.01	< 0.01
T_2	T_9	0.02	0.02	0.01	0.01	< 0.01	< 0.01

continued on next page...

Table D.3 – Correlation Stats for TrES-3 continued from previous page

Params ↓	Chain →	FLDC		OLDC		MDFLDC	
1	2	$\lvert r\rvert$	$\lvert\rho\rvert$	$\lvert r\rvert$	$\lvert\rho\rvert$	$\lvert r\rvert$	$\lvert\rho\rvert$
T_2	T_{10}	0.01	0.01	0.01	0.01	0.02	0.02
T_2	T_{11}	< 0.01	< 0.01	< 0.01	< 0.01	0.01	0.01
T_2	$D_{(r')}$	0.09	0.09	0.11	0.11	–	–
T_2	t_G	0.06	0.06	0.10	0.10	0.12	0.11
T_2	t_T	0.14	0.14	0.08	0.07	0.16	0.15
T_2	$v1_{(r')}$	–	–	0.04	0.04	–	–
T_2	$v2_{(r')}$	–	–	< 0.01	< 0.01	–	–
T_3	T_4	0.02	< 0.01	< 0.01	< 0.01	< 0.01	< 0.01
T_3	T_5	< 0.01	< 0.01	0.01	0.01	< 0.01	< 0.01
T_3	T_6	< 0.01	< 0.01	< 0.01	< 0.01	< 0.01	< 0.01
T_3	T_7	< 0.01	< 0.01	< 0.01	< 0.01	< 0.01	< 0.01
T_3	T_8	0.03	0.04	< 0.01	< 0.01	< 0.01	< 0.01
T_3	T_9	0.02	0.01	< 0.01	< 0.01	< 0.01	< 0.01
T_3	T_{10}	0.01	< 0.01	< 0.01	< 0.01	< 0.01	< 0.01
T_3	T_{11}	0.01	0.02	< 0.01	< 0.01	< 0.01	< 0.01
T_3	$D_{(r')}$	0.03	0.02	< 0.01	< 0.01	–	–
T_3	t_G	0.03	0.03	0.05	0.05	0.03	0.03
T_3	t_T	0.05	0.04	0.07	0.07	0.04	0.04
T_3	$v1_{(r')}$	–	–	0.07	0.08	–	–
T_3	$v2_{(r')}$	–	–	0.01	0.01	–	–
T_4	T_5	0.04	0.03	< 0.01	< 0.01	0.02	0.01
T_4	T_6	< 0.01	< 0.01	0.01	0.01	< 0.01	< 0.01
T_4	T_7	< 0.01	0.01	< 0.01	< 0.01	< 0.01	< 0.01
T_4	T_8	< 0.01	< 0.01	< 0.01	< 0.01	< 0.01	< 0.01
T_4	T_9	0.01	0.01	< 0.01	< 0.01	< 0.01	0.01
T_4	T_{10}	< 0.01	< 0.01	0.01	< 0.01	< 0.01	< 0.01
T_4	T_{11}	0.02	0.01	< 0.01	< 0.01	< 0.01	< 0.01
T_4	$D_{(r')}$	0.06	0.05	0.05	0.05	–	–
T_4	t_G	0.01	0.01	0.01	< 0.01	0.03	0.03
T_4	t_T	0.05	0.04	0.01	< 0.01	0.06	0.05
T_4	$v1_{(r')}$	–	–	< 0.01	< 0.01	–	–
T_4	$v2_{(r')}$	–	–	< 0.01	< 0.01	–	–
T_5	T_6	< 0.01	< 0.01	< 0.01	< 0.01	0.02	0.01
T_5	T_7	0.02	0.01	< 0.01	< 0.01	0.01	0.01
T_5	T_8	< 0.01	< 0.01	< 0.01	< 0.01	0.01	0.01
T_5	T_9	< 0.01	0.01	< 0.01	< 0.01	< 0.01	< 0.01
T_5	T_{10}	< 0.01	0.01	0.01	0.01	0.02	0.02
T_5	T_{11}	0.02	< 0.01	< 0.01	< 0.01	0.01	0.01

continued on next page...

Table D.3 – Correlation Stats for TrES-3 continued from previous page

Params ↓	Chain →	FLDC		OLDC		MDFLDC	
1	2	$\|r\|$	$\|\rho\|$	$\|r\|$	$\|\rho\|$	$\|r\|$	$\|\rho\|$
T_5	$D_{(r')}$	0.02	0.03	0.03	0.03	–	–
T_5	t_G	< 0.01	0.01	0.06	0.06	0.02	0.02
T_5	t_T	0.08	0.08	0.05	0.05	0.03	0.03
T_5	$v1_{(r')}$	–	–	0.06	0.06	–	–
T_5	$v2_{(r')}$	–	–	0.02	0.01	–	–
T_6	T_7	0.01	0.01	< 0.01	< 0.01	< 0.01	< 0.01
T_6	T_8	< 0.01	< 0.01	< 0.01	< 0.01	< 0.01	< 0.01
T_6	T_9	0.04	0.03	< 0.01	< 0.01	< 0.01	< 0.01
T_6	T_{10}	0.01	0.01	< 0.01	< 0.01	< 0.01	< 0.01
T_6	T_{11}	< 0.01	< 0.01	< 0.01	< 0.01	< 0.01	< 0.01
T_6	$D_{(r')}$	0.02	0.02	0.01	0.01	–	–
T_6	t_G	0.05	0.05	0.02	0.02	0.06	0.06
T_6	t_T	< 0.01	< 0.01	0.06	0.06	0.03	0.03
T_6	$v1_{(r')}$	–	–	0.06	0.06	–	–
T_6	$v2_{(r')}$	–	–	< 0.01	< 0.01	–	–
T_7	T_8	< 0.01	< 0.01	< 0.01	< 0.01	< 0.01	< 0.01
T_7	T_9	< 0.01	< 0.01	< 0.01	< 0.01	< 0.01	< 0.01
T_7	T_{10}	0.03	0.03	< 0.01	< 0.01	< 0.01	< 0.01
T_7	T_{11}	< 0.01	< 0.01	< 0.01	< 0.01	< 0.01	< 0.01
T_7	$D_{(r')}$	< 0.01	< 0.01	0.03	0.02	–	–
T_7	t_G	< 0.01	< 0.01	0.02	0.02	< 0.01	< 0.01
T_7	t_T	< 0.01	< 0.01	0.03	0.02	< 0.01	< 0.01
T_7	$v1_{(r')}$	–	–	0.03	0.03	–	–
T_7	$v2_{(r')}$	–	–	0.02	0.02	–	–
T_8	T_9	0.03	0.03	< 0.01	< 0.01	0.01	0.01
T_8	T_{10}	0.02	0.02	< 0.01	< 0.01	< 0.01	< 0.01
T_8	T_{11}	< 0.01	0.02	< 0.01	< 0.01	< 0.01	< 0.01
T_8	$D_{(r')}$	< 0.01	< 0.01	0.02	0.02	–	–
T_8	t_G	0.03	0.02	< 0.01	< 0.01	< 0.01	< 0.01
T_8	t_T	0.04	0.04	< 0.01	0.01	< 0.01	< 0.01
T_8	$v1_{(r')}$	–	–	0.01	0.01	–	–
T_8	$v2_{(r')}$	–	–	< 0.01	< 0.01	–	–
T_9	T_{10}	< 0.01	< 0.01	< 0.01	< 0.01	0.02	0.02
T_9	T_{11}	0.06	0.04	< 0.01	< 0.01	< 0.01	< 0.01
T_9	$D_{(r')}$	< 0.01	< 0.01	0.04	0.03	–	–
T_9	t_G	< 0.01	< 0.01	0.06	0.05	0.02	0.01
T_9	t_T	0.02	0.01	0.06	0.05	< 0.01	< 0.01
T_9	$v1_{(r')}$	–	–	0.05	0.05	–	–

continued on next page...

Table D.3 – Correlation Stats for TrES-3 continued from previous page

Params ↓	Chain →	FLDC		OLDC		MDFLDC	
1	2	$\lvert r\rvert$	$\lvert\rho\rvert$	$\lvert r\rvert$	$\lvert\rho\rvert$	$\lvert r\rvert$	$\lvert\rho\rvert$
T_9	$v2_{(r')}$	–	–	< 0.01	< 0.01	–	–
T_{10}	T_{11}	< 0.01	< 0.01	< 0.01	< 0.01	< 0.01	< 0.01
T_{10}	$D_{(r')}$	0.02	0.02	0.02	0.02	–	–
T_{10}	t_G	0.02	0.02	< 0.01	< 0.01	< 0.01	< 0.01
T_{10}	t_T	0.02	0.01	0.03	0.03	0.02	0.02
T_{10}	$v1_{(r')}$	–	–	0.03	0.03	–	–
T_{10}	$v2_{(r')}$	–	–	0.01	0.01	–	–
T_{11}	$D_{(r')}$	0.02	0.02	0.01	0.01	–	–
T_{11}	t_G	< 0.01	< 0.01	0.03	0.03	0.02	0.02
T_{11}	t_T	0.02	0.02	0.02	0.01	< 0.01	< 0.01
T_{11}	$v1_{(r')}$	–	–	0.01	0.01	–	–
T_{11}	$v2_{(r')}$	–	–	0.01	0.01	–	–
$D_{(r')}$	t_G	**0.86**	**0.85**	**0.61**	**0.52**	–	–
$D_{(r')}$	t_T	**0.74**	**0.71**	0.27	0.17	–	–
$D_{(r')}$	$v1_{(r')}$	–	–	0.05	0.05	–	–
$D_{(r')}$	$v2_{(r')}$	–	–	0.48	**0.53**	–	–
t_G	t_T	**0.76**	**0.72**	**0.89**	**0.87**	**0.94**	**0.94**
t_G	$v1_{(r')}$	–	–	**0.78**	**0.75**	–	–
t_G	$v2_{(r')}$	–	–	< 0.01	< 0.01	–	–
t_T	$v1_{(r')}$	–	–	**0.96**	**0.96**	–	–
t_T	$v2_{(r')}$	–	–	0.17	0.22	–	–
$v1_{(r')}$	$v2_{(r')}$	–	–	0.39	0.41	–	–
T_1	T_2	0.03	0.03	0.03	0.02	0.06	0.05
T_1	T_3	0.02	0.02	< 0.01	< 0.01	< 0.01	< 0.01
T_1	T_4	< 0.01	< 0.01	0.01	0.01	0.02	0.02
T_1	T_5	< 0.01	< 0.01	0.04	0.04	0.05	0.05
T_1	T_6	0.01	< 0.01	0.02	0.02	0.03	0.03
T_1	T_7	< 0.01	< 0.01	< 0.01	< 0.01	< 0.01	< 0.01
T_1	T_8	< 0.01	< 0.01	< 0.01	< 0.01	< 0.01	< 0.01
T_1	T_9	0.02	< 0.01	< 0.01	< 0.01	0.02	0.02
T_1	T_{10}	< 0.01	< 0.01	0.03	0.03	0.02	0.02
T_1	T_{11}	0.01	0.01	< 0.01	< 0.01	0.02	0.02
T_1	$D_{(1)}$	–	–	–	–	**0.51**	0.50
T_1	$D_{(10)}$	–	–	–	–	0.07	0.06
T_1	$D_{(11)}$	–	–	–	–	0.08	0.07
T_1	$D_{(2)}$	–	–	–	–	0.02	0.02
T_1	$D_{(3)}$	–	–	–	–	0.09	0.08
T_1	$D_{(4)}$	–	–	–	–	0.10	0.10

continued on next page...

Table D.3 – Correlation Stats for TrES-3 continued from previous page

Params ↓	Chain →	FLDC		OLDC		MDFLDC	
1	2	$\|r\|$	$\|\rho\|$	$\|r\|$	$\|\rho\|$	$\|r\|$	$\|\rho\|$
T_1	$D_{(5)}$	–	–	–	–	0.02	0.02
T_1	$D_{(6)}$	–	–	–	–	0.07	0.07
T_1	$D_{(7)}$	–	–	–	–	0.09	0.09
T_1	$D_{(8)}$	–	–	–	–	0.09	0.08
T_1	$D_{(9)}$	–	–	–	–	0.01	0.01
T_1	t_G	0.03	0.03	0.04	0.03	0.06	0.06
T_1	t_T	0.04	0.03	0.02	0.03	0.16	0.15
T_2	T_3	0.05	0.04	0.01	0.01	< 0.01	< 0.01
T_2	T_4	0.02	0.02	< 0.01	< 0.01	0.02	0.01
T_2	T_5	0.01	0.02	0.02	0.02	0.03	0.03
T_2	T_6	0.02	0.01	< 0.01	< 0.01	< 0.01	< 0.01
T_2	T_7	< 0.01	< 0.01	< 0.01	< 0.01	< 0.01	< 0.01
T_2	T_8	0.02	0.02	< 0.01	< 0.01	< 0.01	< 0.01
T_2	T_9	0.02	0.02	0.01	0.01	< 0.01	< 0.01
T_2	T_{10}	0.01	0.01	0.01	0.01	0.02	0.02
T_2	T_{11}	< 0.01	< 0.01	< 0.01	< 0.01	0.01	0.01
T_2	$D_{(1)}$	–	–	–	–	0.02	0.02
T_2	$D_{(10)}$	–	–	–	–	0.09	0.09
T_2	$D_{(11)}$	–	–	–	–	0.09	0.09
T_2	$D_{(2)}$	–	–	–	–	0.03	0.02
T_2	$D_{(3)}$	–	–	–	–	0.09	0.09
T_2	$D_{(4)}$	–	–	–	–	0.12	0.11
T_2	$D_{(5)}$	–	–	–	–	0.05	0.04
T_2	$D_{(6)}$	–	–	–	–	0.09	0.09
T_2	$D_{(7)}$	–	–	–	–	0.12	0.12
T_2	$D_{(8)}$	–	–	–	–	0.11	0.11
T_2	$D_{(9)}$	–	–	–	–	0.05	0.05
T_2	t_G	0.06	0.06	0.10	0.10	0.12	0.11
T_2	t_T	0.14	0.14	0.08	0.07	0.16	0.15
T_3	T_4	0.02	< 0.01	< 0.01	< 0.01	< 0.01	< 0.01
T_3	T_5	< 0.01	< 0.01	0.01	0.01	< 0.01	< 0.01
T_3	T_6	< 0.01	< 0.01	< 0.01	< 0.01	< 0.01	< 0.01
T_3	T_7	< 0.01	< 0.01	< 0.01	< 0.01	< 0.01	< 0.01
T_3	T_8	0.03	0.04	< 0.01	< 0.01	< 0.01	< 0.01
T_3	T_9	0.02	0.01	< 0.01	< 0.01	< 0.01	< 0.01
T_3	T_{10}	0.01	< 0.01	< 0.01	< 0.01	< 0.01	< 0.01
T_3	T_{11}	0.01	0.02	< 0.01	< 0.01	< 0.01	< 0.01
T_3	$D_{(1)}$	–	–	–	–	0.01	0.01

continued on next page...

Table D.3 – Correlation Stats for TrES-3 continued from previous page

Params ↓	Chain →	FLDC		OLDC		MDFLDC	
1	2	$\|r\|$	$\|\rho\|$	$\|r\|$	$\|\rho\|$	$\|r\|$	$\|\rho\|$
T_3	$D_{(10)}$	–	–	–	–	0.03	0.03
T_3	$D_{(11)}$	–	–	–	–	0.03	0.03
T_3	$D_{(2)}$	–	–	–	–	< 0.01	< 0.01
T_3	$D_{(3)}$	–	–	–	–	< 0.01	< 0.01
T_3	$D_{(4)}$	–	–	–	–	0.03	0.03
T_3	$D_{(5)}$	–	–	–	–	0.01	0.01
T_3	$D_{(6)}$	–	–	–	–	0.03	0.03
T_3	$D_{(7)}$	–	–	–	–	0.03	0.03
T_3	$D_{(8)}$	–	–	–	–	0.03	0.03
T_3	$D_{(9)}$	–	–	–	–	< 0.01	< 0.01
T_3	t_G	0.03	0.03	0.05	0.05	0.03	0.03
T_3	t_T	0.05	0.04	0.07	0.07	0.04	0.04
T_4	T_5	0.04	0.03	< 0.01	< 0.01	0.02	0.01
T_4	T_6	< 0.01	< 0.01	0.01	0.01	< 0.01	< 0.01
T_4	T_7	< 0.01	0.01	< 0.01	< 0.01	< 0.01	< 0.01
T_4	T_8	< 0.01	< 0.01	< 0.01	< 0.01	< 0.01	< 0.01
T_4	T_9	0.01	0.01	< 0.01	< 0.01	< 0.01	0.01
T_4	T_{10}	< 0.01	< 0.01	0.01	< 0.01	< 0.01	< 0.01
T_4	T_{11}	0.02	0.01	< 0.01	< 0.01	< 0.01	< 0.01
T_4	$D_{(1)}$	–	–	–	–	< 0.01	< 0.01
T_4	$D_{(10)}$	–	–	–	–	0.02	0.02
T_4	$D_{(11)}$	–	–	–	–	0.03	0.03
T_4	$D_{(2)}$	–	–	–	–	< 0.01	< 0.01
T_4	$D_{(3)}$	–	–	–	–	0.03	0.03
T_4	$D_{(4)}$	–	–	–	–	0.14	0.13
T_4	$D_{(5)}$	–	–	–	–	0.01	< 0.01
T_4	$D_{(6)}$	–	–	–	–	0.03	0.03
T_4	$D_{(7)}$	–	–	–	–	0.04	0.03
T_4	$D_{(8)}$	–	–	–	–	0.04	0.04
T_4	$D_{(9)}$	–	–	–	–	< 0.01	< 0.01
T_4	t_G	0.01	0.01	0.01	< 0.01	0.03	0.03
T_4	t_T	0.05	0.04	0.01	< 0.01	0.06	0.05
T_5	T_6	< 0.01	< 0.01	< 0.01	< 0.01	0.02	0.01
T_5	T_7	0.02	0.01	< 0.01	< 0.01	0.01	0.01
T_5	T_8	< 0.01	< 0.01	< 0.01	< 0.01	0.01	0.01
T_5	T_9	< 0.01	0.01	< 0.01	< 0.01	< 0.01	< 0.01
T_5	T_{10}	< 0.01	0.01	0.01	0.01	0.02	0.02
T_5	T_{11}	0.02	< 0.01	< 0.01	< 0.01	0.01	0.01

continued on next page...

Table D.3 – Correlation Stats for TrES-3 continued from previous page

Params ↓	Chain →	FLDC		OLDC		MDFLDC	
1	2	$\lvert r\rvert$	$\lvert\rho\rvert$	$\lvert r\rvert$	$\lvert\rho\rvert$	$\lvert r\rvert$	$\lvert\rho\rvert$
T_5	$D_{(1)}$	–	–	–	–	0.04	0.04
T_5	$D_{(10)}$	–	–	–	–	< 0.01	< 0.01
T_5	$D_{(11)}$	–	–	–	–	< 0.01	< 0.01
T_5	$D_{(2)}$	–	–	–	–	0.02	0.02
T_5	$D_{(3)}$	–	–	–	–	< 0.01	< 0.01
T_5	$D_{(4)}$	–	–	–	–	< 0.01	< 0.01
T_5	$D_{(5)}$	–	–	–	–	**0.58**	**0.56**
T_5	$D_{(6)}$	–	–	–	–	< 0.01	0.01
T_5	$D_{(7)}$	–	–	–	–	< 0.01	< 0.01
T_5	$D_{(8)}$	–	–	–	–	< 0.01	< 0.01
T_5	$D_{(9)}$	–	–	–	–	< 0.01	< 0.01
T_5	t_G	< 0.01	0.01	0.06	0.06	0.02	0.02
T_5	t_T	0.08	0.08	0.05	0.05	0.03	0.03
T_6	T_7	0.01	0.01	< 0.01	< 0.01	< 0.01	< 0.01
T_6	T_8	< 0.01	< 0.01	< 0.01	< 0.01	< 0.01	< 0.01
T_6	T_9	0.04	0.03	< 0.01	< 0.01	< 0.01	< 0.01
T_6	T_{10}	0.01	0.01	< 0.01	< 0.01	< 0.01	< 0.01
T_6	T_{11}	< 0.01	< 0.01	< 0.01	< 0.01	< 0.01	< 0.01
T_6	$D_{(1)}$	–	–	–	–	0.05	0.04
T_6	$D_{(10)}$	–	–	–	–	0.04	0.04
T_6	$D_{(11)}$	–	–	–	–	0.04	0.04
T_6	$D_{(2)}$	–	–	–	–	0.03	0.03
T_6	$D_{(3)}$	–	–	–	–	0.02	0.02
T_6	$D_{(4)}$	–	–	–	–	0.04	0.04
T_6	$D_{(5)}$	–	–	–	–	0.04	0.03
T_6	$D_{(6)}$	–	–	–	–	< 0.01	< 0.01
T_6	$D_{(7)}$	–	–	–	–	0.05	0.04
T_6	$D_{(8)}$	–	–	–	–	0.03	0.03
T_6	$D_{(9)}$	–	–	–	–	0.03	0.03
T_6	t_G	0.05	0.05	0.02	0.02	0.06	0.06
T_6	t_T	< 0.01	< 0.01	0.06	0.06	0.03	0.03
T_7	T_8	< 0.01	< 0.01	< 0.01	< 0.01	< 0.01	< 0.01
T_7	T_9	< 0.01	< 0.01	< 0.01	< 0.01	< 0.01	< 0.01
T_7	T_{10}	0.03	0.03	< 0.01	< 0.01	< 0.01	< 0.01
T_7	T_{11}	< 0.01	< 0.01	< 0.01	< 0.01	< 0.01	< 0.01
T_7	$D_{(1)}$	–	–	–	–	0.01	0.01
T_7	$D_{(10)}$	–	–	–	–	0.01	0.01
T_7	$D_{(11)}$	–	–	–	–	< 0.01	< 0.01

continued on next page...

Table D.3 – Correlation Stats for TrES-3 continued from previous page

Params ↓	Chain →	FLDC		OLDC		MDFLDC	
1	2	$\lvert r\rvert$	$\lvert\rho\rvert$	$\lvert r\rvert$	$\lvert\rho\rvert$	$\lvert r\rvert$	$\lvert\rho\rvert$
T_7	$D_{(2)}$	–	–	–	–	0.01	0.01
T_7	$D_{(3)}$	–	–	–	–	< 0.01	< 0.01
T_7	$D_{(4)}$	–	–	–	–	0.01	0.01
T_7	$D_{(5)}$	–	–	–	–	0.02	0.02
T_7	$D_{(6)}$	–	–	–	–	0.02	0.02
T_7	$D_{(7)}$	–	–	–	–	0.03	0.03
T_7	$D_{(8)}$	–	–	–	–	< 0.01	< 0.01
T_7	$D_{(9)}$	–	–	–	–	< 0.01	< 0.01
T_7	t_G	< 0.01	< 0.01	0.02	0.02	< 0.01	< 0.01
T_7	t_T	< 0.01	< 0.01	0.03	0.02	< 0.01	< 0.01
T_8	T_9	0.03	0.03	< 0.01	< 0.01	0.01	0.01
T_8	T_{10}	0.02	0.02	< 0.01	< 0.01	< 0.01	< 0.01
T_8	T_{11}	< 0.01	0.02	< 0.01	< 0.01	< 0.01	< 0.01
T_8	$D_{(1)}$	–	–	–	–	< 0.01	< 0.01
T_8	$D_{(10)}$	–	–	–	–	< 0.01	0.01
T_8	$D_{(11)}$	–	–	–	–	0.01	0.01
T_8	$D_{(2)}$	–	–	–	–	< 0.01	< 0.01
T_8	$D_{(3)}$	–	–	–	–	< 0.01	< 0.01
T_8	$D_{(4)}$	–	–	–	–	< 0.01	< 0.01
T_8	$D_{(5)}$	–	–	–	–	< 0.01	< 0.01
T_8	$D_{(6)}$	–	–	–	–	< 0.01	< 0.01
T_8	$D_{(7)}$	–	–	–	–	< 0.01	< 0.01
T_8	$D_{(8)}$	–	–	–	–	0.16	0.16
T_8	$D_{(9)}$	–	–	–	–	< 0.01	< 0.01
T_8	t_G	0.03	0.02	< 0.01	< 0.01	< 0.01	< 0.01
T_8	t_T	0.04	0.04	< 0.01	0.01	< 0.01	< 0.01
T_9	T_{10}	< 0.01	< 0.01	< 0.01	< 0.01	0.02	0.02
T_9	T_{11}	0.06	0.04	< 0.01	< 0.01	< 0.01	< 0.01
T_9	$D_{(1)}$	–	–	–	–	0.02	< 0.01
T_9	$D_{(10)}$	–	–	–	–	0.01	< 0.01
T_9	$D_{(11)}$	–	–	–	–	0.01	< 0.01
T_9	$D_{(2)}$	–	–	–	–	< 0.01	< 0.01
T_9	$D_{(3)}$	–	–	–	–	< 0.01	< 0.01
T_9	$D_{(4)}$	–	–	–	–	0.02	0.01
T_9	$D_{(5)}$	–	–	–	–	< 0.01	< 0.01
T_9	$D_{(6)}$	–	–	–	–	< 0.01	0.01
T_9	$D_{(7)}$	–	–	–	–	0.01	< 0.01
T_9	$D_{(8)}$	–	–	–	–	0.02	0.02

continued on next page...

Table D.3 – Correlation Stats for TrES-3 continued from previous page

Params ↓	Chain →	FLDC		OLDC		MDFLDC	
1	2	$\|r\|$	$\|\rho\|$	$\|r\|$	$\|\rho\|$	$\|r\|$	$\|\rho\|$
T_9	$D_{(9)}$	–	–	–	–	0.13	0.12
T_9	t_G	< 0.01	< 0.01	0.06	0.05	0.02	0.01
T_9	t_T	0.02	0.01	0.06	0.05	< 0.01	< 0.01
T_{10}	T_{11}	< 0.01	< 0.01	< 0.01	< 0.01	< 0.01	< 0.01
T_{10}	$D_{(1)}$	–	–	–	–	0.01	0.01
T_{10}	$D_{(10)}$	–	–	–	–	0.05	0.05
T_{10}	$D_{(11)}$	–	–	–	–	< 0.01	< 0.01
T_{10}	$D_{(2)}$	–	–	–	–	0.02	0.02
T_{10}	$D_{(3)}$	–	–	–	–	< 0.01	< 0.01
T_{10}	$D_{(4)}$	–	–	–	–	< 0.01	< 0.01
T_{10}	$D_{(5)}$	–	–	–	–	< 0.01	< 0.01
T_{10}	$D_{(6)}$	–	–	–	–	< 0.01	< 0.01
T_{10}	$D_{(7)}$	–	–	–	–	< 0.01	< 0.01
T_{10}	$D_{(8)}$	–	–	–	–	< 0.01	< 0.01
T_{10}	$D_{(9)}$	–	–	–	–	< 0.01	< 0.01
T_{10}	t_G	0.02	0.02	< 0.01	< 0.01	< 0.01	< 0.01
T_{10}	t_T	0.02	0.01	0.03	0.03	0.02	0.02
T_{11}	$D_{(1)}$	–	–	–	–	0.02	0.02
T_{11}	$D_{(10)}$	–	–	–	–	< 0.01	0.01
T_{11}	$D_{(11)}$	–	–	–	–	0.14	0.13
T_{11}	$D_{(2)}$	–	–	–	–	< 0.01	< 0.01
T_{11}	$D_{(3)}$	–	–	–	–	< 0.01	< 0.01
T_{11}	$D_{(4)}$	–	–	–	–	< 0.01	< 0.01
T_{11}	$D_{(5)}$	–	–	–	–	0.01	0.01
T_{11}	$D_{(6)}$	–	–	–	–	0.02	0.02
T_{11}	$D_{(7)}$	–	–	–	–	0.01	0.01
T_{11}	$D_{(8)}$	–	–	–	–	< 0.01	< 0.01
T_{11}	$D_{(9)}$	–	–	–	–	< 0.01	< 0.01
T_{11}	t_G	< 0.01	< 0.01	0.03	0.03	0.02	0.02
T_{11}	t_T	0.02	0.02	0.02	0.01	< 0.01	< 0.01
$D_{(1)}$	$D_{(10)}$	–	–	–	–	0.30	0.28
$D_{(1)}$	$D_{(11)}$	–	–	–	–	0.24	0.23
$D_{(1)}$	$D_{(2)}$	–	–	–	–	0.09	0.08
$D_{(1)}$	$D_{(3)}$	–	–	–	–	0.21	0.19
$D_{(1)}$	$D_{(4)}$	–	–	–	–	0.33	0.31
$D_{(1)}$	$D_{(5)}$	–	–	–	–	0.20	0.19
$D_{(1)}$	$D_{(6)}$	–	–	–	–	0.29	0.27
$D_{(1)}$	$D_{(7)}$	–	–	–	–	0.36	0.34

continued on next page...

Table D.3 – Correlation Stats for TrES-3 continued from previous page

Params ↓	Chain →	FLDC		OLDC		MDFLDC	
1	2	$\|r\|$	$\|\rho\|$	$\|r\|$	$\|\rho\|$	$\|r\|$	$\|\rho\|$
$D_{(1)}$	$D_{(8)}$	–	–	–	–	0.30	0.28
$D_{(1)}$	$D_{(9)}$	–	–	–	–	0.17	0.16
$D_{(1)}$	t_G	–	–	–	–	0.41	0.39
$D_{(1)}$	t_T	–	–	–	–	0.34	0.32
$D_{(10)}$	$D_{(11)}$	–	–	–	–	0.47	0.45
$D_{(10)}$	$D_{(2)}$	–	–	–	–	0.12	0.11
$D_{(10)}$	$D_{(3)}$	–	–	–	–	0.44	0.41
$D_{(10)}$	$D_{(4)}$	–	–	–	–	**0.64**	**0.61**
$D_{(10)}$	$D_{(5)}$	–	–	–	–	0.34	0.33
$D_{(10)}$	$D_{(6)}$	–	–	–	–	**0.55**	**0.52**
$D_{(10)}$	$D_{(7)}$	–	–	–	–	**0.68**	**0.65**
$D_{(10)}$	$D_{(8)}$	–	–	–	–	**0.57**	**0.55**
$D_{(10)}$	$D_{(9)}$	–	–	–	–	0.27	0.24
$D_{(10)}$	t_G	–	–	–	–	**0.74**	**0.71**
$D_{(10)}$	t_T	–	–	–	–	**0.72**	**0.69**
$D_{(11)}$	$D_{(2)}$	–	–	–	–	0.10	0.09
$D_{(11)}$	$D_{(3)}$	–	–	–	–	0.39	0.36
$D_{(11)}$	$D_{(4)}$	–	–	–	–	**0.56**	**0.53**
$D_{(11)}$	$D_{(5)}$	–	–	–	–	0.30	0.28
$D_{(11)}$	$D_{(6)}$	–	–	–	–	0.46	0.44
$D_{(11)}$	$D_{(7)}$	–	–	–	–	**0.59**	**0.56**
$D_{(11)}$	$D_{(8)}$	–	–	–	–	**0.50**	0.48
$D_{(11)}$	$D_{(9)}$	–	–	–	–	0.24	0.22
$D_{(11)}$	t_G	–	–	–	–	**0.63**	**0.60**
$D_{(11)}$	t_T	–	–	–	–	**0.64**	**0.61**
$D_{(2)}$	$D_{(3)}$	–	–	–	–	0.08	0.08
$D_{(2)}$	$D_{(4)}$	–	–	–	–	0.13	0.12
$D_{(2)}$	$D_{(5)}$	–	–	–	–	0.08	0.08
$D_{(2)}$	$D_{(6)}$	–	–	–	–	0.13	0.12
$D_{(2)}$	$D_{(7)}$	–	–	–	–	0.14	0.14
$D_{(2)}$	$D_{(8)}$	–	–	–	–	0.12	0.10
$D_{(2)}$	$D_{(9)}$	–	–	–	–	0.07	0.06
$D_{(2)}$	t_G	–	–	–	–	0.17	0.16
$D_{(2)}$	t_T	–	–	–	–	0.13	0.12
$D_{(3)}$	$D_{(4)}$	–	–	–	–	**0.51**	0.49
$D_{(3)}$	$D_{(5)}$	–	–	–	–	0.27	0.26
$D_{(3)}$	$D_{(6)}$	–	–	–	–	0.42	0.40
$D_{(3)}$	$D_{(7)}$	–	–	–	–	**0.54**	**0.51**

continued on next page...

Table D.3 – Correlation Stats for TrES-3 continued from previous page

Params ↓	Chain →	FLDC		OLDC		MDFLDC	
1	2	$\|r\|$	$\|\rho\|$	$\|r\|$	$\|\rho\|$	$\|r\|$	$\|\rho\|$
$D_{(3)}$	$D_{(8)}$	–	–	–	–	0.47	0.44
$D_{(3)}$	$D_{(9)}$	–	–	–	–	0.21	0.20
$D_{(3)}$	t_G	–	–	–	–	**0.57**	**0.55**
$D_{(3)}$	t_T	–	–	–	–	**0.59**	**0.57**
$D_{(4)}$	$D_{(5)}$	–	–	–	–	0.40	0.38
$D_{(4)}$	$D_{(6)}$	–	–	–	–	**0.62**	**0.60**
$D_{(4)}$	$D_{(7)}$	–	–	–	–	**0.79**	**0.76**
$D_{(4)}$	$D_{(8)}$	–	–	–	–	**0.68**	**0.65**
$D_{(4)}$	$D_{(9)}$	–	–	–	–	0.31	0.29
$D_{(4)}$	t_G	–	–	–	–	**0.84**	**0.82**
$D_{(4)}$	t_T	–	–	–	–	**0.86**	**0.84**
$D_{(5)}$	$D_{(6)}$	–	–	–	–	0.34	0.32
$D_{(5)}$	$D_{(7)}$	–	–	–	–	0.42	0.40
$D_{(5)}$	$D_{(8)}$	–	–	–	–	0.35	0.34
$D_{(5)}$	$D_{(9)}$	–	–	–	–	0.18	0.17
$D_{(5)}$	t_G	–	–	–	–	0.47	0.45
$D_{(5)}$	t_T	–	–	–	–	0.44	0.42
$D_{(6)}$	$D_{(7)}$	–	–	–	–	**0.66**	**0.63**
$D_{(6)}$	$D_{(8)}$	–	–	–	–	**0.56**	**0.53**
$D_{(6)}$	$D_{(9)}$	–	–	–	–	0.26	0.25
$D_{(6)}$	t_G	–	–	–	–	**0.72**	**0.70**
$D_{(6)}$	t_T	–	–	–	–	**0.70**	**0.68**
$D_{(7)}$	$D_{(8)}$	–	–	–	–	**0.71**	**0.68**
$D_{(7)}$	$D_{(9)}$	–	–	–	–	0.34	0.32
$D_{(7)}$	t_G	–	–	–	–	**0.95**	**0.94**
$D_{(7)}$	t_T	–	–	–	–	**0.90**	**0.89**
$D_{(8)}$	$D_{(9)}$	–	–	–	–	0.28	0.26
$D_{(8)}$	t_G	–	–	–	–	**0.76**	**0.73**
$D_{(8)}$	t_T	–	–	–	–	**0.77**	**0.75**
$D_{(9)}$	t_G	–	–	–	–	0.37	0.35
$D_{(9)}$	t_T	–	–	–	–	0.35	0.33
t_G	t_T	**0.76**	**0.72**	**0.89**	**0.87**	**0.94**	**0.94**

D.2 Supplementary Tables: Auto-Correlation Statistics

As explained in Ch. 4, § 4.2, computing the auto-correlation of chains are a necessary post MCMC task. This section catalogs the Effective Lengths (Eff. Length) and Correlation Lengths (Corr. Lengths) of all parameters in the chains run in this study.

$$c_l = \frac{\langle \theta_j \theta_{j+l} \rangle - \langle \theta_j \rangle^2}{\langle \theta_j^2 \rangle - \langle \theta_j \rangle^2} \tag{D.1}$$

where c_l the auto-correlation function at lag l. The index j counts over the points in the ensemble. The correlation Length is defined as the lag (l), when the auto-correlation function c_l crosses 0.5. The effective length is simply the total chain length divided by the correlation length.

Table D.4: Auto Correlation Stats GJ 1214 Parameters

	FLDC		OLDC		MDFLDC	
Parameter	Corr. Length	Eff. Length	Corr. Length	Eff. Length	Corr. Length	Eff. Length
$D_{(r')}$	19	100,000	100	19,000	–	–
T_1	26	73,076	95	20,000	25	68,934
T_2	45	42,222	100	19,000	35	49,238
T_3	22	86,363	100	19,000	49	35,170
T_4	35	54,285	41	46,341	37	46,577
T_5	27	70,370	100	19,000	73	23,607
T_6	34	55,882	98	19,387	29	59,426
t_G	19	100,000	39	48,717	46	37,464
t_T	32	59,375	871	2,181	3	574,451
$v1_{(r')}$	–	–	4,969	382	–	–
$v2_{(r')}$	–	–	4,928	385	–	–
$D_{(1)}$	–	–	–	–	23	74,928
$D_{(2)}$	–	–	–	–	34	50,686
$D_{(3)}$	–	–	–	–	70	24,619
$D_{(4)}$	–	–	–	–	41	42,033
$D_{(5)}$	–	–	–	–	77	22,381
$D_{(6)}$	–	–	–	–	35	49,238

Table D.5: Auto Correlation Stats XO-2 Parameters

	FLDC		OLDC		MDFLDC	
Parameter	Corr. Length	Eff. Length	Corr. Length	Eff. Length	Corr. Length	Eff. Length
$D_{(I)}$	40	47,500	100	19,000	–	–
$D_{(r')}$	100	19,000	101	18,811	–	–
T_1	50	38,000	75	25,333	59	32,203
T_{10}	36	52,777	245	7,755	293	6,484
T_2	95	20,000	81	23,456	82	23,170
T_3	89	21,348	100	19,000	84	22,619
T_4	80	23,750	506	3,754	588	3,231
T_5	85	22,352	213	8,920	262	7,251
T_6	100	19,000	197	9,644	207	9,178
T_7	52	36,538	162	11,728	184	10,326
T_8	87	21,839	101	18,811	60	31,666
T_9	95	20,000	100	19,000	100	19,000
t_G	100	19,000	100	19,000	99	19,191
t_T	3	633,333	2,880	659	72	26,388
$v1_{(I)}$	–	–	4,907	387	–	–
$v1_{(r')}$	–	–	4,949	383	–	–
$v2_{(I)}$	–	–	4,900	387	–	–
$v2_{(r')}$	–	–	4,900	387	–	–
$D_{(1)}$	–	–	–	–	93	20,430
$D_{(10)}$	–	–	–	–	100	19,000
$D_{(2)}$	–	–	–	–	100	19,000
$D_{(3)}$	–	–	–	–	95	20,000
$D_{(4)}$	–	–	–	–	394	4,822
$D_{(5)}$	–	–	–	–	146	13,013
$D_{(6)}$	–	–	–	–	29	65,517
$D_{(7)}$	–	–	–	–	84	22,619
$D_{(8)}$	–	–	–	–	100	19,000
$D_{(9)}$	–	–	–	–	76	25,000

Table D.6: Auto Correlation Stats TrES-3 Parameters

	FLDC		OLDC		MDFLDC	
Parameter	Corr. Length	Eff. Length	Corr. Length	Eff. Length	Corr. Length	Eff. Length
$D_{(r')}$	81	23,456	1,038	1,830	–	–
T_1	84	22,619	88	21,590	100	19,000
T_{10}	90	21,111	67	28,358	82	23,170
T_{11}	107	17,757	100	19,000	100	19,000
T_2	100	19,000	100	19,000	69	27,536
T_3	318	5,974	25	76,000	61	31,147
T_4	100	19,000	89	21,348	100	19,000
T_5	100	19,000	27	70,370	100	19,000
T_6	102	18,627	35	54,285	68	27,941
T_7	59	32,203	92	20,652	100	19,000
T_8	245	7,755	100	19,000	100	19,000
T_9	100	19,000	264	7,196	301	6,312
t_G	39	48,717	4,996	380	2,866	662
t_T	29	65,517	4,901	387	2,807	676
$v1_{(r')}$	–	–	4,900	387	–	–
$v2_{(r')}$	–	–	4,939	384	–	–
$D_{(1)}$	–	–	–	–	282	6,737
$D_{(10)}$	–	–	–	–	436	4,357
$D_{(11)}$	–	–	–	–	233	8,154
$D_{(2)}$	–	–	–	–	100	19,000
$D_{(3)}$	–	–	–	–	100	19,000
$D_{(4)}$	–	–	–	–	1,724	1,102
$D_{(5)}$	–	–	–	–	100	19,000
$D_{(6)}$	–	–	–	–	390	4,871
$D_{(7)}$	–	–	–	–	2,460	772
$D_{(8)}$	–	–	–	–	896	2,120
$D_{(9)}$	–	–	–	–	538	3,531

D.3 Supplementary Tables: The Gelman-Rubin Convergence Statistic

We computed the G-R statistic using the description in Gelman & Rubin (1992). For a given parameter of interest the G-R statistic is computed using n ensemble points from m chains run from different starting locations. For each parameter (θ), we start by computing the mean of the ensembles from each chain. the variance from each ensemble, the mean of all the parameter ensembles and the square of the mean, represented as $\bar{\theta}_i$,s_i^2, $\bar{\theta}_{\rm all}$ and $\bar{\theta}_i^2$ respectively, where the index i counts over the number of chains (m). We then compute the variance between the means of each chain B/n,

$$\frac{B}{n} = \sum_{i=1}^{m} (\bar{\theta} - \bar{\theta}_{\rm all})^2/(m-1) \tag{D.2a}$$

the within-sequence average of the variances W,

$$W = \sum_{i=1}^{m} s_i^2/m \tag{D.2b}$$

and the target variance $\hat{\sigma}^2$,

$$\hat{\sigma}^2 = \frac{n-1}{n} W + \frac{1}{n} B \tag{D.2c}$$

The variance estimate of the ensemble is then given by,

$$\hat{V} = \hat{\sigma}^2 + B/mn \tag{D.2d}$$

and the degrees of freedom,

$$df = 2\frac{\hat{V}^2}{\hat{\rm var}(\hat{V})} \tag{D.2e}$$

where

$$\begin{aligned}
\hat{\rm var}(\hat{V}) \;\; = \;\; & \left(\frac{n-1}{n}\right)^2 \frac{1}{m} \hat{\rm var}(s_i^2) + & \text{(D.2f)} \\
& \left(\frac{m+1}{m}\right)^2 \frac{2}{m-1} B^2 + & \text{(D.2g)} \\
& 2\frac{(m+1)(n-1)}{mn^2} \times & \text{(D.2h)} \\
& \frac{n}{m} \left[\hat{\rm cov}(s_i^2, \bar{\theta}_i^2) - 2\bar{\theta}_{\rm all} \hat{\rm cov}(s_i^2, \bar{\theta}_i)\right] & \text{(D.2i)}
\end{aligned}$$

The G-R statistic $\hat{R}$ is then given by,

$$\hat{R} = \frac{\hat{V}}{W}\frac{df}{df-2} \tag{D.2j}$$

which should approach 1 as $n \to \infty$ for converged chains. The remainder of this chapter lists the G-R statistic for all chains run for this study.

Table D.7: Gelman-Rubin Statistic for GJ 1214 Chains

Parameter	FLDC	OLDC	MDFLDC
$D_{(r')}$	1.000	1.000	–
T_1	1.000	1.000	1.000
T_2	1.000	1.000	1.000
T_3	1.000	1.000	1.000
T_4	1.000	1.000	1.000
T_5	1.000	1.000	1.000
T_6	1.000	1.000	1.000
t_G	1.000	1.000	1.000
t_T	1.000	1.000	1.000
$v1_{(r')}$	–	1.000	–
$v2_{(r')}$	–	1.001	–
$D_{(1)}$	–	–	1.000
$D_{(2)}$	–	–	1.000
$D_{(3)}$	–	–	1.000
$D_{(4)}$	–	–	1.000
$D_{(5)}$	–	–	1.000
$D_{(6)}$	–	–	1.000

Table D.8: Gelman-Rubin Statistic for XO-2 Chains

Parameter	FLDC	OLDC	MDFLDC
$D_{(I)}$	1.000	1.013	–
$D_{(r')}$	1.000	1.000	–
T_1	1.000	1.000	1.000
T_{10}	1.000	1.000	1.000
T_2	1.001	1.000	1.000
T_3	1.000	1.000	1.000
T_4	1.000	1.000	1.000
T_5	1.000	1.000	1.001
T_6	1.002	1.000	1.001
T_7	1.000	1.000	1.000
T_8	1.001	1.000	1.000
T_9	1.000	1.000	1.000
t_G	1.000	1.008	1.000
t_T	1.000	1.029	1.001
$v1_{(I)}$	–	1.059	–
$v1_{(r')}$	–	1.017	–
$v2_{(I)}$	–	1.085	–
$v2_{(r')}$	–	1.009	–
$D_{(1)}$	–	–	1.000
$D_{(10)}$	–	–	1.000
$D_{(2)}$	–	–	1.000
$D_{(3)}$	–	–	1.000
$D_{(4)}$	–	–	1.001
$D_{(5)}$	–	–	1.001
$D_{(6)}$	–	–	1.000
$D_{(7)}$	–	–	1.000
$D_{(8)}$	–	–	1.000
$D_{(9)}$	–	–	1.000

Table D.9: Gelman-Rubin Statistic for TrES-3 Chains

Parameter	FLDC	OLDC	MDFLDC
$D_{(r')}$	1.000	1.001	–
T_1	1.001	1.000	1.000
T_{10}	1.000	1.000	1.000
T_{11}	1.000	1.000	1.000
T_2	1.000	1.000	1.000
T_3	1.000	1.000	1.000
T_4	1.000	1.000	1.000
T_5	1.000	1.000	1.000
T_6	1.000	1.000	1.000
T_7	1.000	1.000	1.000
T_8	1.000	1.000	1.000
T_9	1.000	1.000	1.000
t_G	1.000	1.000	1.002
t_T	1.000	1.000	1.002
$v1_{(r')}$	–	1.000	–
$v2_{(r')}$	–	1.014	–
$D_{(1)}$	–	–	1.000
$D_{(10)}$	–	–	1.000
$D_{(11)}$	–	–	1.003
$D_{(2)}$	–	–	1.000
$D_{(3)}$	–	–	1.001
$D_{(4)}$	–	–	1.002
$D_{(5)}$	–	–	1.000
$D_{(6)}$	–	–	1.001
$D_{(7)}$	–	–	1.002
$D_{(8)}$	–	–	1.002
$D_{(9)}$	–	–	1.000

Appendix E

Tables of Transit Times for GJ 1214b, XO-2b and TrES-3b

The following tables list all the transit times used in this dissertation. The values are drawn from the literature and the analysis of APOSTLE data.

Table E.1: Transit Times for GJ 1214

Epoch	T0 (2,400,000+)	σ_{T0}	Reference
217	55307.8926553	0.0000715	APOSTLE (TMCMC)
246	55353.7244015	0.0000876	APOSTLE (TMCMC)
265	55383.7522361	0.0000979	APOSTLE (TMCMC)
470	55707.7349807	0.0000878	APOSTLE (TMCMC)
489	55737.7625878	0.0000895	APOSTLE (TMCMC)
513	55775.6925407	0.0001012	APOSTLE (TMCMC)
217	55307.8927000	0.0001400	APOSTLE (TAP)
246	55353.7244100	0.0001300	APOSTLE (TAP)
265	55383.7522020	0.0000960	APOSTLE (TAP)
470	55707.7350300	0.0002100	APOSTLE (TAP)
489	55737.7626200	0.0001200	APOSTLE (TAP)
513	55775.6925500	0.0001800	APOSTLE (TAP)
0	54964.9442080	0.0004030	Charbonneau et al. (2009)
10	54980.7479702	0.0000903	Charbonneau et al. (2009)
12	54983.9087558	0.0000901	Charbonneau et al. (2009)
22	54999.7127030	0.0001260	Charbonneau et al. (2009)
222	55315.7941900	0.0004200	Sada et al. (2010)

continued on next page...

Table E.1 – Transit Times for GJ 1214 continued from previous page

Epoch	T0 (2,400,000+)	σ_{T0}	Reference
241	55345.8220200	0.0001400	Sada et al. (2010)
241	55345.8220900	0.0003700	Sada et al. (2010)
246	55353.7240800	0.0003600	Sada et al. (2010)
253	55364.7874500	0.0002900	Sada et al. (2010)
10	54980.7485700	0.0001500	Carter et al. (2011)
12	54983.9098200	0.0001600	Carter et al. (2011)
15	54988.6508080	0.0000490	Carter et al. (2011)
24	55002.8746700	0.0001900	Carter et al. (2011)
193	55269.9629900	0.0001600	Carter et al. (2011)
210	55296.8301300	0.0002300	Carter et al. (2011)
222	55315.7946930	0.0000800	Carter et al. (2011)
222	55315.7948500	0.0002300	Carter et al. (2011)
224	55318.9552300	0.0001700	Carter et al. (2011)
246	55353.7238700	0.0001800	Carter et al. (2011)
248	55356.8849500	0.0001500	Carter et al. (2011)
253	55364.7870000	0.0001500	Carter et al. (2011)
260	55375.8499700	0.0001300	Carter et al. (2011)
265	55383.7520500	0.0001300	Carter et al. (2011)
270	55391.6541050	0.0005900	Carter et al. (2011)
0	54964.9447790	0.0007990	Kundurthy et al. (2011)
10	54980.7487210	0.0002630	Kundurthy et al. (2011)
10	54980.7487400	0.0003900	Kundurthy et al. (2011)
12	54983.9095520	0.0003810	Kundurthy et al. (2011)
12	54983.9094900	0.0002280	Kundurthy et al. (2011)
22	54999.7134420	0.0002530	Kundurthy et al. (2011)
217	55307.8924540	0.0002710	Kundurthy et al. (2011)

continued on next page...

Table E.1 – Transit Times for GJ 1214 continued from previous page

Epoch	T0 (2,400,000+)	σ_{T0}	Reference
246	55353.7245390	0.0003070	Kundurthy et al. (2011)
265	55383.7521430	0.0002600	Kundurthy et al. (2011)
1	54966.5252070	0.0003510	Berta et al. (2011)
10	54980.7486820	0.0001040	Berta et al. (2011)
12	54983.9095070	0.0000900	Berta et al. (2011)
22	54999.7134480	0.0001550	Berta et al. (2011)
222	55315.7945640	0.0000660	Berta et al. (2011)
229	55326.8574040	0.0001100	Berta et al. (2011)
234	55334.7593340	0.0000660	Berta et al. (2011)
465	55699.8328660	0.0000690	Bean et al. (2011)
494	55745.6647290	0.0000600	Bean et al. (2011)
518	55783.5944000	0.0001100	Bean et al. (2011)
260	55375.8501000	0.0001000	Croll et al. (2011)
286	55416.9402000	0.0004000	Croll et al. (2011)
286	55416.9404000	0.0001000	Croll et al. (2011)
291	55424.8423000	0.0001000	Croll et al. (2011)
315	55462.7722000	0.0001000	Croll et al. (2011)
220	55312.6330850	0.0000800	Désert et al. (2011)
221	55314.2134400	0.0000930	Désert et al. (2011)
239	55342.6613300	0.0002300	de Mooij et al. (2012)
239	55342.6615700	0.0002900	de Mooij et al. (2012)
263	55380.5908900	0.0001700	de Mooij et al. (2012)
263	55380.5912100	0.0001900	de Mooij et al. (2012)
263	55380.5912000	0.0002200	de Mooij et al. (2012)
263	55380.5912500	0.0004000	de Mooij et al. (2012)
280	55407.4583000	0.0000700	de Mooij et al. (2012)

continued on next page...

Table E.1 – Transit Times for GJ 1214 continued from previous page

Epoch	T0 (2,400,000+)	σ_{T0}	Reference
292	55426.4235000	0.0003200	de Mooij et al. (2012)
433	55649.2602809	0.0003100	Berta et al. (2012)
507	55766.2101569	0.0004000	Berta et al. (2012)

Table E.2: Transit Times for XO-2

Epoch	T0 (2,400,000+)	σ_{T0}	Reference
3	54474.7324165	0.0001138	APOSTLE (TMCMC)
16	54508.7387480	0.0001293	APOSTLE (TMCMC)
24	54529.6659623	0.0000900	APOSTLE (TMCMC)
125	54793.8684527	0.0002433	APOSTLE (TMCMC)
154	54869.7275307	0.0002348	APOSTLE (TMCMC)
167	54903.7339748	0.0001352	APOSTLE (TMCMC)
393	55494.9179555	0.0001503	APOSTLE (TMCMC)
417	55557.6989124	0.0002012	APOSTLE (TMCMC)
430	55591.7050679	0.0000800	APOSTLE (TMCMC)
443	55625.7109263	0.0001392	APOSTLE (TMCMC)
3	54474.7325200	0.0002100	APOSTLE (TAP)
16	54508.7387700	0.0002000	APOSTLE (TAP)
24	54529.6660400	0.0001600	APOSTLE (TAP)
125	54793.8683600	0.0004100	APOSTLE (TAP)
154	54869.7273500	0.0005000	APOSTLE (TAP)
167	54903.7340300	0.0002000	APOSTLE (TAP)
393	55494.9179400	0.0002100	APOSTLE (TAP)
417	55557.6989200	0.0002500	APOSTLE (TAP)

continued on next page...

Table E.2 – Transit Times for XO-2 continued from previous page

Epoch	T0 (2,400,000+)	σ_{T0}	Reference
430	55591.7051100	0.0001500	APOSTLE (TAP)
443	55625.7111200	0.0001900	APOSTLE (TAP)
0	54466.8859000	0.0002100	Fernandez et al. (2009)
5	54479.9647100	0.0003900	Fernandez et al. (2009)
16	54508.7394200	0.0002600	Fernandez et al. (2009)
21	54521.8185600	0.0007200	Fernandez et al. (2009)
24	54529.6651100	0.0004300	Fernandez et al. (2009)
25	54532.2805600	0.0007400	Fernandez et al. (2009)
261	55149.6252900	0.0002700	Sing et al. (2011)
269	55170.5526000	0.0002300	Sing et al. (2011)
269	55170.5521900	0.0002300	Sing et al. (2011)
303	55259.4905600	0.0003000	Sing et al. (2011)

Table E.3: Transit Times for TrES-3

Epoch	T0 (2,400,000+)	σ_{T0}	Reference
597	54965.7046437	0.0001079	APOSTLE (TMCMC)
620	54995.7465390	0.0001326	APOSTLE (TMCMC)
836	55277.8821699	0.0002456	APOSTLE (TMCMC)
878	55332.7425269	0.0001033	APOSTLE (TMCMC)
891	55349.7228375	0.0003216	APOSTLE (TMCMC)
992	55481.6479691	0.0001589	APOSTLE (TMCMC)
1117	55644.9210892	0.0000699	APOSTLE (TMCMC)
1143	55678.8828740	0.0001637	APOSTLE (TMCMC)
1156	55695.8623990	0.0003861	APOSTLE (TMCMC)

continued on next page...

Table E.3 – Transit Times for TrES-3 continued from previous page

Epoch	T0 (2,400,000+)	σ_{T0}	Reference
1185	55733.7414753	0.0001397	APOSTLE (TMCMC)
1234	55797.7456860	0.0001699	APOSTLE (TMCMC)
597	54965.7046300	0.0002000	APOSTLE (TAP)
620	54995.7465900	0.0001400	APOSTLE (TAP)
836	55277.8822500	0.0003600	APOSTLE (TAP)
878	55332.7426300	0.0002700	APOSTLE (TAP)
891	55349.7230400	0.0003800	APOSTLE (TAP)
992	55481.6479900	0.0001600	APOSTLE (TAP)
1117	55644.9211900	0.0001800	APOSTLE (TAP)
1143	55678.8825200	0.0003000	APOSTLE (TAP)
1156	55695.8623500	0.0006600	APOSTLE (TAP)
1185	55733.7417000	0.0003300	APOSTLE (TAP)
1234	55797.7456600	0.0002900	APOSTLE (TAP)
0	54185.9111700	0.0002000	Sozetti et al. (2009)
10	54198.9738900	0.0002200	Sozetti et al. (2009)
22	54214.6470400	0.0002800	Sozetti et al. (2009)
23	54215.9528200	0.0002100	Sozetti et al. (2009)
268	54535.9689900	0.0001700	Sozetti et al. (2009)
281	54552.9497100	0.0001500	Sozetti et al. (2009)
294	54569.9298300	0.0001500	Sozetti et al. (2009)
313	54594.7466800	0.0002500	Sozetti et al. (2009)
0	54185.9111400	0.0002800	Gibson et al. (2009)
10	54198.9738100	0.0003300	Gibson et al. (2009)
22	54214.6470500	0.0003600	Gibson et al. (2009)
23	54215.9528400	0.0002400	Gibson et al. (2009)
267	54534.6631700	0.0001700	Gibson et al. (2009)

continued on next page...

Table E.3 – Transit Times for TrES-3 continued from previous page

Epoch	T0 (2,400,000+)	σ_{T0}	Reference
268	54535.9689900	0.0002300	Gibson et al. (2009)
281	54552.9497200	0.0002100	Gibson et al. (2009)
294	54569.9298400	0.0002100	Gibson et al. (2009)
313	54594.7467100	0.0002800	Gibson et al. (2009)
329	54615.6462700	0.0001700	Gibson et al. (2009)
342	54632.6268700	0.0001100	Gibson et al. (2009)
355	54649.6070800	0.0001300	Gibson et al. (2009)
358	54653.5257800	0.0003700	Gibson et al. (2009)
365	54662.6697000	0.0003400	Gibson et al. (2009)
371	54670.5070400	0.0003300	Gibson et al. (2009)
374	54674.4249700	0.0005200	Gibson et al. (2009)
381	54683.5680800	0.0001800	Gibson et al. (2009)
265	54532.0493900	0.0003300	Christiansen et al. (2011)
266	54533.3551500	0.0003500	Christiansen et al. (2011)
269	54537.2746300	0.0003800	Christiansen et al. (2011)
270	54538.5812600	0.0003500	Christiansen et al. (2011)
271	54539.8870300	0.0004000	Christiansen et al. (2011)
272	54541.1926100	0.0003500	Christiansen et al. (2011)
273	54542.4993000	0.0004100	Christiansen et al. (2011)

Appendix F

Used Nuisance Parameters

The following tables list the set of Nuisance parameters used to detrend each lightcurve. See Ch. 2 Table 2.3 for definitions.

Table F.1: Nuisance Parameters used for GJ 1214 Chains

T#	Nuisance Parameters used (FLDC, OLDC and MDFLDC)
T1	airmass, msky1, msky2, gsky, x1, y1, x2, y2, sD1, sD2, sF1, sF2, a0
T2	airmass, msky1, msky2, gsky, x1, y1, x2, y2, sD1, sD2, sF1, sF2, a0
T3	airmass, msky1, msky2, gsky, x1, y1, x2, y2, sD1, sD2, sF1, sF2, a0
T4	airmass, msky1, msky2, gsky, x1, y1, x2, y2, sD1, sD2, sF1, sF2, a0
T5	airmass, msky1, msky2, gsky, x1, y1, x2, y2, sD1, sD2, sF1, sF2, a0
T6	airmass, msky1, msky2, gsky, x1, y1, x2, y2, sD1, sD2, sF1, sF2, a0

Table F.2: Nuisance Parameters used for XO-2 Chains

T#	Nuisance Parameters used (FLDC, OLDC and MDFLDC)
T1	airmass, msky1, msky2, gsky, x1, y1, x2, y2, sD1, sD2, sF1, sF2, a0
T2	airmass, msky1, msky2, gsky, x1, y1, x2, y2, sD1, sD2, sF1, sF2, a0
T3	airmass, msky1, msky2, gsky, x1, y1, x2, y2, sD1, sD2, sF1, sF2, a0
T4	airmass, msky1, msky2, gsky, x1, y1, x2, y2, sD1, sD2, sF1, sF2, a0
T5	airmass, x1, y1, sD1, sF1, a0
T6	airmass, x1, y1, sD1, sF1, a0
T7	airmass, gsky, x1, y1, sD1, sF1
T8	airmass, gsky, x1, y1, sD1, sF1
T9	airmass, gsky, x1, y1, sD1, sF1
T10	airmass, gsky, x1, y1, sD1, sF1

Table F.3: Nuisance Parameters used for TrES-3 Chains

T#	Nuisance Parameters used (FLDC, OLDC and MDFLDC)
T1	airmass, gsky, x1, y1, sD1, sF1
T2	airmass, gsky, x1, y1, sD1, sF1
T3	airmass, gsky, x1, y1, sD1, sF1
T4	airmass, gsky, x1, y1, sD1, sF1
T5	airmass, gsky, x1, y1, sD1, sF1
T6	airmass, gsky, x1, y1, sD1, sF1
T7	airmass, gsky, x1, y1, sD1, sF1
T8	airmass, gsky, x1, y1, sD1, sF1
T9	airmass, gsky, x1, y1, sD1, sF1
T10	airmass, gsky, x1, y1, sD1, sF1
T11	airmass, gsky, x1, y1, sD1, sF1

BIBLIOGRAPHY

Adams, E. R., López-Morales, M., Elliot, J. L., Seager, S., & Osip, D. J. 2010, ApJ, 721, 1829

Adams, E. R., López-Morales, M., Elliot, J. L., et al. 2011, ApJ, 741, 102

Agol, E., Steffen, J., Sari, R., & Clarkson, W. 2005, MNRAS, 359, 567

Agol, E., & Steffen, J. H. 2007, MNRAS, 374, 941

Albrecht, S., Winn, J. N., Johnson, J. A., et al. 2012, arXiv:1206.6105

Bakos, G. Á., Noyes, R. W., Kovács, G., et al. 2009, IAU Symposium, 253, 21

Ballard, S., Christiansen, J. L., Charbonneau, D., et al. 2010, ApJ, 716, 1047

Ballard, S., Fabrycky, D., Fressin, F., et al. 2011, ApJ, 743, 200

Barnes, J. W., & Fortney, J. J. 2004, ApJ, 616, 1193

Basri, G., Walkowicz, L. M., Batalha, N., et al. 2011, AJ, 141, 20

Batalha, N. M., Borucki, W. J., Bryson, S. T., et al. 2011, ApJ, 729, 27

Batalha, N. M., Rowe, J. F., Bryson, S. T., et al. 2012, arXiv:1202.5852

Bayless, A. J., & Orosz, J. A. 2006, ApJ, 651, 1155

Bean, J. L. 2009, A&A, 506, 369

Bean, J. L., Miller-Ricci Kempton, E., & Homeier, D. 2010, Nature, 468, 669

Bean, J. L., Désert, J.-M., Kabath, P., et al. 2011, ApJ, 743, 92

Becker, A. C. et al. in prep

Berdyugina, S. V. 2005, Living Reviews in Solar Physics, 2, 8

Berta, Z. K., Charbonneau, D., Bean, J., et al. 2011, ApJ, 736, 12

Berta, Z. K., Charbonneau, D., Désert, J.-M., et al. 2012, ApJ, 747, 35

Bertin, E., & Arnouts, S. 1996, A&AS, 117, 393

Bessell, M. S. 1990, PASP, 102, 1181

Borucki, W. J., Koch, D., Basri, G., et al. 2010, Science, 327, 977

Borucki, W. J., Koch, D. G., Basri, G., et al. 2011, ApJ, 728, 117

Borucki, W. J., Koch, D. G., Basri, G., et al. 2011, ApJ, 736, 19

Borucki, W. J., Koch, D. G., Batalha, N., et al. 2011, arXiv:1112.1640

Boumis, P., Pollacco, D., Steele, I., et al. 2010, 9th International Conference of the Hellenic Astronomical Society, 424, 426

Brown, T. M., Charbonneau, D., Gilliland, R. L., Noyes, R. W., & Burrows, A. 2001, ApJ, 552, 699

Burke, C. J., McCullough, P. R., Valenti, J. A., et al. 2007, ApJ, 671, 2115

Burrows, A., Hubeny, I., Budaj, J., Knutson, H. A., & Charbonneau, D. 2007, ApJ, 668, L171

Carter, J. A., Yee, J. C., Eastman, J., Gaudi, B. S., & Winn, J. N. 2008, ApJ, 689, 499

Carter, J. A., & Winn, J. N. 2009, ApJ, 704, 51

Carter, J. A., & Winn, J. N. 2010, ApJ, 716, 850

Carter, J. A., Winn, J. N., Holman, M. J., et al. 2011, ApJ, 730, 82

Chabrier, G., Gallardo, J., & Baraffe, I. 2007, A&A, 472, L17

Charbonneau, D., Brown, T. M., Latham, D. W., & Mayor, M. 2000, ApJ, 529, L45

Charbonneau, D., et al. 2009, Nature, 462, 891

Christiansen, J. L., Ballard, S., Charbonneau, D., et al. 2011, ApJ, 726, 94

Claret, A., & Bloemen, S. 2011, A&A, 529, A75

Croll, B., Albert, L., Jayawardhana, R., et al. 2011, ApJ, 736, 78

Crossfield, I. J. M., Barman, T., & Hansen, B. M. S. 2011, ApJ, 736, 132

Cochran, W. D., Fabrycky, D. C., Torres, G., et al. 2011, ApJS, 197, 7

Collier Cameron, A., Bouchy, F., Hébrard, G., et al. 2007, MNRAS, 375, 951

Collier Cameron, A., et al. 2007, MNRAS, 380, 1230

Cousins, A. W. J. 1976, Monthly Notes of the Astronomical Society of South Africa, 35, 70

Demory, B.-O., et al. 2009, A&A, 505, 205

Demory, B.-O., Gillon, M., Deming, D., et al. 2011,A&A, 533, A114

Désert, J.-M., Bean, J., Miller-Ricci Kempton, E., et al. 2011, ApJ, 731, L40

Désert, J.-M., Charbonneau, D., Demory, B.-O., et al. 2011, ApJS, 197, 14

Díaz, R. F., Rojo, P., Melita, M., et al. 2008, ApJ, 682, L49

Dittmann, J. A., Close, L. M., Green, E. M., & Fenwick, M. 2009, ApJ, 701, 756

Eastman, J., Siverd, R., & Gaudi, B. S. 2010, PASP, 122, 935

Eastman, J., Gaudi, B. S., & Agol, E. 2012, arXiv:1206.5798

Edwards, R. T., Hobbs, G. B., & Manchester, R. N. 2006, MNRAS, 372, 1549

Fabrycky, D., & Tremaine, S. 2007, ApJ, 669, 1298

Faedi, F., Barros, S. C. C., Anderson, D. R., et al. 2011, A&A, 531, A40

Fairhead, et al., 1988, IAUS, 128, 419

Fairhead, L. & P. Bertangnon, 1990, A&A, 229, 240

Fernandez, J. M., Holman, M. J., Winn, J. N., et al. 2009, AJ, 137, 4911

Fressin, F., Knutson, H. A., Charbonneau, D., et al. 2010, ApJ, 711, 374

Fressin, F., Torres, G., Rowe, J. F., et al. 2011, arXiv:1112.4550

Fridlund, M. et al. 2006, Noordwijk, The Netherlands, ESA SP-1306

Ford, E. B. 2005, AJ, 129, 1706

Ford, E. B., & Gaudi, B. S. 2006, ApJ, 652, L137

Fortney, J. J., Lodders, K., Marley, M. S., & Freedman, R. S. 2008, ApJ, 678, 1419

Fukugita, M., Ichikawa, T., Gunn, J. E., Doi, M., Shimasaku, K.,& Scheider, D. p. 1996, AJ, 111, 1748

Fukui, A., Narita, N., Tristram, P. J., et al. 2011, PASJ, 63, 287

Fulton, B. J., Shporer, A., Winn, J. N., et al. 2011, AJ, 142, 84

Gazak, J. Z., Johnson, J. A., Tonry, J., et al. 2011, arXiv:1102.1036

Gautier, T. N., III, Charbonneau, D., Rowe, J. F., et al. 2012, ApJ, 749, 15

Gelman, A. & D. B. Rubin, 1992, Statistical Science, 7, 457

Gelman, A. et al. 2003, Bayesian Data Analysis (2nd ed.; Boca Raton: Chapman & Hall/CRC)

Gibson, N. P., Pollacco, D., Simpson, E. K., et al. 2009, ApJ, 700, 1078

Gomes, R., Levison, H. F., Tsiganis, K., & Morbidelli, A. 2005, Nature, 435, 466

Harada, W. & T. Fukushima, 2003, AJ, 126, 2557

Hauschildt, P. H., Allard, F., & Baron, E. 1999, ApJ, 512, 377

Hawley, S. L., & Pettersen, B. R. 1991, ApJ, 378, 725

Hawley, S. L., Gizis, J. E., & Reid, I. N. 1996, AJ, 112, 2799

Hawley, S. L., et al. 2003, ApJ, 597, 535

Henry, G. W., Howard, A. W., Marcy, G. W., Fischer, D. A., & Johnson, J. A. 2011, arXiv:1109.2549

Hobbs, G. B., et al., 2006, MNRAS, 369, 655

Holman, M. J., & Murray, N. W. 2005, Science, 307, 1288

Holman, M. J., & Winn, J. N. 2006, Bulletin of the American Astronomical Society, 38, 482

Holman, M. J., et al. 2006, ApJ, 652, 1715

Holman, M. J., Fabrycky, D. C., Ragozzine, D., et al. 2010, Science, 330, 51

Howard, A. W., Johnson, J. A., Marcy, G. W., et al. 2011, ApJ, 730, 10

Howard, A. W., Bakos, G. Á., Hartman, J., et al. 2012, ApJ, 749, 134

Hubeny, I., Burrows, A., & Sudarsky, D. 2003, ApJ, 594, 1011

Ikoma, M., Emori, H., & Nakazawa, K. 2001, ApJ, 553, 999

Ivezić, Ž., Smith, J. A., Miknaitis, G., et al. 2007, AJ, 134, 973

Kaplan, G., H., 2005, USNO Circular, 179, The IAU Resolution on Astronomical Reference Systems, Time Scales and Earth Rotation Models: Explanation and Implementation

Kane, S. R., Horne, K., Street, R. A., et al. 2003, Scientific Frontiers in Research on Extrasolar Planets, 294, 387

Knutson, H. A., Charbonneau, D., Noyes, R. W., Brown, T. M., & Gilliland, R. L. 2007, ApJ, 655, 564

Knutson, H. A., Howard, A. W., & Isaacson, H. 2010, ApJ, 720, 1569

Knutson, H. A., Madhusudhan, N., Cowan, N. B., et al. 2011, ApJ, 735, 27

Kowalski, A. F., Hawley, S. L., Holtzman, J. A., Wisniewski, J. P., & Hilton, E. J. 2010, ApJ, 714, L98

Kundurthy, P., Agol, E., Becker, A. C., et al. 2011, ApJ, 731, 123

Latham, D. W., Rowe, J. F., Quinn, S. N., et al. 2011, ApJ, 732, L24

Lanza, A. F., Pagano, I., Leto, G., et al. 2009, A&A, 493, 193

Lanza, A. F., Bonomo, A. S., Moutou, C., et al. 2010, A&A, 520, A53

Lanza, A. F., Bonomo, A. S., Pagano, I., et al. 2011, A&A, 525, A14

Léger, A., Rouan, D., Schneider, J., et al. 2009, A&A, 506, 287

Lin, D. N. C., Bodenheimer, P., & Richardson, D. C. 1996, Nature, 380, 606

Lissauer, J. J., Hubickyj, O., D'Angelo, G., & Bodenheimer, P. 2009, *Icarus*, 199, 338

Lissauer, J. J., Fabrycky, D. C., Ford, E. B., et al. 2011, Nature, 470, 53

Lissauer, J. J., Ragozzine, D., Fabrycky, D. C., et al. 2011, ApJS, 197, 8

Machalek, P., McCullough, P. R., Burrows, A., et al. 2009, ApJ, 701, 514

Maciejewski, G., Dimitrov, D., Neuhäuser, R., et al. 2010, MNRAS, 407, 2625

Maciejewski, G., Raetz, S., Nettelmann, N., et al. 2011, A&A, 535, A7

Maíz Apellániz, J. 2006, AJ, 131, 1184

Mandel, K., & Agol, E. 2002, ApJ, 580, L171

Markwardt, C. B., http://www.physics.wisc.edu/ craigm/idl/, Last Modified on 2011-12-21 20:14:43 by Craig Markwardt

Masset, F. S., & Papaloizou, J. C. B. 2003, ApJ, 588, 494

Mayor, M., & Queloz, D. 1995, Nature, 378, 355

McArthur, B. E., Endl, M., Cochran, W. D., et al. 2004, ApJ, 614, L81

McCullough, P. R., Stys, J. E., Valenti, J. A., et al. 2005, PASP, 117, 783

Miller-Ricci, E., Rowe, J. F., Sasselov, D., et al. 2008, ApJ, 682, 593

Miller-Ricci, E., Rowe, J. F., Sasselov, D., et al. 2008, ApJ, 682, 586

de Mooij, E. J. W., & Snellen, I. A. G. 2009, A&A, 493, L35

de Mooij, E. J. W., Brogi, M., de Kok, R. J., et al. 2012, A&A, 538, A46

Morales, J. C., Gallardo, J., Ribas, I., Jordi, C., Baraffe, I., & Chabrier, G. 2010, ApJ, 718, 502

Monet, D. G., Levine, S. E., Canzian, B., et al. 2003, AJ, 125, 984

Montes, D., López-Santiago, J., Gálvez, M. C., Fernández-Figueroa, M. J., De Castro, E., & Cornide, M. 2001, MNRAS, 328, 45

Mukadam, A. S., Owen, R., Mannery, E., et al. 2011, PASP, 123, 1423

Nascimbeni, V., Piotto, G., Bedin, L. R., & Damasso, M. 2011, A&A, 527, A85

Nascimbeni, V., Piotto, G., Bedin, L. R., et al. 2011, A&A, 532, A24

Nesvorný, D., Kipping, D. M., Buchhave, L. A., et al. 2012, Science, 336, 1133

Nettelmann, N., Fortney, J. J., Kramm, U., & Redmer, R. 2011, ApJ, 733, 2

O'Donovan, F. T., Charbonneau, D., Bakos, G. Á., et al. 2007, ApJ, 663, L37

Pál, A., Sárneczky, K., Szabó, G. M., et al. 2011, MNRAS, 413, L43

Pollacco, D. L., Skillen, I., Collier Cameron, A., et al. 2006, PASP, 118, 1407

Pollack, J. B., Hubickyj, O., Bodenheimer, P., et al. 1996, *Icarus*, 124, 62

Pont, F., Gilliland, R. L., Moutou, C., et al. 2007, A&A, 476, 1347

Queloz, D., Bouchy, F., Moutou, C., et al. 2009, A&A, 506, 303

Rabus, M., Alonso, R., Belmonte, J. A., et al. 2009, A&A, 494, 391

Rasio, F. A., & Ford, E. B. 1996, Science, 274, 954

Rhodes, B. C., http://rhodesmill.org/pyephem/reference.html, Last updated on Mar 16, 2012. Created using Sphinx 1.1.3.

Reiners, A., & Basri, G. 2009, A&A, 496, 787

Rogers, L. A., & Seager, S. 2010, ApJ, 716, 1208

Sada, P. V., Deming, D., Jackson, B., et al. 2010, ApJ, 720, L215

Sahu, K. C., Casertano, S., Bond, H. E., et al. 2006, Nature, 443, 534

Sartoretti, P., & Schneider, J. 1999, A&AS, 134, 553

Seager, S., & Mallén-Ornelas, G. 2003, ApJ, 585, 1038

Seager, S., Kuchner, M., Hier-Majumder, C. A., & Militzer, B. 2007, ApJ, 669, 1279

Seidelmann, P. K. & T. Fukushima, 1992, A&A, 265, 833

Silva, A. V. R. 2003, ApJ, 585, L147

Silva-Valio, A. 2008, ApJ, 683, L179

Sing, D. K., Désert, J.-M., Fortney, J. J., et al. 2011, A&A, 527, A73

Southworth, J. 2010, MNRAS, 408, 1689

Sozzetti, A., Torres, G., Charbonneau, D., et al. 2009, ApJ, 691, 1145

Standish, E. M., 1998, A&A, 336, 381

Stankov, A., Martin, D., Schulz, R., et al. 2007, Transiting Extrapolar Planets Workshop, 366, 268

Steele, I. A., Bates, S. D., Gibson, N., et al. 2008, Proc. SPIE, 7014,

Steffen, J. H., & Agol, E. 2005, MNRAS, 364, L96

Steffen, J. H., Ragozzine, D., Fabrycky, D. C., et al. 2012, arXiv:1205.2309

Street, R. A., Pollaco, D. L., Fitzsimmons, A., et al. 2003, Scientific Frontiers in Research on Extrasolar Planets, 294, 405

Szymański, M., Udalski, A., Kubiak, M., et al. 2001, Dynamics of Star Clusters and the Milky Way, 228, 277

Tegmark, M., et al. 2004, Phys. Rev. D, 69, 103501

Tingley, B., Thurl, C., & Sackett, P. 2006, A&A, 445, L27

Torres, G., Winn, J. N., & Holman, M. J. 2008, ApJ, 677, 1324

Tsiganis, K., Gomes, R., Morbidelli, A., & Levison, H. F. 2005, Nature, 435, 459

Tufts, J. R., Lobdill, R., Haldeman, B. J., et al. 2008, Proc. SPIE, 7021

Tusnski, L. R. M., & Valio, A. 2011, ApJ, 743, 97

Walkowicz, L. M., Basri, G., Batalha, N., et al. 2011, AJ, 141, 50

Walsh, K. J., Morbidelli, A., Raymond, S. N., O'Brien, D. P., & Mandell, A. M. 2011, Nature, 475, 206

West, A. A., Hawley, S. L., Bochanski, J. J., Covey, K. R., Reid, I. N., Dhital, S., Hilton, E. J., & Masuda, M. 2008, AJ, 135, 785

Winn, J. N., Holman, M. J., Shporer, A., et al. 2008, AJ, 136, 267

Winn, J. N. 2010, Chapter in EXOPLANETS, ed. S. Seager, University of Arizona Press (Tucson, AZ)

Wolfram Research, Inc., Mathematica, Version 7.0, Champaign, IL (2008).

Wright, J. T., Fakhouri, O., Marcy, G. W., et al. 2011, PASP, 123, 412

VITA

Praveen Kundurthy was born in Kochi, India in 1983. He earned his Bachelor of Science degree in Astronomy and Physics, Magna Cum Laude and Honors, from the University of Arizona, Tucson in 2005. He worked as a Research Technician with the Infrared Astronomy Group at Steward Observatory, Tucson between 2005 and 2006. In 2008 he earned his Master of Science degree in Astronomy from the University of Washington, Seattle. In 2012, he earned his Doctor of Philosophy degree in Astronomy from the University of Washington, Seattle.